

國立成功大學  
航空太空工程學系  
碩士論文

National Cheng Kung University  
Department of Aeronautics and Astronautics  
Master Thesis

圓柱後經渦漩引致振動之尾流特性研究  
Wake Flow Characteristics of a Circular Cylinder  
Undergoing Vortex-Induced Vibration

研究生：趙明宏

指導教授：張克勤

共同指導教授：周晉成

Student: Fernando José De La Cruz Chávez

Advisor: Keh-Chin Chang

Co-advisor: Chin-Chen Chou

Tainan, Taiwan, R.O.C.

April 2022

中華民國一一年四月

國立成功大學

碩士論文

圓柱後經渦漩引致振動之尾流特性研究

Wake Flow Characteristics of a Circular Cylinder Undergoing  
Vortex-Induced Vibration

研究生：趙明宏

本論文業經審查及口試合格特此證明

論文考試委員：關志哲

李鼎新

司晉成

張廷勳

指導教授：張廷勳

單位主管：呂幸新

(單位主管是否簽章授權由各院、系(所、學位學程)自訂)

中華民國 111 年 4 月 8 日

## 摘要

題目：圓柱後經渦漩引致振動之尾流特性研究

研究生：趙明宏

指導教授：張克勤、周晉成

結構疲勞破壞因結渦至振動(VIV)產生振盪導致。在過去的幾年裡，VIV 一直在被研究，主要聚焦於“鎖定”現象發生期間的振盪響應。儘管了解振動位移和氣動力作用在結構上以避免這種現象是至關重要，但了解近尾流中的行為也很重要。

本研究使用低速風洞和粒子追蹤測速系統(PIV)，通過實驗研究了在 VIV 引起的氣彈力不穩定性、鎖定和非鎖定狀態下圓柱尾流的渦流結構。由熱線測速系統 (HWA) 量測得速度數據作為確認 PIV 結果可靠度的基準。相位平均技術用於使流場可視化結果更清晰，並應用 Q 準則來檢測尾流中的渦流。另外執行靜態實驗，其結果用於比較動態實驗。研究表明，在共振時，渦旋脫落頻率與結構固有頻率相匹配，此時圓柱的位移最大。隨著圓柱體的振動，自由流和振動圓柱體之間的相對速度發生變化。發現這種變化會影響渦流強度並對尾流中的渦流行為產生很大影響，特別是對渦流中心到中心線的距離以及每個連續渦流之間的距離。因此，渦流型態對圓柱體的振盪很敏感。此外，通過對流場進行統計分析，探討非靜止圓柱的紊流特性。分解相位平均速度，識別真實的速度擾動。

## ABSTRACT

### Wake Flow Characteristics of a Circular Cylinder Undergoing Vortex-Induced Vibration

Fernando José De La Cruz Chávez

Keh-Chin Chang and Chin-Chen Chou

*Department of Aeronautics and Astronautics, National Cheng Kung University*

#### SUMMARY

The instability of structures under the presence of vortex-induced vibration (VIV) can generate oscillations which may cause fatigue damage to the structure. In past years, VIV has been studied and its main focus has concerned the oscillation response during the “lock-in” phenomenon. Even though it is crucial to know the vibrating displacement and forces acting on the structure to avoid this phenomenon, understanding the behavior in the near-wake flow can be important too.

This study experimentally investigates the vortical structures in the wake of a circular cylinder during aeroelastic instability induced by VIV, at lock-in and at non-lock-in state, using a low-speed wind tunnel and a particle image velocimetry (PIV) system. The velocity data from a hot-wire anemometry (HWA) system is used as a benchmark to confirm the reliability of the PIV results. The phase average technique is used to have a clearer visualization of the flow field and the Q-criterion is applied to detect the vortices in the wake. Static experiments were also done, and the results are used for comparison. This study reveals that at resonance, the vortex shedding frequency matches that of the structural natural frequency, and the displacement of the vibrating cylinder is the largest. As the cylinder oscillates, the relative velocity between the freestream and the vibrating cylinder is altered. This alteration is found to affect the vortex strength and to have a great influence on the behaviors of the vortices in the wake, specifically on the distances of the vortex center from the centerline and the distance between each consecutive vortex. Therefore, the vortex patterns are sensitive to the oscillation of the cylinder. In addition, the turbulent characteristics of the non-stationary cylinder are explored by performing a statistical analysis of the flow. The phase-averaged velocity is decomposed, and the true velocity fluctuations are identified.

**Keywords:** VIV, PIV, Q Criterion, Phase Average, Vortex, Coherent Structure, Turbulent Characteristics

## ACKNOWLEDGMENT

A new chapter in my life is about to end, the one as a master student at National Cheng Kung University. It was difficult in many ways. I took challenging courses filled with complicated equations; spent countless hours doing sophisticated experiments and analyzing data; had sleepless nights reading papers and writing this Thesis. I felt very overwhelmed at some moments, but here I am finishing my master's degree, something that could not be possible without the people that helped me throughout this journey.

First, I want to thank my parents for their unconditional support. Even though I decided to study a bachelor's degree in Taiwan, far away from home, and then chose to stay here to continue with my graduate studies, they encouraged me to follow my aspirations. I love you both; thank you for being the voice of reason. I also want to thank Professor Chang for his guidance. His enthusiasm about turbulence and about research in general inspired me to keep studying and learning new things. I am also very thankful to Dr. Chou who carefully and patiently guided me during the past two years. He taught me new skills and assisted me with any problem that I encountered. Thank you for always pushing me to my limits and out of my comfort zone. I also want to say a special thank you to Sally for helping me with all the difficulties that came across; whose optimism and enthusiasm were a driving force that kept me moving forward. Finally, I want to give thanks to Mr. Lin, Mr. Lee, and Mr. Wang for taking the time to assist me with the preparations of my experiments; to Do-Van Dong for his advice and companionship in the lab; to Tai Wei for sharing his knowledge and skills with me; Tzu Hsun and Teresa for explanations about analysis and experiments.

# CONTENT

摘要.....	II
ABSTRACT.....	III
ACKNOWLEDGMENT.....	IV
CONTENT.....	V
LIST OF TABLES.....	VIII
LIST OF FIGURES.....	X
NOMENCLATURE.....	XV
Chapter 1 – Introduction.....	1
1.1 Motivation and objective.....	2
Chapter – 2 Literature review.....	4
2.1 Flow induced vibration.....	4
2.2 Vorticity and vortex structures.....	4
2.2.1 Q criterion.....	5
2.3 Vortex shedding.....	6
2.4 Vortex-induced vibration.....	7
2.4.1 Harmonic model and non-dimensional parameters.....	7
2.4.2 Lock-in state.....	10
2.4.2.1 Frequency synchronization.....	10
2.4.2.2 Influence of mass damping ratio on amplitude response.....	11
2.4.3 Vortex patterns.....	12
2.4.4 Effects of Reynolds number.....	12
2.4.4.1 Amplitude response.....	13
2.4.4.2 Vortex formation.....	13
2.5 Stationary versus vibrating cylinders.....	14
2.6 Turbulence spectra and length scales.....	15
2.6.1 Energy cascade.....	15
2.6.2 Turbulence spectra.....	16
2.6.3 The -5/3 Kolmogorov law of turbulence.....	17
2.6.4 Turbulence length scales.....	17
Chapter 3 – Experimental facility and methodology.....	24

3.1	Wind tunnel .....	24
3.2	Cylinder models .....	25
3.3	Methodology .....	27
3.4	Velocity measurement instrumentation.....	28
3.4.1	Particle Image Velocimetry (PIV).....	28
3.4.1.1	Seeding system .....	29
3.4.1.2	Analysis software .....	30
3.4.2	Hotwire anemometry .....	31
3.4.2.1	HWA calibration.....	32
3.4.2.2	Turbulence spectra analysis.....	34
3.4.3	Pitot tube.....	35
3.5	Experimental setup.....	35
3.5.1	Static setup.....	36
3.5.2	Aeroelastic setup.....	36
3.6	Uncertainty and error analysis.....	38
3.6.1	HWA errors .....	38
3.6.2	PIV errors .....	39
Chapter 4 – Experimental results and discussion.....		54
4.1	Fixed test .....	54
4.1.1.1	Selection of seeding material.....	54
4.1.2	Verification of analysis techniques.....	55
4.1.3	PIV results .....	57
4.1.3.1	Standard deviation .....	57
4.1.3.2	Characteristics of the mean and fluctuating velocity fields.....	58
4.2	Vibrating test.....	59
4.2.1	Frequency response .....	60
4.2.2	Amplitude response .....	61
4.3	Strouhal number data .....	62
4.4	Inertial subrange and Taylor subrange length scales .....	63
4.5	Vortex visualization in the wake .....	66
4.5.1	Vorticity and vortex strength.....	68
4.5.2	Vortex center location .....	69
4.6	Phase-averaged velocity decomposition .....	71

Chapter 5 – Conclusions ..... 111

    5.1 Concluding remarks ..... 111

    5.2 Future prospect..... 112

REFERENCES ..... 113



## LIST OF TABLES

Table 3-1 Error sources and uncertainty of HWA system. Note: the free stream velocity considered is 5 m/s. ....	41
Table 3-2 Error sources and uncertainty of PIV system. Note: these values correspond to an interrogation window size of $32 \times 32$ . ....	41
Table 4-1 Maximum error percentage of mean streamwise velocity profile between HWA and PIV using oil and solid particles at different stations for $Re = 1.3 \times 10^4$ and $Re = 2.4 \times 10^4$ . ....	74
Table 4-2 Summary of the normalized standard deviations ( $\sigma$ ) and standard errors (SE) of the mean streamwise velocity at different positions. ....	74
Table 4-3 Frequency results obtained from HWA experiments for four different $U^*$ cases at both stations $x/D = 4$ and $6$ . ....	74
Table 4-4 Vortex shedding frequency and Strouhal number results obtained from HWA tests for each case tested. ....	75
Table 4-5 Upper and lower limits ( $k_1, k_2$ ) of the inertial subrange shown in the energy density spectrum (Figure 4.23) of each case tested. ....	75
Table 4-6 Integral and Taylor length scales of each case tested, measured at two different stations, $x/D = 4$ and $6$ , for both static and vibrating cylinders. Note: values are expressed in micrometers ( $\mu\text{m}$ ). ....	75
Table 4-7 Number of samples in one period ( $N_p$ ), total number of periods in data ( $TN_p$ ), and the first zero-up-cross sample of each case tested. ....	76
Table 4-8 Distances from the center of vortex 1, vortex 2 and vortex 3, to the x-axis (normalized with $D$ ), defined as $y-V_1$ , $y-V_2$ , and $y-V_3$ , respectively. Results of static and vibrating cases at $U^*=3.3$ for different phases ( $tp/T$ ). ....	76
Table 4-9 Distances from the center of vortex 1, vortex 2 and vortex 3, to the x-axis (normalized with $D$ ), defined as $y-V_1$ , $y-V_2$ , and $y-V_3$ , respectively. Results of static and vibrating cases at $U^*=4.6$ for different phases ( $tp/T$ ). ....	76
Table 4-10 Distances from the center of vortex 1, vortex 2 and vortex 3, to the x-axis (normalized with $D$ ), defined as $y-V_1$ , $y-V_2$ , and $y-V_3$ , respectively. Results of static and vibrating cases at $U^*=5.3$ for different phases ( $tp/T$ ). ....	77
Table 4-11 Distances from the center of vortex 1, vortex 2 and vortex 3, to the x-axis (normalized with $D$ ), defined as $y-V_1$ , $y-V_2$ , and $y-V_3$ , respectively. Results of static and vibrating cases at $U^*=6$ for different phases ( $tp/T$ ). ....	77

Table 4-12 Distances between vortex 1 (V1) and vortex 3 (V3), defined as C13 (normalized with D), of static and vibrating case at  $U^* = 3.3$  for different phases ( $tp/T$ ). .....77

Table 4-13 Distances between vortex 1 (V1) and vortex 3 (V3), defined as C13 (normalized with D), of static and vibrating case at  $U^* = 4.6$  for different phases ( $tp/T$ ). .....78

Table 4-14 Distances between vortex 1 (V1) and vortex 3 (V3), defined as C13 (normalized with D), of static and vibrating case at  $U^* = 5.3$  for different phases ( $tp/T$ ). .....78

Table 4-15 Distances between vortex 1 (V1) and vortex 3 (V3), defined as C13 (normalized with D), of static and vibrating case at  $U^* = 6$  for different phases ( $tp/T$ ). .....78



## LIST OF FIGURES

Figure 2.1. Strouhal number vs Reynolds number for circular cylinders (Blevins, 1990). ....	19
Figure 2.2. Vibration of a two-dimensional, spring-supported, damped model in steady flow. .....	19
Figure 2.3. Time history and cylinder vibration spectrum at a) pre-lock-in, b) lock-in, and c) after lock-in states (Goswami et al., 1993). ....	20
Figure 2.4. Amplitude vs reduced velocity for different structural damping (Goswami et al., 1993). ....	20
Figure 2.5. a) Two-branch response plot for high mass damping values. b) Three-branch response plot for low mass damping values (Govardhan & Williamson, 2006). ....	21
Figure 2.6. Map of regimes for the different vortex modes (Williamson & Roshko, 1988). ..	21
Figure 2.7. a) Amplitude vs mass damping ratio curves for constant Re, and b) Displacement traces at zero mass damping for different Re. Mass is kept constant $m^* = 10$ . From (Govardhan & Williamson, 2006). ....	22
Figure 2.8. A typical energy spectrum of turbulent flow depicting the energy cascade process. It is divided into three different ranges, each corresponding to a different length scale of eddies. ....	23
Figure 2.9. A turbulence spectrum and its characteristics. The behavior of the spectra in the inertial range follows the $-5/3$ Kolmogorov law of turbulence. ....	23
Figure 3.1. Diagram of the low-speed wind tunnel used in this research. ....	42
Figure 3.2. Design of circular cylinder model for vibrating tests. ....	42
Figure 3.3. Cylinder (Model 2) used for vibrating tests installed in the low-speed wind tunnel. Three laser sensors were used to measure the amplitude of vibration. ....	43
Figure 3.4. Green laser DPSS 532 nm – 5W. ....	43
Figure 3.5. High speed camera Photron Fastcam SA-X. ....	44
Figure 3.6. Custom made mirror for PIV laser. ....	44
Figure 3.7. Camera lens Nikon NIKKOR 50 mm f/1.2. ....	45
Figure 3.8. Seeding injector. ....	45
Figure 3.9. Design of the particle seeding device. ....	46
Figure 3.10. DANTEC Streamline Pro CTA 90C10 system. ....	46
Figure 3.11. NI BNC-210 terminal block. ....	47
Figure 3.12. X-wire probe 55P61 and its orientation with respect to experimental coordinate system. ....	47

Figure 3.13. Low pressure calibrator DPI610.....	48
Figure 3.14. Percentage of raw data that satisfy the condition $\beta \leq 45^\circ$ at streamwise stations of $x/D = 4$ and 6 for the case of $Re = 1.3 \times 10^4$ .....	48
Figure 3.15. Validyne DP103-18 low pressure variable reluctance sensor. ....	49
Figure 3.16. Experimental layout of the PIV static test.....	49
Figure 3.17. Experimental layout of the PIV vibrating test.....	50
Figure 3.18. The HWA static test setup. It shows the circular cylinder model and the structure supporting the HWA probe. The vertical bar has a moving mechanism that can move the plate supporting the HWA in the y direction. ....	50
Figure 3.19. Experimental layout of HWA test (for aeroelastic test). ....	51
Figure 3.20. The laser sensors KEYENCE IL-1000.....	51
Figure 3.21. The NI cDAQ-9178.....	52
Figure 3.22. Aluminum box holder mounted at the ends of both models. ....	52
Figure 3.23. Structure that supports the model for the static experiments. ....	53
Figure 3.24. Design of aeroelastic support structure .....	53
Figure 4.1. Comparison of mean streamwise velocity profiles obtained with PIV solid, PIV oil, and HWA at $Re = 1.3 \times 10^4$ and at the stations of $x/D = 2, 4, 6$ .....	79
Figure 4.2. Comparison of mean streamwise velocity profiles obtained with PIV solid, PIV oil, and HWA at $Re = 2.4 \times 10^4$ and at the stations of $x/D = 2, 4, 6$ .....	79
Figure 4.3. Comparison of mean streamwise velocity profiles between present PIV solid, and HWA results and Lin (2021) HWA results at $Re = 1.3 \times 10^4$ and at the stations of $x/D = 2, 4$ and 6.....	80
Figure 4.4. Comparison of mean lateral velocity profiles between present PIV solid, and HWA results and Lin (2021) HWA results at $Re = 1.3 \times 10^4$ and at the stations of $x/D = 2, 4$ and 6.....	80
Figure 4.5. Comparison of root-mean-square streamwise velocity profiles obtained with PIV and HWA at $Re = 1.3 \times 10^4$ and at the stations of $x/D = 2, 4$ and 6. ....	81
Figure 4.6. Comparison of root-mean-square lateral velocity profiles obtained with PIV and HWA at $Re = 1.3 \times 10^4$ and at the stations of $x/D = 2, 4$ and 6. ....	81
Figure 4.7. Comparison of mean lateral velocity profiles obtained with PIV and HWA at $Re = 2.4 \times 10^4$ and at the stations of $x/D = 2, 4$ and 6. ....	82
Figure 4.8. Comparison of root-mean-square streamwise velocity profiles obtained with PIV and HWA at $Re = 2.4 \times 10^4$ and at the stations of $x/D = 2, 4$ and 6. ....	82

Figure 4.9. Comparison of root-mean-square lateral velocity profiles obtained with PIV and HWA at $Re = 2.4 \times 10^4$ and at the stations of $x/D = 2, 4$ and $6$ .	83
Figure 4.10. Variations of standard deviations and standard errors of mean streamwise velocity taken at the point $(x/D=4, y/D=1)$ for a) $Re = 1.3 \times 10^4$ and b) $Re = 2.4 \times 10^4$ . *Values are normalized with free stream velocity.	83
Figure 4.11. Variations of standard deviations of mean streamwise velocity taken at the points $(x/D=4, y/D=1)$ and $(4, 3)$ for a) $Re = 1.3 \times 10^4$ and b) $Re = 2.4 \times 10^4$ .	84
Figure 4.12. Mean streamwise velocity contour and velocity profiles for stations $x/D=4$ and $6$ , at a) $Re = 1.3 \times 10^4$ and b) $Re = 2.4 \times 10^4$ . *Static case using Model 1.	85
Figure 4.13. Normalized streamwise and lateral mean and root-mean-square velocity profiles at different stations $(x/D = 3, 4, 5, 6$ and $7)$ for a) $Re = 1.3 \times 10^4$ and b) $Re = 2.4 \times 10^4$ . *Static case using Model 1.	86
Figure 4.14. a) Decay curve of displacement after an initial excitation, and b) the structural natural frequency $f_n$ determined by FFT.	87
Figure 4.15. Close up of the free decay amplitude curve with three peaks identified as peak 0, peak 1, and peak n, highlighted with a red point.	87
Figure 4.16. Time histories and spectra of cylinder vibrations and velocity fluctuations for the case of $U^* = 5.3$ . a) Time histories of velocity fluctuation (red) and vibration amplitude (green), b) velocity fluctuation spectrum, and c) amplitude fluctuation spectrum.	88
Figure 4.17. Time histories and spectra of cylinder vibrations and velocity fluctuations for the case of $U^* = 3.3$ . a) Time histories of velocity fluctuation (red) and vibration amplitude (green), b) velocity fluctuation spectrum, and c) amplitude fluctuation spectrum.	88
Figure 4.18. Time histories and spectra of cylinder vibrations and velocity fluctuations for the case of $U^* = 4.6$ . a) Time histories of velocity fluctuation (red) and vibration amplitude (green), b) velocity fluctuation spectrum, and c) amplitude fluctuation spectrum.	89
Figure 4.19. Time histories and spectra of cylinder vibrations and velocity fluctuations for the case of $U^* = 6$ . a) Time histories of velocity fluctuation (red) and vibration amplitude (green), b) velocity fluctuation spectrum, and c) amplitude fluctuation spectrum.	89
Figure 4.20. Free vibration response of the elastically mounted cylinder. The maximum displacement is plotted against the velocity ratio. a) data presented by Williamson and Govardhan (2004). b) the data acquired in the present study.	90
Figure 4.21. Strouhal number as a function of the Reynolds number. The blue line represent the Strouhal number envelope proposed by Lienhard (1966). Present results of static test	

are shown with green circles, while brown squares represent data from vibrating tests. Gray diamonds represent data of vibrating experiments from literature. Yellow triangles show data of static experiments from literature. ....90

Figure 4.22. Plot of sum of absolute differences for different window sizes of static case,  $U^*=3.3$ ; collected at point  $(x/D, y/D) = (4, 1)$ . The size utilized is that at which the SAD is greater than 90% of the asymptotic value. In this case the moving average size is 39, highlighted in red. ....91

Figure 4.23. Turbulence energy spectra density of each case tested. The actual energy density is represented in blue. The smoothed signal (by moving average) is depicted in yellow. The red line, which has a slope of  $-5/3$ , indicates the approximate inertial range. Figures a), c), e) and g) are results of the static case. Figures b), d), f), and h) are results of the vibrating case. Results of velocity ratios  $U^* = 3.3, 4.6, 5.3, \text{ and } 6$ , are shown in Figures a) and b), c) and d), e) and f), g) and h), respectively. \*All results were obtained at point  $(x/D, y/D) = (4, 1)$ . ....92

Figure 4.24. Length scale factors of  $\Delta x$  and  $\lambda x$  at stations  $x/D = 4$  and  $6$ . (Refer to Equation (4.9)). ....92

Figure 4.25. The phase average wave data (minus its average) and its zero-up-crossing index of vibrating case  $U^*=5.3$ . Each circle can represent the zero phase ( $t_p / T = 0$ ). .....93

Figure 4.26. Root-mean-square variance and standard deviation of phase-averaged data for vibrating tests measured at point  $(x/D, y/D) = (4,2)$ . a) are results of  $U^* = 3.3$ , and b) are results of  $U^* = 6$ . ....94

Figure 4.27. Root-mean-square variance and standard deviation of phase-averaged data for static tests measured at point  $(x/D, y/D) = (4,2)$ . a) are results of  $U^* = 3.3$ , and b) are results of  $U^* = 6$ . ....95

Figure 4.28. Phase-averaged normalized vorticity contour and vortex contour lines by Q criterion for static tests at different phases  $t_p/T$ . Yellow star denotes the vortex center (the maximum Q value). ....97

Figure 4.29. Phase-averaged normalized vorticity contour and vortex contour lines by Q criterion for vibrating tests at different phases  $t_p/T$ . Yellow (or red) star denotes the vortex center (the maximum Q value). ....99

Figure 4.30. Distance from vortex center (depicted with a yellow star) to x-axis ( $y/D=0$ ). Labeled for each vortex, from left to right, as  $y-V1, y-V2, y-V3$ . .... 100

Figure 4.31. Distance between center of vortex 1 (V1) and vortex 3 (V3), defined as  $C_{13}$ . ... 100

Figure 4.32. Phase-averaged vortex strength contour by Q criterion for static tests at different phases $tp/T$ .	102
Figure 4.33. Phase-averaged vortex strength contour by Q criterion for vibrating tests at different phases $tp/T$ .	104
Figure 4.34. Comparison of vortex center locations (y-V1, y-V2 and y-V3) at phase $tp/T = 0$ between static and vibrating case for $U^* = 3.3, 4.6, 5.3$ and $6$ .	105
Figure 4.35. Comparison of the path of a specific vortex center (starting with y-V1 at phase $tp/T = 0$ ) through all phases, between $U^* = 3.3, 4.6, 5.3$ and $6$ for vibrating case. *Note that the same vortex center becomes y-V3 at phase $tp/T = 8$ .	105
Figure 4.36. Comparison of the vortex center distances between V1 and V3 (C13) at $tp/T = 0$ between static and vibrating cases for $U^* = 3.3, 4.6, 5.3$ and $6$ .	106
Figure 4.37. Phase-averaged velocity contour of case $U^* = 6$ at $tp/T = 0$ . Red dots depict the two positions selected, $(x/D, y/D) = 4, 0.5$ and $(4, 1)$ , to perform the decomposition of the phase-averaged velocities.	106
Figure 4.38. a) Phase-averaged velocity fluctuation during five periods ( $tp/T = 5$ ). b) Phase-averaged velocity fluctuation within one arbitrary period ( $tp/T = 1$ ). c) Root-mean-square of the “real fluctuating” velocity ( $tp/T = 1$ ). *Each term is computed at $(x/D, y/D) = (4, 0.5)$ for the case of $U^* = 6$ and normalized with $U_f$ .	107
Figure 4.39. a) Phase-averaged velocity fluctuation during five periods ( $tp/T = 5$ ). b) Phase-averaged velocity fluctuation within one arbitrary period ( $tp/T = 1$ ). c) Root-mean-square of the “real fluctuating” velocity ( $tp/T = 1$ ). *Each term is computed at $(x/D, y/D) = (4, 1)$ for the case of $U^* = 6$ and normalized with $U_f$ .	107
Figure 4.40. a) Phase-averaged velocity fluctuation during five periods ( $tp/T = 5$ ). b) Phase-averaged velocity fluctuation within one arbitrary period ( $tp/T = 1$ ). c) Root-mean-square of the “real fluctuating” velocity ( $tp/T = 1$ ). *Each term is computed at $(x/D, y/D) = (4, 0.5)$ for the case of $U^* = 6$ and normalized with $u_{pa}$ .	108
Figure 4.41. a) Phase-averaged velocity fluctuation during five periods ( $tp/T = 5$ ). b) Phase-averaged velocity fluctuation within one arbitrary period ( $tp/T = 1$ ). c) Root-mean-square of the “real fluctuating” velocity ( $tp/T = 1$ ). *Each term is computed at $(x/D, y/D) = (4, 1)$ for the case of $U^* = 6$ and normalized with $u_{pa}$ .	108
Figure 4.42. Time histories of the phase-averaged velocity, and root-mean-square of the phase-averaged fluctuating velocity measured at points $(x/D, y/D) = (4, 0), 4, 0.5$ and $(4, 1)$ for a) $U^* = 3.3$ , b) $U^* = 4.6$ , c) $U^* = 5.3$ , d) $U^* = 6$ .	110

## NOMENCLATURE

$A$	Amplitude
$A_y$	Amplitude of vibration in the y-direction
$A_{max}^*$	Maximum amplitude ratio
$b$	Width
$c$	Structural damping
$C_{EA}$	Effective added mass coefficient, Eq. (2.14)
$C_L$	Lift coefficient, Eq. (2.9)
$C_{13}$	Distance between center of vortex V1 and V3 (Figure 4.31)
$D$	Outer diameter of the circular cylinder model
$D_o, D_i$	Outer and inner diameter
$E$	Modulus of elasticity; voltages of hot-wires
$F$	Force
$F_L$	Lift force
$f_n$	Natural frequency, Eq. (3.3)
$f_s$	Vortex shedding frequency, Eq. (3.1)
$h$	Height
$I$	Moment of inertia, Eq. (3.22)
$k$	Spring stiffness, Eq. (3.20)
$L$	Length of the model; lift
$l_0$	Characteristic length of model (Diameter)
$m$	Mass per unit length
$m_A$	Added mass
$M$	Mass of the model
$N$	Number of samples
$N_p$	Number of samples in one period
$n$	Period number
$p$	Pressure
$Q$	Second invariant of velocity gradient tensor, Eq. (2.6)
$Re$	Reynolds number, Eq. (2.16)
$S$	Strain rate tensor, Eq. (2.3)
$Sc$	Scruton number, Eq. (2.17)

$St$	Strouhal number, Eq. (2.7)
$Stk$	Stokes number, Eq. (3.4)
$t$	Time
$T_n$	Period of natural oscillation, Eq. (4.6)
$T_s$	Vortex shedding period
$T_{N_p}$	Total number of periods within number of samples acquired
$t_p$	Phase time varying from 0 to T
$u$	Streamwise velocity
$\bar{u}, u'$	Mean and fluctuating streamwise velocity
$\tilde{u}_{pa}$	Quasiperiodic component of velocity
$U$	Streamwise mean flow velocity
$U_f$	Streamwise free stream velocity
$u_{pa}$	Phase-averaged streamwise velocity
$\overline{u_{pa}}$	Mean phase-averaged streamwise velocity
$v$	Velocity in the y direction
$\bar{v}, v'$	Mean and fluctuating lateral velocity
$V1, V2, V3$	Vortex 1, vortex 2 and vortex 3 (Figure 4.30 and Figure 4.31)
$W$	Weight
$x$	Position / displacement in the x-direction
$y$	Position/displacement from equilibrium position in y-direction
$\dot{y}; \ddot{y}$	Time derivatives of displacement
$y-V1, y-V2, y-V3$	Distance from x-axis to vortex center (Figure 4.30)

### Abbreviations

DoF	Degree of freedom
FIV	Flow-induced vibration
fps	Frames per second
HWA	Hot wire anemometer
KE	Kinetic energy, Eqns. (2.22), (2.23)
LS	Length scale
MF	Magnification factor
PIV	Particle-image velocimetry

rms	Root mean square
SAD	Sum of absolute differences, Eq. (4.8)
SE	Standard error, Eq. (4.3)
std	Standard deviation
VIV	Vortex-induced vibration

### Greek symbols

$\alpha$	Mass damping ratio
$\delta$	Deflection of springs, Eqns. (3.21), (3.23)
$\lambda_x$	Taylor scale of eddies
$\Lambda_x$	Integral scale of eddies, Eq. (2.24)
$\rho$	Density of fluid ( $kg/m^3$ )
$\zeta$	Damping of the system, Eq. (4.4)
$\tau$	Viscous stress tensor, Eq. (2.5)
$\Omega$	Rotation rate tensor, Eq. (2.4)
$\beta$	Angle of flow from the x-axis, Eq. (3.14)
$\eta$	Kolmogorov microscale, Eq. (2.26)
$\sigma$	Standard deviation, Eq. (4.2)
$\sigma_{\bar{x}}$	Standard error, Eq. (4.3)
$\mu$	Dynamic viscosity of the fluid ( $kg/(m \cdot s)$ )
$\omega$	Vorticity; angular vortex shedding frequency, Eq. (3.2)
$\phi$	Phase angle

### Non-dimensional parameters

$A^*$	$\frac{A}{D}$	Amplitude ratio (See also Eqns. (2.12) and 2.15)
$U^*$	$\frac{U}{f_n D}$	Velocity ratio
$m^*$	$\frac{m}{\pi \rho D^2 L / 4}$	Mass ratio
$\zeta$	$\frac{\delta}{\sqrt{4\pi^2 + \delta^2}}$	Damping ratio
$\alpha$	$m^* \zeta$	Mass damping ratio
$f^*$	$\frac{f_s}{f_n}$	Frequency ratio (See also Eqn. (2.13))
$Re$	$\frac{\rho U D}{\mu}$	Reynolds number
$\omega^*$	$\frac{\omega D}{U}$	Normalized vorticity

## Chapter 1 – Introduction

In recent years, due to the rapid increase in population, many new structures are being constructed, such as bridges, tall buildings, and electricity cable systems. Oftentimes, structures with bluff bodies cross section, such as circular and rectangular, are employed. The main purpose of this type of structures is to bear loads under the conditions of containing flow or providing heat transfer, unlike aircraft components which intend to reduce drag and increase lift (Blevins, 1990). Due to their cross-section shape, they tend to block the flow of fluids, which in turn forms a large wake region with vortices behind the structure.

Fluids, such as air and water, are present everywhere in this world. They are applied extensively in aerospace engineering, underwater engineering, civil engineering, thermal power engineering, etc. When a fluid flows around a structure, it exerts a force on them. The flow of such fluids can cause useful motions such as the rotation of a wind turbine and the lift of an aircraft; however, it can also cause destructive vibrations, which usually happens when vortices are synchronized. This phenomenon is common in bluff structures, making them susceptible to fluid force fluctuation, which may result in some type of flow induced vibration (FIV), such as vortex induced vibration (VIV), galloping or flutter, and may even cause the destruction of the structure. Under a steady flow, bluff structures are susceptible to flow-induced vibrations due to the shedding of vortices caused by the interaction between both separated shear layers. This phenomenon is known as vortex-induced vibration (VIV).

It is well agreed that the cost for performing numerical simulations is lower than that for conducting experiments in a wind-tunnel. With numerical simulations one can reproduce complicated flow fields, but it is necessary to verify the data and assess the accuracy of the results beforehand. This is where experimental studies come into play. Experimental studies can provide more realistic and reliable results. It is thus important to combine experiments with numerical simulations, or to verify the results with other references, in order to trust the results

obtained in research. For wind tunnel experiments, there exist different measurement techniques that can be used to obtain information about the physical mechanism of the structures and the dynamics of the flow. Particle Image Velocimetry (PIV) is one of the popular measurement techniques in the present used for research in fluid mechanics. It is a non-intrusive technique that captures velocity information of whole flow fields and provides spatial and temporal information of the velocity flow field. From this information, quantitative visualizations of the instantaneous flow patterns can be made, and spatial differential quantities of turbulence can be obtained, such as velocity field, vorticity, and turbulent kinetic energy. In PIV, the fluid motion is made visible by adding tracer particles and illuminating them with a laser. From the positions of these tracer particles at two instances in time, the displacement can be obtained, and the velocity can be inferred. This is the main method used in the present study to visualize the fluid flow and its wake characteristics.

Another common method used for velocity field measurements is the Hot-Wire Anemometry (HWA). Unlike PIV technique, HWA is a “point-wise” technique, meaning that the information of the flow field is obtained at a fixed point with a series of time, and it is based on convective heat transfer from a heated wire in a fluid flow. It is composed of sensors, thin metallic wires, that are heated by an electric current and cooled by the incident flow. The sensor heating current varies with the fluid velocity to maintain constant sensor resistance, and, thus, constant sensor temperature. From the temperature or resistance attained by the sensor, information about the flow can be deduced, such as mean and fluctuating velocity components (Comte-Bellot, 1976).

## **1.1 Motivation and objective**

Bluff structures with circular and square cross sections are the most used in the design of multiple slender structures subjected to cross flow, and they are prone to different aeroelastic instabilities. If the oscillating structure is light and low damped, the dissipation capability of

the system is low, and VIV may occur with large amplitudes in a wide range of flow speeds. These types of flows are complex due to the formation of boundary layer, shear layers, and recirculatory flow regions. By understanding the flow behaviors around bluff structures undergoing vortex-induced vibrations, the responses of such structures can be predicted, and the destructive oscillations could be avoided.

Experimental and theoretical studies on the wake characteristics and VIV of structures with circular and square cross sections are abundant. However, most studies focus on the physical response of the fluid-structure interaction, such as vibration amplitudes and forces applied by the fluid on the cylinder, employing forced vibration tests, in which the frequency and amplitude of vibration is controlled independently.

For these reasons, this research aims to investigate the wake characteristics behind an elastically suspended circular cylinder undergoing vortex-induced vibration during free vibration at Reynolds numbers in the subcritical range, in a low-speed wind tunnel. Visualization of the flow field phenomena during lock-in state is done using a PIV system and the identification of vortices is accomplished by means of the Q-criterion analysis (Jeong & Hussain, 1995), with the intention of understanding the well-known physical consequences of this vibration. A hot-wire anemometer is used to obtain the velocity flow field data, which is used as a benchmark to examine the accuracy of the PIV results.

## Chapter 2 – Literature review

### 2.1 Flow induced vibration

The force exerted on a structure by the fluid creates a feedback loop. The fluid force causes the structure to deform; as the structure deforms, its orientation to the flow changes, while exerting an equal but opposite force on the fluid. The structure force on the fluid can synchronize vortices in the wake and produce large amplitude vibrations. This is called flow-induced vibration (FIV), which arises from distinct fluid dynamic phenomena and can be classified depending on the type of flow, either steady or unsteady, and the type of structure (Blevins, 1990). Vortex-induced vibration (VIV) is one of the most common flow-induced vibration phenomena. It is a self-excited oscillation with limited amplitude which is caused by periodical forces on the structure of the oscillatory system. Due to its importance, it has been widely investigated using different approaches targeting different phenomena. A literature review about the VIV of circular cylinders is presented along this section, as well as the different methods used to measure the flow field.

### 2.2 Vorticity and vortex structures

As it is known, vorticity is a relative term to indicate the direction of fluid rotation. It is a vector which, in 2D, only has a component in the direction perpendicular to the plane. A positive value of this component indicates counterclockwise rotation, while a negative value means a clockwise rotation. It is mathematically defined as the curl of the velocity field and is hence a measure of local rotation of the fluid, as follows:

$$\omega(r, t) = \nabla \times V(r, t) \quad (2.1)$$

Qualitatively, regions of spinning fluid are associated with vorticity, which are known as vortices. There exist many definitions of a vortex, however, in this study we define a vortex as a region containing both a positive second invariant of  $\nabla u$  and low pressure, as proposed by

Hunt et al. (1988). Visualization of the coherent vortical structures in the flow can provide valuable information of the flow field. However, detection and identification of these structures by using the vorticity magnitude does not sufficiently describe accurate coherent structures, in addition to other drawbacks. Thus, to have a better visualization of the wake flow, the detection of vortex structures is preferred over the vorticity. That is, by detecting the vortices in the wake, the coherent vortical structures can be seen clearer. Even though there are different metrics that can be used to identify vortical structures numerically, there is no single perfect method to do so. Nevertheless, focus is made on the  $Q$  criterion in this study, which is an Eulerian scalar used for vortex identification (Hunt et al., 1988).

### 2.2.1 $Q$ criterion

The  $Q$  criterion is an objective method used to detect and visualize vortices. For two dimensional flows, it can be turned into a mathematically exact vortex definition. In some cases, it can be proven that fluid particles form impenetrable swirling regions (Haller, 2001; Koh & Legras, 2002). In addition, regions of stretching in two-dimensional flows can be detected by using this method (Lapeyre et al., 2001).

In tensor notation, the value  $Q$  comes from the definition of the velocity gradient tensor  $\nabla u = \delta u_i / \delta x_j$ . This tensor can be separated into a symmetric part  $S$ , known as the strain rate tensor, and an antisymmetric part  $\Omega$ , known as the rotation rate or vorticity tensor, such that  $\nabla u = S + \Omega$ , as follows.

$$\frac{\delta u_i}{\delta x_j} = \frac{1}{2} \left[ \left( \frac{\delta u_i}{\delta x_j} \right) + \left( \frac{\delta u_j}{\delta x_i} \right) \right] + \frac{1}{2} \left[ \left( \frac{\delta u_i}{\delta x_j} \right) - \left( \frac{\delta u_j}{\delta x_i} \right) \right] \quad (2.2)$$

where the strain rate tensor is

$$S = \frac{1}{2} \left[ \left( \frac{\delta u_i}{\delta x_j} \right) + \left( \frac{\delta u_j}{\delta x_i} \right) \right] \quad (2.3)$$

and the rotation rate (or vorticity) tensor is

$$\Omega = \frac{1}{2} \left[ \left( \frac{\delta u_i}{\delta x_j} \right) - \left( \frac{\delta u_j}{\delta x_i} \right) \right]. \quad (2.4)$$

Because the viscous stress tensors  $\tau$  are specifically functions of the strain rate only,

$$\tau = \mu \left[ \left( \frac{\delta u_i}{\delta x_j} \right) + \left( \frac{\delta u_j}{\delta x_i} \right) \right] \quad (2.5)$$

$Q$  can then be calculated as the second invariant of the velocity gradient tensor as follows

$$Q = \frac{1}{2} (|\Omega|^2 - |S|^2). \quad (2.6)$$

Thus,  $Q$  represents the local balance between shear strain rate and vorticity magnitude (Jeong & Hussain, 1995).

Furthermore, the  $Q$ -criterion of Hunt et al. (1988) defines a vortex as a spatial region of  $Q > 0$ , for instance, where the vorticity tensor dominates the strain rate tensor. Hence, positive values of  $Q$  indicate areas in the flow field where the local rate of rotation ( $\Omega$ ) is dominant, while negative values indicate the areas dominated by the rate of strain or viscous stress ( $S$ ).

### 2.3 Vortex shedding

As stated in literature (Hsieh et al., 2017; Zdravkovich, 1997), vortex shedding represents the main characteristic of the wake of a stationary cylinder. A vortex is a mass of fluid rotating around a common center in which a force of suction operates as a whirlpool. The speed of the fluid that circulates around the vortex increases as it approaches the center, while the pressure decreases. It is defined by the vorticity in the fluid, which indicates the rate and direction of fluid rotation. When a uniform two-dimensional flow pass over a bluff structure, it separates and forms two shear layers (thin regions of concentrated vorticity), across which a large velocity gradient exists. The vorticity within the shear layers is fed by the energy in the oncoming flow and grows until it is shed in the form of a vortex. If this process is repeated periodically, a Von Karman Vortex street is formed (Goswami et al., 1993). Vortex streets are formed in the wake of bluff bodies over a broad range of Reynolds numbers, from about 50 to

$10^6$  and higher (Griffin, 1995). The frequency at which the vortices are shed depends on the stream velocity as well as the dimension of the cylinder  $D$ . This dependence is reflected by the Strouhal number ( $St$ ):

$$St = \frac{f_s D}{U_f} \quad (2.7)$$

which is a dimensionless constant that describes the oscillating flow mechanism; where  $f_s$  is the vortex shedding frequency,  $D$  is the diameter of the cylinder, and  $U_f$  is the free stream velocity. It is well known that for a circular cylinder,  $St \cong 0.2$  over a large Reynolds number interval, as found by Blevins (1990), shown in Figure 2.1. The phenomenon of vortex shedding and its corresponding frequency can be obtained by performing tests on a stationary cylinder.

## 2.4 Vortex-induced vibration

VIV of an elastically mounted cylinder in a flow is caused by the Karman vortex street (alternate shedding of vortices) generated downstream of the cylinder. As the vortices are shed from first one side and then the other, surface pressure forces are imposed on the cylinder. These oscillatory forces exerted on the cylinder cause the elastic structure to vibrate transverse to the flow direction (Friedman, 1997). Typically, when the vortex shedding frequency locks in with the natural frequency  $f_n$  of the system due to the increasing flow velocity, a region of relatively large-amplitude oscillations, called the lock-in region, can be observed (Seyed-Aghazadeh et al., 2017). Therefore, VIV is a limited-amplitude oscillation phenomenon that starts at a critical wind speed and disappears beyond a certain flow velocity (Mannini et al., 2014).

### 2.4.1 Harmonic model and non-dimensional parameters

The elastically supported cylinder exposed perpendicular to a fluid flow can be linearly modeled by a circular cylinder with diameter  $D$ , which is supported by a spring of stiffness  $k$  and a damper with damping  $c$ , as shown in Figure 2.2. As the cylinder vibrates, it traces out

the path shown, and for steady vibration, the length of path for one cycle is  $U_f/f$ , where  $f$  is the frequency of vibration.

The width of the path is  $2A_y$ , where  $A_y$  is the amplitude of vibration (Blevins, 1990). An equation of motion that can represent the oscillations of the cylinder in the transverse  $y$ -direction is

$$m\ddot{y} + \zeta\dot{y} + ky = F_L \quad (2.8)$$

where  $y$  is the displacement of the cylinder in the vertical plane from its equilibrium position, and  $\dot{y}$  and  $\ddot{y}$  its first and second time derivatives, respectively. The dimensionless  $F_L$  is defined by the lift coefficient as

$$C_L = \frac{F_L}{\frac{1}{2}\rho U^2 DL} \quad (2.9)$$

Because vortex shedding is a sinusoidal process, the motion of the cylinder is harmonic in time at the shedding frequency, meaning that  $L = \sin \omega t$ . When the natural frequency of the body is synchronized with the vortex shedding frequency, an approximation of the force  $F(t)$  is often given by

$$F(t) = F_0 \sin(\omega t + \phi) \quad (2.10)$$

where  $\phi$  is the phase angle between the fluid force and the body displacement; and of the response displacement  $y(t)$  as

$$y(t) = A \sin(\omega t) \quad (2.11)$$

where  $\omega = 2\pi f$  is the angular vortex shedding frequency and  $f$  the body oscillation frequency.

From Equations (2.8) - (2.11) the response amplitude ( $A^*$ ) and frequency ( $f^*$ ) can be derived as follows:

$$A^* = \frac{1}{4\pi^3} \frac{C_Y \sin \phi}{(m^* + C_A)\zeta} \left(\frac{U^*}{f^*}\right)^2 f^* \quad (2.12)$$

$$f^* = \sqrt{\frac{m^* + C_A}{m^* + C_{EA}}} , \quad (2.13)$$

as was done by Khalak and Williamson (1999), who made use of the non-dimensional parameters  $A^*$ ,  $U^*$ ,  $f^*$ ,  $C_Y$ , and  $m^*$  as defined in Nomenclature, and chose to use the natural frequency  $f_n$  in water.  $C_A$  is the potential added mass ( $m_A$ ) coefficient which, for circular cylinders, usually has a value of 1.0, and  $C_{EA}$  is an effective added mass coefficient that includes an apparent effect due to the total transverse fluid force in-phase with the body acceleration ( $C_Y \cos \phi$ ):

$$C_{EA} = \frac{1}{2\pi^3} \frac{C_Y \cos \phi}{A^*} \left(\frac{U^*}{f^*}\right)^2 . \quad (2.14)$$

The added mass is  $m_A = C_A m_d$ , where  $m_d$  is the displaced mass of fluid, that is  $m_d = \pi \rho D^2 L / 4$ , and where  $L$  is the length of the cylinder.

More recently, Govardhan and Williamson (2006) came up with an equation defining the non-dimensional amplitude as a function of mass damping and Reynolds number as follows:

$$A^* = (1 - 1.2\alpha + 0.3\alpha^2) \log(0.41Re^{0.36}) , \quad (2.15)$$

$$Re = \frac{\rho UD}{\mu} . \quad (2.16)$$

This equation, however, cannot be used for large mass damping values because it does not represent well low amplitude responses of order  $A^* \sim 0.1$ . The damping factor  $\zeta$  (defined in Section 4.2) characterizes the energy dissipated by a structure as it vibrates, which is often expressed as a fraction of 1, the critical damping factor. The mechanical damping of the system as well as the fluid-structure mass ratio greatly influence the response amplitude, and their combined effect is reflected by the Scruton number

$$Sc = \frac{m\zeta}{\rho D^2} . \quad (2.17)$$

## 2.4.2 Lock-in state

As mentioned by various researchers, vortex-induced vibrations take place within a limited range of flow velocities and their resulting vibration amplitudes are self-limiting (Mannini et al., 2014; Parkinson, 1989); the amplitude does not keep increasing with velocity. When the vortex shedding frequency ( $f_s$ ) is close to the natural frequency ( $f_n$ ) of the structure, their ratio  $f^*$  approaches unity,

$$f^* = \frac{f_s}{f_n} \approx 1 \quad (2.18)$$

indicating that the periodicity in the wake is synchronized with that of the system. This phenomenon is known as resonance.

### 2.4.2.1 Frequency synchronization

Synchronization can be defined as the matching of the frequency of the periodic wake vortex mode with the body oscillation frequency, meaning that the force frequency must match the oscillation frequency, that is, a condition known as lock-in state (Williamson & Govardhan, 2004). Under lock-in state, the feedback from the synchronized wake to the cylinder is intensified, leading to large response amplitudes of the elastically supported cylinder (Goswami et al., 1993). Feng (1968) did a thorough investigation on the relationship of the frequencies, displacement amplitudes, and surface pressures on an oscillating circular cylinder. He found out that the lock-in region and  $A^*$  both become smaller and occur at lower  $U$  values as the damping level of the cylinder is increased. Later, Goswami et al. (1993) studied the lock-in state of a circular cylinder by varying the flow velocities from well below the exact synchronization ( $f_s/f_n = 1$ ) velocity to above it. He states that the vortex-induced response of a cylinder can be divided into two major categories: locked-in and nonlocked-in. He found out that for nonlocked-in states, the spectrum of the vibration of the cylinder shows components at both frequencies  $f_s$  and  $f_n$ , while for lock-in state only the frequency  $f_s$  can be identified.

These phenomena can be seen in Figure 2.3, where the time histories and spectra of cylinder vibrations are shown for pre-lock-in (reduced velocities), lock-in, and after lock-in (higher velocities) range respectively.

#### **2.4.2.2 Influence of mass damping ratio on amplitude response**

The dynamic of the elastic system is influenced by the mass ratio ( $m^*$ ) and the structural damping ( $\zeta$ ), defined together as the mass damping ratio ( $\alpha$ ), and closely related to the Scruton number, as shown in Nomenclature. The response amplitude as a function of reduced velocity for various mechanical damping values can be seen in Figure 2.4, which shows the reduced velocity range over which lock-in state is present, that is, the velocity at which oscillation starts to occur, amplitude is maximum, and oscillation ceases to occur. As velocity is increased, the critical velocity at which lock-in starts to manifest remains almost unaffected by variations in mass ratio and mechanical damping, while the velocity at which lock-in terminates is decreased with increasing damping; the lock-in range becomes narrower for increasing damping. Therefore, for small Scruton numbers the lock-in range is wider whereas for high Scruton numbers it is narrower. However, Belloli et al. (2015) obtained three different curves each with different maximum amplitude at the same Scruton number, which confirms that the Scruton number cannot be the only parameter that identifies the maximum response of the cylinder in lock-in region.

For high mass-damping ( $m^*\zeta$ ) systems, Feng (1968) found two amplitude branches over a range of reduced velocities, the “initial” branch, and the “lower” branch, with a hysteretic transition between them. On the other hand, Khalak and Williamson (1997) found that for VIV of a cylinder on a low mass-damping system there exist three amplitude branches, the “initial” branch, the “upper” branch, and the “lower” branch, with a hysteretic transition between the initial and upper branches. They compared their result at  $m^*\zeta = 0.013$  with that of Feng (1968) at  $m^*\zeta = 0.36$ , confirming the existence of two types of amplitude response:

three branches (initial, upper, and lower) are present for low mass damping; there is no upper branch, and only the initial and lower branch exist for high mass damping. This is seen in Figure 2.5 which shows the typical two-branch and three-branch response plots for high mass-damping and low-mass damping, respectively.

### 2.4.3 Vortex patterns

When a cylinder oscillates perpendicularly to the flow, the vortex patterns are different from the classical Karman vortex street. The work done by Williamson and Roshko (1988) using forced vibrating cylinders defined a set of regimes for vortex wake modes. The flow can be categorized into two modes: 2S and 2P. In the 2S mode, two single vortices per cycle are formed, whereas for the 2P mode, two pairs of vortices per cycle are formed. They are dependent on two parameters, the wavelength ratio  $\lambda^* = \lambda/D$  and the amplitude ratio  $A^*$ . Depending on the amplitude response, the vortex wake pattern can be given as 2S, 2P, and P + S modes, which are the principal modes near the lock-in region. A map of these regimes is shown in Figure 2.6 in which the 2S mode corresponds to the initial branch, and the 2P mode is associated with the lower or upper branch.

### 2.4.4 Effects of Reynolds number

The interaction between the cylinder and the incoming flow is also affected by the Reynolds number. Many studies have focused on the effects of flow at low  $Re$ ; nonetheless, in more recent years, due to the improvement of experimental and CFD techniques, the investigation of wake flow over bluff bodies at high  $Re$  has been flourishing. For flows of  $Re > 1 \times 10^5$  around a circular cylinder, there exist at least four different regimes: subcritical, critical, supercritical and transcritical. The subcritical is the lowest regime which ranges up to  $Re \approx 2 \times 10^5$ , within which the shedding usually happens in a regular manner. In this regime the drag coefficient is high, about 1.2, yielding a Strouhal number of about 0.2 (Bearman, 1969).

### 2.4.4.1 Amplitude response

According to Govardhan and Williamson (2006), Reynolds number is a key parameter for determining the peak-amplitude response. The ‘peak amplitude’ ( $A_{max}^*$ ) is defined as the maximum amplitude ratio evaluated over a complete amplitude response plot, as normalized velocity is varied, for a particular mass and damping and Reynolds number. By looking at time history of cylinder oscillation (Figure 2.7 b)), corresponding to the flow speed at which peak oscillation amplitude is found, it can be seen that as Re is increased, the oscillation amplitude increases as well, producing larger fluctuations in amplitude. In addition, the variation of  $A^*$  with mass damping for three different given Re are plotted in Figure 2.7 a), clearly showing that curve shifts upwards for higher Re. Consequently, the jumps in amplitude between the different branch responses are larger at higher Re, because the upper branch amplitude increases with Re.

### 2.4.4.2 Vortex formation

The development of the near wake flow and the physical evolution of the wake of a bluff body are influenced by the vortex formation region, which is the region of the flow where vortex shedding is initiated at all Reynolds numbers. When the flow is in the critical Reynolds number regime, regular vortex shedding happens and the vortex shedding frequency is clearly defined. However, the regular shedding ceases to happen as Re increases due to the three dimensionality of the flow caused by turbulence generated around it (Bearman, 1969).

Depending on the Re values, the vortex formation region length will be altered; nevertheless, it is important to notice that there exist many definitions for this (its extent in the streamwise direction) in the literature:

- The minimum of the mean pressure on the wake axis or centerline (Roshko, 1955).
- The maximum of the wake velocity fluctuation at the fundamental shedding or Strouhal frequency off the wake centerline (Schaefer & Eskinazi, 1959).

- The maximum of the wake velocity fluctuation at twice the shedding frequency on the wake centerline (Gerrard, 1966).
- The minimum cross-stream or lateral spacing, close to the body base region, of the maxima of the velocity fluctuation field (Bearman, 1965).

All of which have been reconciled by the study of Griffin (Griffin, 1995), whose results showed that they agree well with each other for  $Re$  up to 350. So, by using any of these measures, the formation length or the effective position of shedding is in accordance with the location of maximum vortex strength.

## 2.5 Stationary versus vibrating cylinders

The flow behavior and characteristics of the wake and vortex shedding for a stationary and vibrating cylinder are very different. The main feature of an elastically mounted cylinder is the formation of “jets” that stimulate the formation of vortices. A jet is a narrow stream of flow with a high velocity. The dynamics of the shedding process in the initial branch was described by Hsieh et al. (2017), who used visualization techniques to observe it qualitatively. As the cylinder moves from its highest amplitude to its initial position, part of the incoming flow passes beneath the cylinder and creates a jet in the upward direction. This jet forces the lower vortex to convect downstream, and at the same time forms a new vortex with counterclockwise direction on the upper side of the cylinder. This process is repeated, but with opposite direction, as the cylinder moves upwards.

Some important differences between the two types of system are mentioned in the following lines. For the stationary case, the vortices are formed from the upper and lower shear layers behind the cylinder, forming the Karman vortex street downstream. In contrast, for the vibrating case, vortices are formed by oblique jets, which intrude upon the formation zone and influence the wake flow downstream. A recirculation zone appears downstream of the stationary cylinder, wherein vortices are formed, while for the vibrating case no recirculation

zone can be found just downstream. Yet, in the near wake region ( $x/D < 5$ ), with same velocity, the size of the affected region is wider for the vibrating cylinder than for the stationary cylinder. It also has been detected that the patterns of the velocity profiles are very different between both cases; for a vibrating cylinder the values of  $u$  at the  $x$ -axis are larger than those away from the  $x$ -axis for  $x/D < 4$  (Hsieh et al., 2017).

It is clear that the wake flow behavior of a vibrating system is much more complex than that of a stationary one. Thus, to understand better the characteristics of a vibrating cylinder, it is important to carry out qualitative measurements of the flow field using visualization techniques, as well as quantitative measurements.

## **2.6 Turbulence spectra and length scales**

Turbulence is an instability generated by shear, which leads to large scale disturbances in the flow field, consisting of random velocity fluctuations. A turbulent flow is random, chaotic, rotational, and three-dimensional. It is characterized by high levels of fluctuating vorticity (Tennekes & Lumley, 1989). From previous concepts and definitions introduced, it is well understood that a fluid flowing over a circular cylinder is separated from the surface due to the unstable shear layers generated at the separation points, forming a wake region with vortices. This signifies that the flow behind a circular cylinder is turbulent. Turbulence can be described in terms of an energy cascade in which vortices of large scale dissipate into smaller scales until the viscous effects dominate and the turbulence energy is dissipated into heat (El-Gabry et al., 2014).

### **2.6.1 Energy cascade**

The turbulent flow after a circular cylinder comprises of eddies with a wide spectrum of spatial and temporal scales. The largest turbulent eddies are typically scaled with the cylinder dimensions, and extract energy from the mean flow. The large eddies are broken down into

smaller eddies, which in turn are broken down into even smaller eddies. This process continues until the eddies reach their smallest size at which viscous effects become dominant and are damped out by viscosity. The smallest eddies are known as Kolmogorov dissipation scales. In a similar manner, the kinetic energy is fed from the mean flow into large eddies and continues to cascade down to smaller eddies until they reach the Kolmogorov dissipation scale, a process known as energy cascade, shown in Figure 2.8 (Brennen, 2006; Ekman, 2020). Due to this process, the flow eventually reaches a fully developed state, in which the disturbance energy for any one size of eddy becomes relatively constant.

## 2.6.2 Turbulence spectra

It is possible to examine the energy cascade process further by setting a probabilistic framework in which fluid velocities and pressures are decomposed into mean and fluctuation components.

$$u_i = \bar{u}_i + u'_i \quad , \quad p = \bar{p}_i + p'_i \quad (2.19)$$

Each velocity component ( $u, v, w$ ), as well as all the components of the stress tensor ( $\sigma_{ij}$ ) can be decomposed in a similar manner. As explained by Brennen (2006), the mean components are defined by averaging the quantity over a period of time,  $T$ , which is much larger than any of the periods of the turbulent fluctuations so that

$$\bar{u}_i = \frac{1}{T} \int_t^{t+T} u_i dt \quad , \quad (2.20)$$

so it necessarily follows that

$$\frac{1}{T} \int_t^{t+T} u'_i dt = 0 \quad . \quad (2.21)$$

By means of the turbulent motions,  $u'_i$ , the kinetic energy  $KE$  is defined by

$$KE = \frac{1}{2} \overline{u'_i u'_i} \quad (2.22)$$

which is visualized as being distributed either spatially over eddies of many sizes ( $k$ ) or over eddies of many frequencies ( $\omega$ ). Thus, a turbulent energy density can be defined as

$$KE = \int_0^{\infty} e(k) dk \quad \text{or} \quad KE = \int_0^{\infty} e(\omega) d\omega \quad (2.23)$$

Hence, a spectrum of the turbulent fluctuations can be obtained by plotting  $e(k)$  against  $k$  or  $e(\omega)$  against  $\omega$ .

### 2.6.3 The -5/3 Kolmogorov law of turbulence

As mentioned in the literature (Brennen, 2006; Lewandowski & Pinier, 2016), Kolmogorov presumed the existence of an intermediate range of wavenumbers, called the “inertial subrange”. In Figure 2.9 (obtained from Brennen (2006)) the amplitude of the turbulent energy density is plotted against the frequency of those fluctuations, showing that the energy of large eddies at low frequencies cascades down as the frequency increases until they reach their smallest size at high frequencies and are completely damped out. Moreover, it illustrates the three different ranges that can be observed from a turbulence spectrum, namely: the energy-containing range, where the mean flow is creating large eddies; the inertial range, where neither the mean flow creation nor the viscosity are explicitly important; and the dissipation range, where eddies are dissipated by viscosity. The inertial range is governed by the -5/3’s law. This law states that for homogeneous and isotropic turbulence, in the inertial range, the energy density of the flow  $E = E(k)$  at a given point  $(t, x)$  is driven by the dissipation  $\mathcal{E}$  and behaves like  $C^{te} k^{-5/3}$ . (For a detailed derivation of the Law of the -5/3 see the work by Lewandowski and Pinier (2016)).

### 2.6.4 Turbulence length scales

Turbulence length scales can provide further information regarding the properties of a turbulent fluid flow; they are used to characterize their spectra and processes. Each range within the spectra is characterized by a length scale of eddies. The integral length scale (macro-scale),

present within the energy-containing range, is a measure of the largest eddy size in a turbulent fluid, defined by Roach (1987), as

$$\Lambda_x = \left[ \frac{E(f) U_{mean}}{4\bar{u}^2} \right]_{f \rightarrow 0} \quad (2.24)$$

where  $\bar{u}$  is the standard deviation of the streamwise velocity.

The inertial range corresponds to the dissipation length scale or Taylor microscale, a critical intermediate eddy size below which viscosity begins to damp out the eddies. It is considered as the “smallest large scale”, a measure of the average dimensions of the eddies that are responsible for the dissipation of turbulent energy (Pouransari et al., 2014). The Taylor length scale can be calculated from the power spectrum, considering the turbulence field is homogeneous and isotropic, as shown by Roach (1987):

$$\frac{1}{\lambda_x^2} = \frac{2\pi^2}{U^2 \bar{u}^2} \int_0^\infty f^2 E(f) df \quad (2.25)$$

Lastly, the smallest turbulence length scale is the Kolmogorov microscale  $\eta$ , present in the dissipation range of the energy density spectrum, defined as

$$\eta = \left( \frac{\nu^3}{\epsilon} \right)^{1/4} \quad (2.26)$$

where the parameters governing the small-scale motion include:  $\epsilon$ , the viscous dissipation rate per unit mass ( $\text{m}^2 \text{sec}^{-3}$ ), and  $\nu$ , the kinematic viscosity ( $\text{m}^2 \text{sec}^{-1}$ ) (Tennekes & Lumley, 1989).

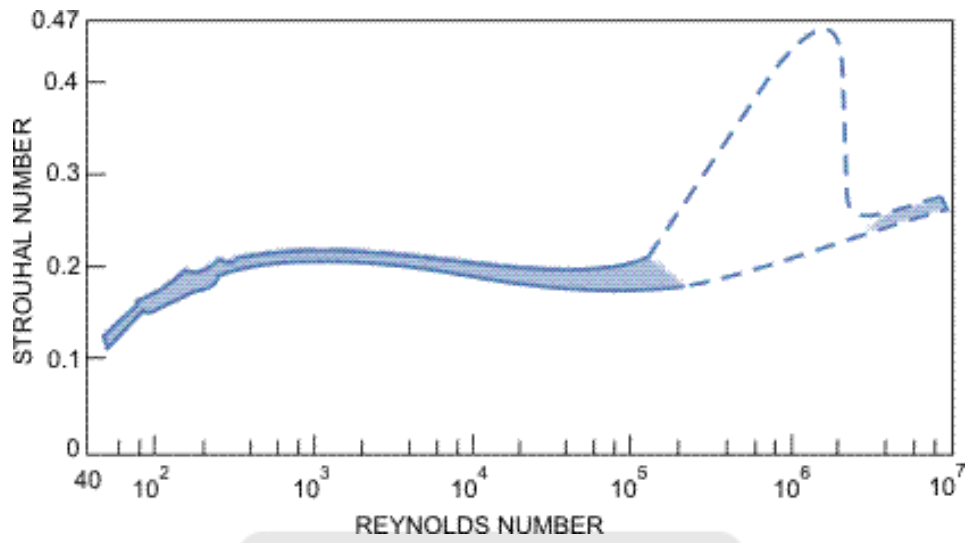


Figure 2.1. Strouhal number vs Reynolds number for circular cylinders (Blevins, 1990).

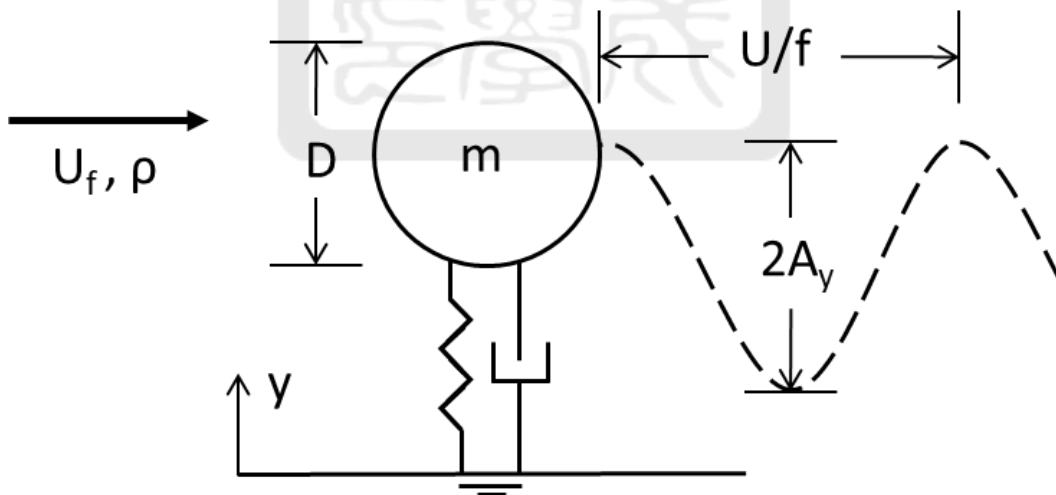


Figure 2.2. Vibration of a two-dimensional, spring-supported, damped model in steady flow.

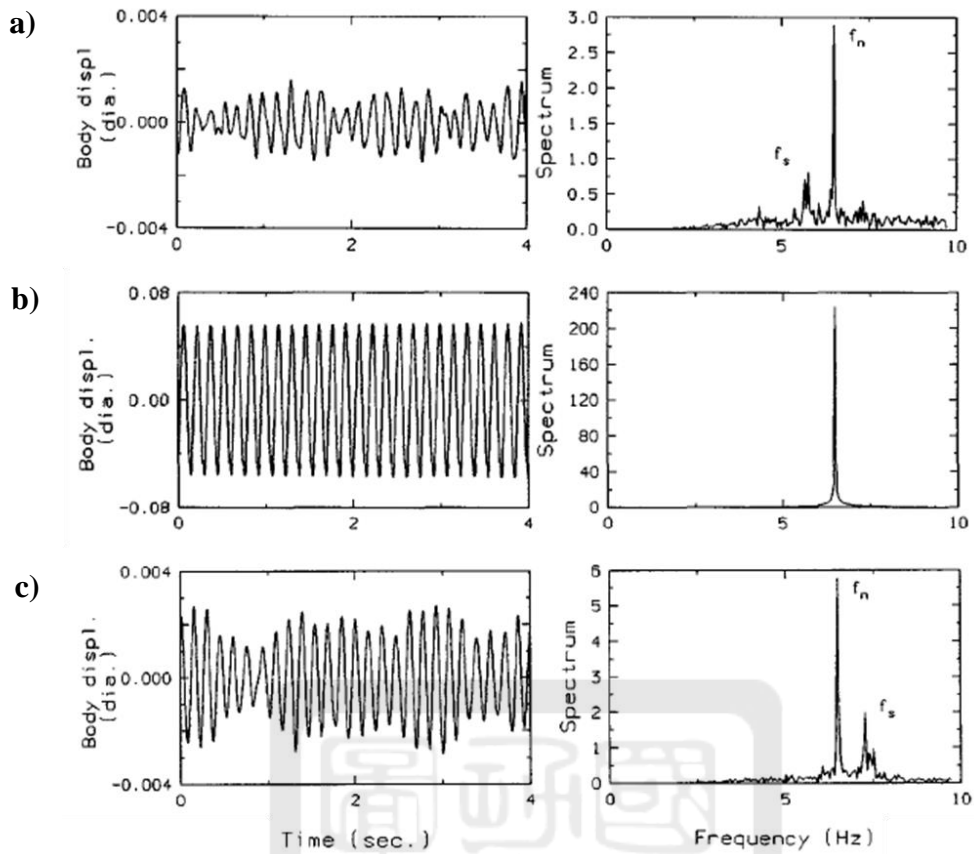


Figure 2.3. Time history and cylinder vibration spectrum at a) pre-lock-in, b) lock-in, and c) after lock-in states (Goswami et al., 1993).

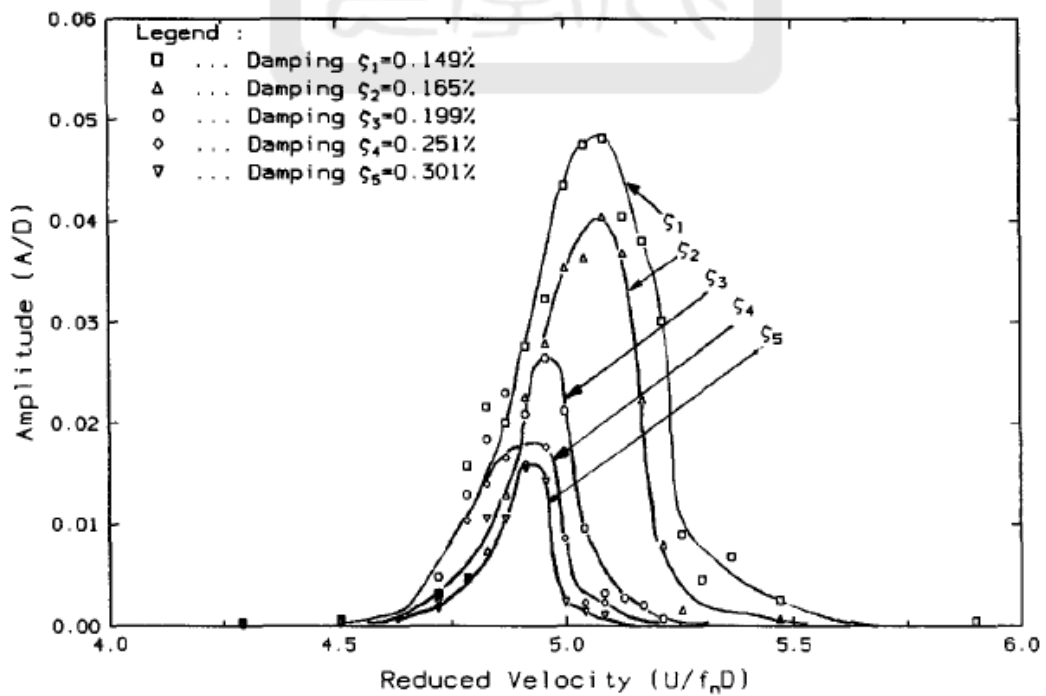


Figure 2.4. Amplitude vs reduced velocity for different structural damping (Goswami et al., 1993).

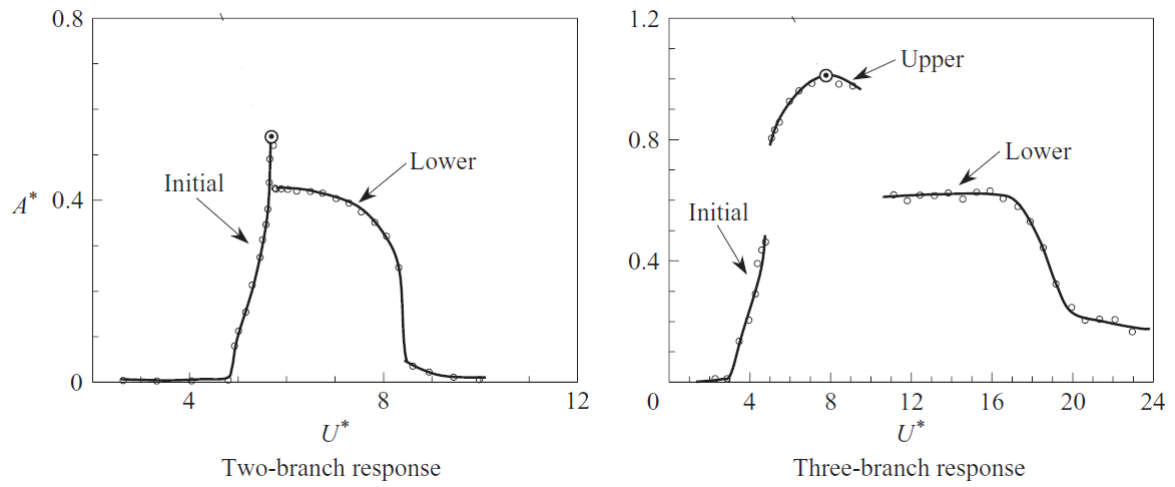


Figure 2.5. a) Two-branch response plot for high mass damping values. b) Three-branch response plot for low mass damping values (Govardhan & Williamson, 2006).

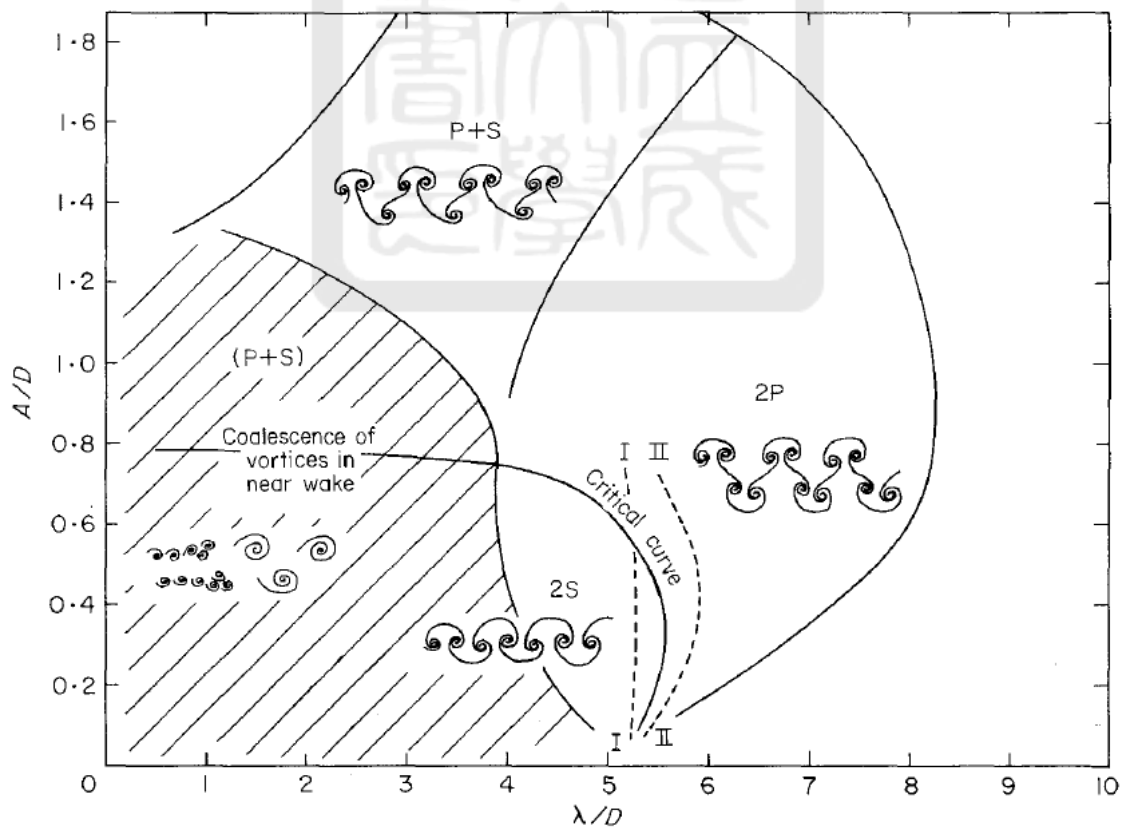


Figure 2.6. Map of regimes for the different vortex modes (Williamson & Roshko, 1988).

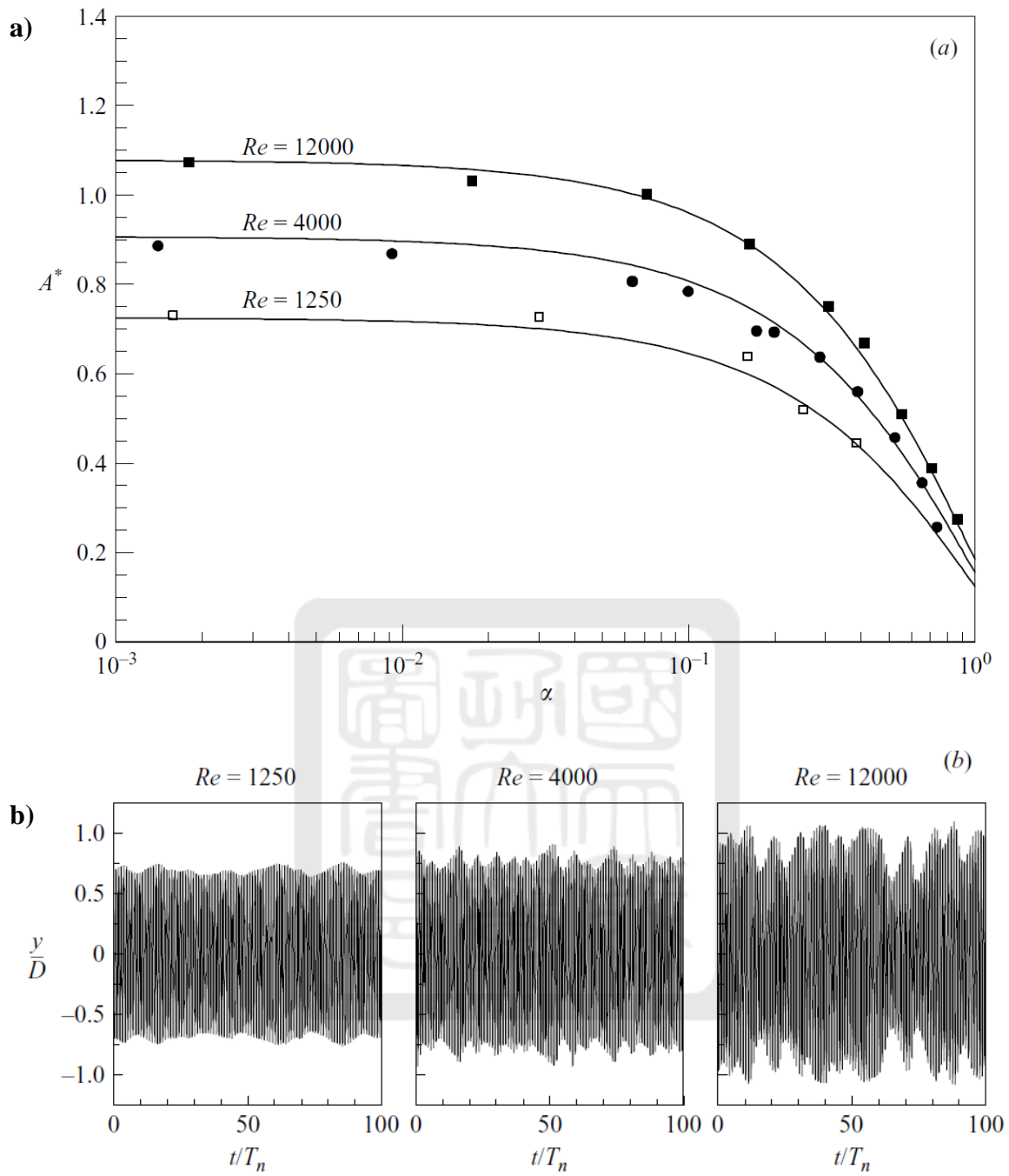


Figure 2.7. a) Amplitude vs mass damping ratio curves for constant  $Re$ , and b) Displacement traces at zero mass damping for different  $Re$ . Mass is kept constant  $m^* = 10$ . From (Govardhan & Williamson, 2006).

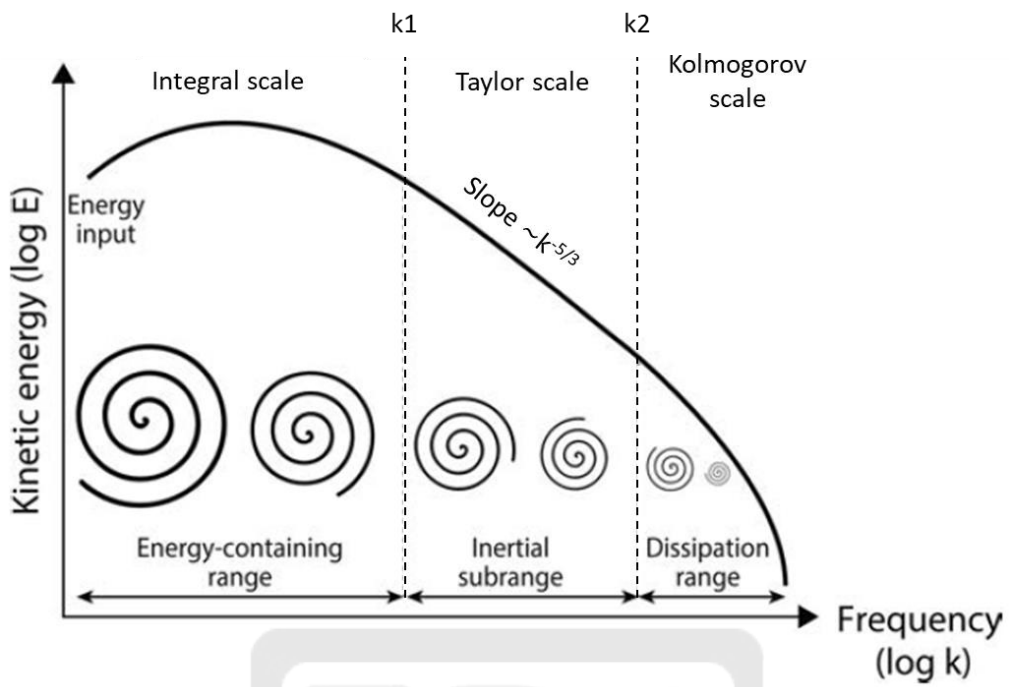


Figure 2.8. A typical energy spectrum of turbulent flow depicting the energy cascade process. It is divided into three different ranges, each corresponding to a different length scale of eddies.

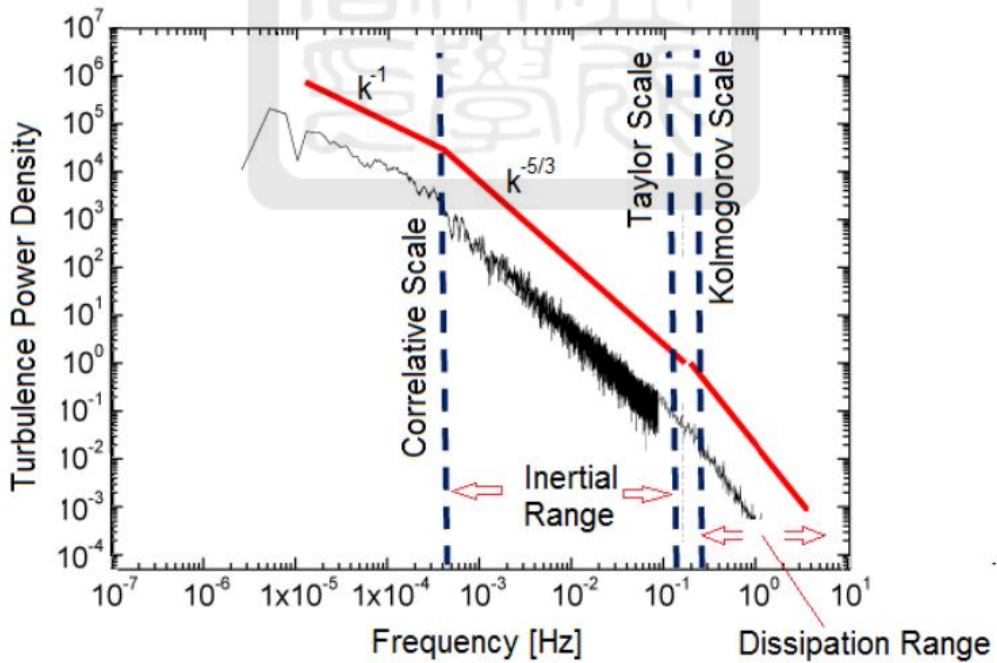


Figure 2.9. A turbulence spectrum and its characteristics. The behavior of the spectra in the inertial range follows the  $-5/3$  Kolmogorov law of turbulence.

## Chapter 3 – Experimental facility and methodology

The equipment used to carry out the experiments of this study, as well as the instruments, are described in this chapter, such as the wind tunnel, the models and their mechanism, the PIV system, the HWA system, and the analysis software. Furthermore, a detailed explanation of the process used, and the analysis approaches implemented are explained.

### 3.1 Wind tunnel

The experiments of this study were performed in a closed-circuit low-speed wind tunnel located in the Aerospace Science and Technology Research Center (ASTRC) of National Cheng Kung University (NCKU) at Guiren Campus in Tainan. It is composed of a fan that keeps the air flowing; a diffuser that deaccelerates the flow; guiding vanes that turn the air in the corners; a settling chamber comprised of three screens and one honeycomb that help reduce the turbulence level in the flow before it enters the contraction section; a nozzle that accelerates the flow; and a test section where the tests are carried out (see Figure 3.1).

The maximum velocity of this wind tunnel is 67 m/s. It is equipped with a variable pitch fan, meaning that the wind speed can be adjusted by controlling the pitch angle of the fan blades as well as by regulating the rotation frequency of the fan. The total circuit length of the tunnel is approximately 80 meters. Its nozzle has a contraction ratio of 9, and the test section has a rectangular cross section with height of 1.2 m, width of 1.8 m and length of 2.7 m. The test section has nine acrylic windows throughout the bounded wall that allow visual observations and PIV measurements: three on each side wall of the section and three on the upper wall. Over the top of the test section, a structure holds the PIV system, of which laser sheet passes through the central top window, parallel to the side walls of the wind tunnel.

## 3.2 Cylinder models

The non-dimensional parameters used to describe the characteristics of the fluid-structure interaction response depend on different fluid properties (velocity, density, viscosity) and structure properties (dimensions, mass, damping, natural frequency). For this reason, the design of the models and the experimental setups is of great importance. Two different solid circular cylinders were used in this study.

One cardboard tube with outer diameter  $D_o = 0.042\text{ m}$ , and length  $L = 0.9\text{ m}$  was used for the static tests (Model 1). A stainless-steel tube with outer diameter  $D_o = 0.022\text{ m}$ , inner diameter  $D_i = 0.014\text{ m}$ , and length  $L = 2.1\text{ m}$ , was positioned at its longitudinal axis to ease its assembling. The blockage ratio given by the model is 2.7%, and its corresponding length to diameter ratio is about 21, which is large enough to ensure two-dimensional flow in the central part of the near wake region of the cylinder (Hsieh et al., 2017). This model, which span covers the whole width of the test section, was used to conduct a vibrating experiment using a system of four springs located outside the test section. However, it was observed that the cylinder bended while it was oscillating, hence, another circular cylinder, as well as a new aeroelastic structure (to be described in Section 3.5.2), was designed for the vibrating experiments.

A shorter and thicker acrylic cylinder tube used for the vibrating tests, was designed in order to avoid the bending effects produced by the oscillation of the structure. For its design, the Strouhal number obtained from the fixed experiments ( $St = 0.197$ ) was used as a benchmark to calculate the model dimensions, in such a way that the structural natural frequency matches the vortex shedding frequency, in order to attain the lock-in state during oscillation. The vortex shedding frequency is obtained from the definition of Strouhal number,

$$f_s = \frac{StU_f}{D}. \quad (3.1)$$

Because the angular frequency is determined as

$$\omega = 2\pi f_s = \sqrt{\frac{k}{m}}, \quad (3.2)$$

the natural frequency of the structure can be related to the vortex shedding frequency:

$$f_n = \frac{1}{2\pi} \sqrt{\frac{k}{m}} = \frac{\omega}{2\pi} = f_s. \quad (3.3)$$

The mass of each component of the model was also taken into account during the calculations. After comparison of different values and their corresponding expected frequency, the dimensions that best suit our purposes were selected.

The new model (Model 2) is composed of an acrylic tube with  $D_o = 0.1 \text{ m}$ ,  $D_i = 0.094 \text{ m}$  and  $L = 1.215 \text{ m}$ ; a stainless steel tube that passes through the longitudinal axis of the acrylic tube, with the same outer and inner diameter as that used in the fixed test, that is  $D_o = 0.022 \text{ m}$ ,  $D_i = 0.014 \text{ m}$ , and of length  $L = 1.4 \text{ m}$ . Ten wood plates of thickness  $t = 0.0065 \text{ m}$  act as ribs, connecting the steel tube and the acrylic tube. Because the model is supported within the test section, to impose two-dimensional flow conditions, circular acrylic plates of  $0.3 \text{ m}$  in diameter were attached at the model ends. Its total mass, including the end holders that connect the model to the springs, is  $m = 5.42 \text{ kg}$ . The blockage ratio given by the model alone is 5.6%, and its slenderness ratio,  $L/D$ , is 12, which is capable of yielding wake flow with two dimensional characteristics at the spanwise central region (Lin et al., 2012). The mass ratio of this model is  $m^* = 472$ , which is considered as a high mass ratio, as compared to those employed by Williamson and Govardhan (2004). The CAD design and the actual model can be seen in Figure 3.2 and Figure 3.3. Furthermore, the necessary stiffness of the aeroelastic system was calculated and the springs were designed based on it, which will be explained in Section 3.5.2.

### 3.3 Methodology

This study discusses the different characteristics in the wake of a static and a vibrating circular cylinder. The static and vibrating experiments were both conducted with a free stream velocity,  $U_f$ , ranging from 4 m/s to 6 m/s ( $U^* = 4.1 - 6$ ), corresponding to a maximum Reynolds number (based on the diameter of the cylinder) of  $1.3 \times 10^4$  and  $3.2 \times 10^4$ , respectively. Both cases were in the subcritical wake regime (Bearman, 1969). This range corresponds to the lock-in state range, where the frequency ratio  $f^*$  remains close to unity. Hence, at resonance, the parameter  $U^*/f^* = U/fD \approx U/f_s D = 1/St$ , suggests a resonance at the normalized velocity  $U^* \approx 5 - 6$  (Williamson & Govardhan, 2004). The streamwise stations selected to perform measurements were located at  $x/D = 4$  and  $x/D = 6$  downstream from the surface of the model.

First, the static tests with particle image velocimetry and hot wire anemometry were carried out and their results were compared to make sure that both instruments can yield correct measurements. Particle image velocimetry was used to measure the two-dimensional instantaneous velocity field in the near wake region. The cross-type hot wire anemometer was placed in several positions ( $y/D = 0$  to 4) behind the model in order to derive the power spectral density of the streamwise velocity fluctuations in the wake. The calibration of the HWA is made following the polynomial curve fitting method, as will be explained in Section 3.4.2.1.

Measurements made with the HWA are compared with measurements using a pitot tube, by means of a pressure transducer DP103-18, to check its reliability. The pressure transducer was calibrated using a DPI610 pressure calibrator. The X-type HWA data serves as a comparison basis for identifying the accuracy of the employed PIV measurements. After confirming the correctness of the measurement instrumentation utilized, PIV and HWA vibrating tests were performed.

For the case of the vibrating tests, in addition to PIV and HWA systems, the displacements of the model were recorded with three non-contact lasers. The damping and natural frequency of the system were first measured imposing several times an initial condition and recording the free decay of the oscillations in still air. The cylinder was excited to oscillate freely by applying an initial displacement. The natural frequency of the structure is  $f_n = 9.7 \text{ Hz}$ , so the expected resonance velocity can be calculated using Equation 3.1, yielding a value of  $U = 5.2 \text{ m/s}$ . While the damping is  $\zeta = 0.005$ .

### **3.4 Velocity measurement instrumentation**

In this study, a PIV system and a hot wire anemometry were used to visualize and measure the flow field. Both systems are explained in detail along this section, as well as each of their components.

#### **3.4.1 Particle Image Velocimetry (PIV)**

Particle image velocimetry is an indirect nonintrusive method since the data is obtained from the foreign particles (seeding or tracer particles) instead of the fluid flow itself. The PIV system comprises a continuous-type green color laser (Green DPSS 532 nm Laser, Figure 3.4), with an output power of 5W and wavelength of 532 nm, as the light source; a high-speed camera (Photron FASTCAM SA-X, Figure 3.5); and a personal computer to acquire and save data. The beam emitted from the laser source is reflected by a custom-made mirror (Figure 3.6) that turns the horizontal laser beam into a vertical laser sheet of about 3 mm in thickness and with a  $45^\circ$  spread angle, cast downward into the test section through the upper central acrylic window. The camera, which memory has been recently upgraded and can now take up to 43000 pictures, is equipped with a Nikon NIKKOR 50 mm f/1.2 lens (Figure 3.7) for image acquisition. The parameters were set according to the Nyquist theorem, which states that to avoid the problem of aliasing statistics, the frame rate must be at least twice as fast as the

frequencies of small turbulent eddies such as that of Taylor-scale eddy (Bendat & Piersol, 2011).

For the static tests, the frame rate was set at 2000 fps, associated with a spatial resolution of  $1024 \times 1024$  pixels. The exposure is dependent on the shutter speed of the camera. Considering the tradeoff between acquiring enough intensity on the imaging sensor and reducing the blurred image of particles (Boillot & Prasad, 1996), it was set to be the smallest possible for each case (different fps influence this value). For the case of the vibrating test, because the diameter of the model is larger and thus the shedding frequency is smaller, the frame rate used was 1000 fps. The spatial resolution was  $1024 \times 1024$  pixels.

### 3.4.1.1 Seeding system

The seeding material utilized are aluminum oxide ( $Al_2O_3$ ) particles. A custom-made seeding injector with an airfoil-shape cross section was used to feed the tracer particles into the airflow in the upstream region in front of the model, aligned with the laser sheet (Figure 3.8). The particle seeding device used is a cyclone particle generator developed by Shih et al. (2016). It is essentially a cylindrical crystal container filled with the tracer particles to which compressed air is injected from the bottom in such a manner that generates a swirl upwards expelling the tracer particles into the seeding injector, illustrated in Figure 3.9. The mass flow rate is controlled by adjusting the air entrance rate from the compressor tank.

An important scaling parameter in fluid-particle flows is the Stokes number (denoted as  $Stk$  in this study). Turbulent dispersion and inter-particle collisions are two factors that may interfere with particle dynamics in a turbulent particle-laden flow field. The Stokes number, which is the ratio of particle response time  $\tau_p$  to a time characteristic of the fluid motion  $\tau_f$ , can describe the extent of turbulence dispersion. That is

$$Stk = \frac{\tau_p}{\tau_f} = \frac{\rho_p d_p^2}{18\mu} \cdot \frac{U_f}{l_0}, \quad (3.4)$$

where the times are defined as follows:

$$\tau_p = \frac{\rho_p d_p^2}{18\mu} \quad (3.5)$$

and

$$\tau_f = \frac{U_f}{l_0} \quad (3.6)$$

where the subscript  $p$  and  $f$  denote the particles and fluid, respectively;  $l_0$  is the characteristic length of the model (usually diameter).

A small Stokes number ( $Stk \ll 1$ ) implies that the particles can maintain near dynamic equilibrium with the carrier fluids while a large Stokes number ( $Stk \gg 1$ ) suggests that the particle motion is unaffected by the carrier flow field, so it does not follow the real path of the fluid flow. For good tracing capabilities, the nominal mean size of the tracer particles used had better be less than 10  $\mu\text{m}$ . This ensures that the Stokes number of the seeding particles is sufficiently smaller than unity, which implies that the particles are capable of following the carrier fluid motion faithfully. In this case, the highest Stokes number was estimated to be 0.070 for Model 2, at the highest wind speed tested, 5.9  $\text{m/s}$  ( $U^* = 6$ ;  $Re = 3.8 \times 10^4$ ).

### 3.4.1.2 Analysis software

The software PIVview 2C/3C, developed by PIVTEC GmbH, was used to perform image analysis of the PIV recordings. The local flow velocity  $u$  at a point  $(x, y)$  is computed by measuring the displacement  $\Delta x$  of a group of tracer particles during a short time interval  $\Delta t$ :

$$u = \frac{\Delta x}{\Delta t} = \frac{\Delta X}{MF \Delta t} \quad (3.7)$$

MF is the magnification factor, which allows converting the displacement  $\Delta x$  in the object space to that in the image plane, indicated with  $\Delta X$ . The magnification factor MF was equal to 2.014, which generates a spatial resolution of 0.381 mm/pixel for the image, meaning that the apparatus used is capable of performing PIV measurements at higher frame rates.

The spatial resolution of the PIV depends on the employed size of the interrogation window. In this study, the analysis of cross correlation of image pairs was applied to determine the velocity fields (Adrian, 1991). The multi-grid refinement method was adopted to augment the accuracy of the velocity calculation, and window deformation was performed to reduce the error that is induced by velocity gradient in the flow. The choice for the final interrogation window size depends on the particle image density. The final interrogation window of the process must be higher than the value obtained by the equation:

$$Window\ size = \frac{4\ U\ MF}{sampling\ rate} \times 1000 \quad (3.8)$$

For low velocities it was  $32 \times 32$  pixels, while for higher velocities the final window size was  $64 \times 64$  pixels.

Furthermore, the median mask of smoothing filter was employed during data analysis to eliminate the impulse noise in the image. This filter replaces the value of a pixel by the median of the gray level in the neighborhood for each mask. However, the use of a large mask in the median smooth might result in “mosaic” image, because its function is similar to a low-pass filter that may lead to the loss of high spatial frequency signals (Gonzalez, 2002). For this reason, the size of the median mask was meticulously selected to be  $3 \times 3$ .

### 3.4.2 Hotwire anemometry

To carry out HWA measurements, the StreamLine Pro CTA system of Dantec Dynamics was used (Figure 3.10). It comprises of a mainframe (90N10) with a temperature probe and two modules of constant temperature anemometer (CTA, 90C10). The analogue signals were processed by a NI BNC-210 terminal block (Figure 3.11). The hot wire probe used in this study is a straight X wire probe (DANTEC 55P61). This probe mounts with its axis parallel to the direction of the air flow, so that the predominant flow vector attacks the two wires, each, with an angle under  $45^\circ$ . It has two platinum-plated tungsten wire sensors of  $5\ \mu\text{m}$

diameter and 1.25 mm long, which are arranged in X-array, where they form an angle of 90° with one another. The body of the probe is a 2.3 mm-diameter ceramic tube, equipped with gold-plated connector pins that connect to the probe supports by means of plug-and-socket arrangements. It is marked with one and two dots to indicate the sensor number (Figure 3.12). According to the hot-wire manual offered by DANTEC Dynamics (*Miniature Wire*, 2021), this type of probe can be used to measure two-dimensional flows of low turbulence intensity; however, the angle of the flow vector is limited within  $\pm 45^\circ$ .

### 3.4.2.1 HWA calibration

A pitot tube was used to calibrate each sensor by means of the variable-frequency wind turbine and the pressure calibrator DPI610 (Figure 3.13). This calibration allows to establish a relation between the CTA output and the flow velocity. In this study, the calibration is done following the procedure of the practical guide from DANTEC Dynamics (Jorgensen, 2002). The probe is exposed to a set of known velocities  $U$ , and the voltages  $E$  are recorded. These points  $(E, U)$  are used to obtain a curve fit that represents the transfer function to be used when converting data records from voltages into velocities. It is important to keep track of the air temperature, which should not vary greatly from calibration to measurement (with moderate temperature changes of  $\pm 5^\circ C$ ).

The calibrated relations of the velocities  $U_{cal,i}$ , and the output voltage of each sensor  $E_i$ , are given by a polynomial equation in the 4<sup>th</sup> order:

$$U_{cal,i} = C_{0,i} + C_{1,i}E_i + C_{2,i}E_i^2 + C_{3,i}E_i^3 + C_{4,i}E_i^4, \quad i = 1, 2. \quad (3.9)$$

The instantaneous velocities defined by the sensors are:

$$U_1 = \frac{\sqrt{2}}{2} \sqrt{(1 + k_2^2) \cdot U_{cal,2}^2 - k_2^2 \cdot U_{cal,1}^2}, \quad (3.10)$$

$$U_2 = \frac{\sqrt{2}}{2} \sqrt{(1 + k_1^2) \cdot U_{cal,1}^2 - k_1^2 \cdot U_{cal,2}^2}, \quad (3.11)$$

which are used to calculate U and V velocity components in the x and y-direction, respectively, as follows:

$$U = \frac{\sqrt{2}}{2} \cdot U_1 + \frac{\sqrt{2}}{2} \cdot U_2 \quad (3.12)$$

$$V = \frac{\sqrt{2}}{2} \cdot U_1 - \frac{\sqrt{2}}{2} \cdot U_2 \quad (3.13)$$

In these equations, the default values from DANTEC Dynamics for yaw-coefficients are  $k_1^2 = k_2^2 \cong 0.04$  (Jorgensen, 2002).

The sampling rate used for flow measurements was 10 kHz, and a total of 300,000 raw data samples were captured. Turbulence statistics were computed utilizing the total number of samples to assure stationary results.

An X-type HWA probe can sense correctly one-quadrant-plane ( $\pm 45^\circ$ ) flow direction only (Jorgensen, 2002). To obtain confident measurements very upstream in the near-wake region, where the recirculation zone with high instantaneous flow angles is present, a criterion based on the flow angle is necessary to be set. It states that the instantaneous flow angle ( $\beta$ ) must fall within the condition  $|\beta| \leq 45^\circ$ ; otherwise, the data should be discarded. It is calculated from the instantaneous streamwise and lateral velocity components, U and V, respectively, as

$$\beta = \tan^{-1} \left( \frac{V}{U} \right). \quad (3.14)$$

This criterion was corroborated by Chen and Chang (2018), whose results demonstrate that the cross-type HWA is incapable of providing accurate measurements in the very upstream regions ( $x/D < 2$ ) due to high instantaneous flow angles. Hence, the HWA measurements of this study are considered confident at the stations  $x/D \geq 4$ . This was reassured by determining the percentage of raw data number satisfying the condition of  $|\beta| \leq 45^\circ$  at both streamwise stations of  $x/D = 4$  and 6 for the static case. In this case, the uncertainty of the HWA system

was considered to lessen the criterion for confident HWA data; that is, the set of raw data must contain more than 97.5% of the total raw data (300,000) that satisfy the condition  $|\beta| \leq 45^\circ$ . It is observed in Figure 3.14 that, for both stations, the percentages of raw data number exceed 97.5% for the whole sectional domain. It means that confident measurements can be achieved with the X-type HWA system in the in the downstream stations of  $x/D \geq 4$ .

### 3.4.2.2 Turbulence spectra analysis

The velocity signal obtained from HWA measurements is in the time domain. The method of Fast Fourier Transform (FFT) was applied to transform the data from time domain to the frequency domain. The software MATLAB (2021) was used to perform this analysis, as described below.

The FFT of the velocity fluctuation ( $U$ ) is first calculated, resulting in half the number of unique points ( $n = L/2$ ). The total velocity points sampled ( $L$ ) over a period of time is the length of the signal, and the frequency array is half the length of the signal, where  $fps$  is the sampling rate:

$$FreqData = fft(U) \quad (3.15)$$

$$L = length(FreqData) \quad (3.16)$$

$$aFreq = fps/2 * (1:n)/n . \quad (3.17)$$

The absolute value of the frequency data squared divided by the signal length gives the power, independent of the length of the signal:

$$Power = abs(fft(U)).^2/L . \quad (3.18)$$

Plotting frequency and power shows the power spectrum (to be shown in Section 4). Then the energy  $E(f)$  can be determined by dividing power by the sampling frequency:

$$Energy = Power/fps . \quad (3.19)$$

Plotting  $E(f)$  and frequency yield the energy density spectrum, from which the inertial range is identified, and the length scales are determined (see results in Section 4.4).

### 3.4.3 Pitot tube

The pitot tube was placed at the inlet of the test section to measure the free stream velocity. A DP103-18 low pressure variable reluctance sensor (Figure 3.15) was used to catch the voltage data which can be interpreted as pressure by means of the calibration curve. The calibration of the low-pressure sensor was done using the DPI610 pressure calibrator.

## 3.5 Experimental setup

Static and dynamic tests were performed to fulfill the goals of this study. Each case uses a different cylinder model; therefore, a different setup to execute the necessary experiments was devised. In this section, the structures fabricated, and the arrangements of each test case are reported. For both cases, the streamwise stations measured were located at  $x/D = 4$  and  $x/D = 6$  downstream the model. Because a wake requires 50 to 100  $D$  to reach its self-preserving condition (Townsend, 1976), so both stations measured in this study are in the near-wake region.

For the PIV measurements, these positions were within the field of view of the camera, and they were selected during data analysis to perform the required calculations. The laser sheet of the PIV system is projected from the top of the tunnel 0.9 m away from the walls (at the middle of the test section). The seeding injector is placed vertically at the entrance of the test section, parallel to the laser sheet (See Figure 3.16 and Figure 3.17).

For the case of the HWA measurements, a bar with a moving mechanism was fabricated (Figure 3.18), which was supported vertically by two long aluminum bars attached to the floor and to the ceiling of the test section along the centerline, that is, 0.9 m away from the walls, that act as rails to move the moving mechanism bar horizontally along the x-direction. The X-

type hot wire probe was secured horizontally to the moving plate, which y-position was adjusted using a LabVIEW (2021) program. The layout of the HWA system is shown in Figure 3.19. The probe was placed at the two distances,  $x/D = 4$  and  $6$ , away from the surface of the model, and its position was varied along the y-axis. Data of the velocity field was obtained at different points, covering a total range from  $y/D = 4$  to  $y/D = -4$ .

CMOS multi-function analog laser sensors (KEYENCE IL-1000) were used to measure the displacement of the model during VIV, with which its amplitude response was obtained. One sensor was located at each side of the model under the spring plate and another at the center, with the laser beam perpendicular and aligned with the axis of the model (see Figure 3.3 and Figure 3.20). The analogue time signals of the displacement were digitally sampled with a National Instruments cDAQ-9178 (Figure 3.21).

### 3.5.1 Static setup

For the stationary experiments, an aluminum box (Figure 3.22) was designed to hold the model at both ends of the tube, outside the test section,  $1.35\text{ m}$  away from the inlet of the test section. Each box is composed of two pieces that function as a clip pressing the steel tube in between them. This holder is connected to a support bar that attaches to a frame fixed to the outer side walls of the test section (Figure 3.23). The frame is locked under the central window at the same height on both sides. The vertical support bars hold the model horizontally at the middle of the test section, perpendicular to the incoming flow, spanning through the whole width of the test section. The full layout of the PIV static test is depicted in Figure 3.16.

### 3.5.2 Aeroelastic setup

Having in mind the purpose of this study (to visualize the flow field around a two-dimensional rigid cylinder while it oscillates perpendicular to the flow), a new aeroelastic structure was designed to hold Model 2. The cylinder model was placed inside the test section,

about 1.08 m away from the inlet, and supported by two aluminum frames connected both to the floor and the ceiling of the wind tunnel, as depicted in Figure 3.24. It was connected through its longitudinal axis tube, using the aluminum boxes described in the previous subsection, to four horizontal stainless-steel plates which worked as springs (two at each end of the model) and allowed only the vertical displacement. The spring-plates were designed to match the structural stiffness based on the shedding frequency results of the static test and on the characteristics of the model. Their total stiffness was estimated as follows:

$$k = \omega^2 m = (2\pi f_s)^2 m , \quad (3.20)$$

where the expected  $f_s = 9.7 \text{ Hz}$ , and the total mass of the model  $m$  is 5.42 kg, resulting in  $k \approx 22012 \text{ N/m}$ . Hence, each spring plate should have a nominal stiffness of 5503  $\text{N/m}$ .

The dimensions of each stainless-steel plate were calculated using the equation of the maximum deflection of a bending beam (Gere & Goodno, 2012), that is,

$$\delta_{max} = \frac{WL^3}{3EI} = \frac{12WL^3}{3Ebh^3} = \frac{4WL^3}{Ebh^3} , \quad (3.21)$$

where the moment of inertia ( $I$ ) of a beam with a rectangular cross section is expressed as:

$$I = \frac{bh^3}{12} . \quad (3.22)$$

Here  $b$  represents the width of the spring plate and  $h$  the height (or thickness). The deflection can be expressed in terms of weight and stiffness

$$\delta = \frac{W}{k} , \quad (3.23)$$

and the length of the spring plate can be estimated in terms of the total stiffness as

$$L = \sqrt[3]{\frac{Ebh^3}{4k}} . \quad (3.24)$$

The height (thickness) was first selected, in accordance with the material available for manufacturing, to be 0.0025  $m$ . After comparing different possible lengths, the most apt for

our needs of the flow field visualization was chosen. A plate-springs was fabricated with length = 0.344 m, width = 0.04 m and thickness = 0.0025 m.

To have a rough idea of the oscillation response of the aeroelastic structure, the non-dimensional amplitude expected in this study is calculated using Equation 2.15. With the relatively high damping of the structure ( $\zeta = 0.005$ ), which leads to a relatively high Scruton number ( $Sc = 7.12$ ), the maximum amplitude predicted is  $A_{max}^* \approx 0.2$ .

### 3.6 Uncertainty and error analysis

Experimental measurements are not and will never be perfect. Every real measurement is subject to a finite measurement error and uncertainties of the calculation procedure. The measured values can be decomposed into a true value and the measurement error  $\delta_X$  (Raffel et al., 2018):

$$X_{measured} = X_{true} + \delta_X . \quad (3.25)$$

#### 3.6.1 HWA errors

The data obtained using the X-type HWA has an uncertainty which derivates from the accuracy of the instrument and the sensors, the resolution of the A/D converter, and the conversion error of voltage to velocity during calibration. The total error  $U_{total}$  of the HWA system is estimated as (Bevington et al., 1993):

$$U_{total} = \sqrt{U_{DPI610}^2 + U_{pitot}^2 + U_{probe}^2 + U_{AD}^2 + U_{poly}^2} . \quad (3.26)$$

The estimation of the maximum error ( $U_{DPI610}$ ) of the pressure calibrator DPI610 is 0.05%, obtained from the pressure calibrator itself, which matches that shown in the manual ("Druck DPI 610/615 IS: User manual K0430," 2008); estimation of the pitot tube error ( $U_{pitot}$ ) is 1%; the precision error for the X-type HWA sensor probe (55P61) was considered to be  $U_{probe} \approx 2\%$ , according to Dantec Dynamic's manual (Jorgensen, 2002); the estimation of the voltage

resolution of the A/D converter ( $U_{AD}$ ) is 0.02% (Jorgensen, 2002); and the linearization error of the quadratic polynomial calibration curve ( $U_{poly}$ ) is deemed to be  $\approx 1\%$  (Jorgensen, 2002).

Taking into consideration the free stream velocity used in this study, the total uncertainty of the HWA system employed is estimated to be about 2.4%. Details of values of the HWA experimental errors, as well as their sources are shown in Table 3-1.

### 3.6.2 PIV errors

Errors in PIV measurements might be due to the specific flow facility used, setup of experimental apparatus, image recording process and choices of the data evaluation methods. There exist two types of errors: random errors which are usually non predictable and can change in magnitude and sign for each single measurement; and systematic (or bias) errors caused by incorrect calibration or incorrect operation of the measurement system, typically constant and predictable.

The installation and alignment of the apparatus is of critical importance so to reduce perspective errors. The calibration procedure may contribute an error if the measurement laser sheet plane does not perfectly coincide with the plane selected for the calibration, leading to a variation of the optical magnification along the direction of the optical axis. If the calibration is conducted properly, the magnification and calibration uncertainties can be neglected with respect to the total uncertainty (Sciacchitano, 2019), however, this is a hard task, so this type of error is considered.

In this study, the uncertainty of the PIV measurement was estimated by separately estimating the uncertainty due to systematic errors and random errors. Systematic errors include truncation errors due to the finite number of particle images in an interrogation window, estimated to approach 1 pixel, and detection error in magnification process, estimated to be 0.1 pixel:

$$\text{Systematic error} = \sqrt{1^2 + 0.1^2} \approx 1.005 . \quad (3.27)$$

Random error sources include particle image diameter, particle image density, background noise, particle image shift, and displacement gradients, obtained based on the results found by Raffel et al. (2018):

$$\text{Random error} = \sqrt{0.003^2 + 0.004^2 + 0.042^2 + 0.003^2 + 0.003^2} \approx 0.0425. \quad (3.28)$$

Thus, the overall error in pixels is  $\sqrt{1.005 + 0.0425} = 1.0059$  (individual errors and sources are summarized in Table 3-2). So, for an image resolution of  $1024 \times 1024$  pixels, the uncertainty of the PIV measurement is about 3.13%, calculated as follows:

$$\text{Total uncertainty} = \sqrt{\frac{1.0059}{1024}} = 0.0313 \cong 3.1\% . \quad (3.29)$$



Table 3-1 Error sources and uncertainty of HWA system. Note: the free stream velocity considered is 5 m/s.

<b>Source</b>	<b>Error (%)</b>	<b>Error (m/s)</b>
Pressure calibrator	0.05	0.0025
Pitot tube calibration	1	0.05
HWA sensor probe (55P61)	2	0.1
A/D converter resolution	0.02	0.001
Polynomial calibration curve	1	0.05
<b>Overall error (m/s)</b>		<b>0.1225</b>
<b>Relative uncertainty (%)</b>		<b>2.4%</b>

Table 3-2 Error sources and uncertainty of PIV system. Note: these values correspond to an interrogation window size of  $32 \times 32$ .

<b>Source</b>	<b>Error value (pixels)</b>
Particle image diameter	0.003
Particle image density	0.004
Background noise	0.042
Particle image shift	0.003
Displacement gradients	0.003
Truncation error due to finite number of particles in an interrogation window size	1
Error due to magnification and calibration	0.1
<b>Overall error</b>	<b>1.0059</b>
<b>Relative uncertainty (%)</b>	<b>3.1%</b>

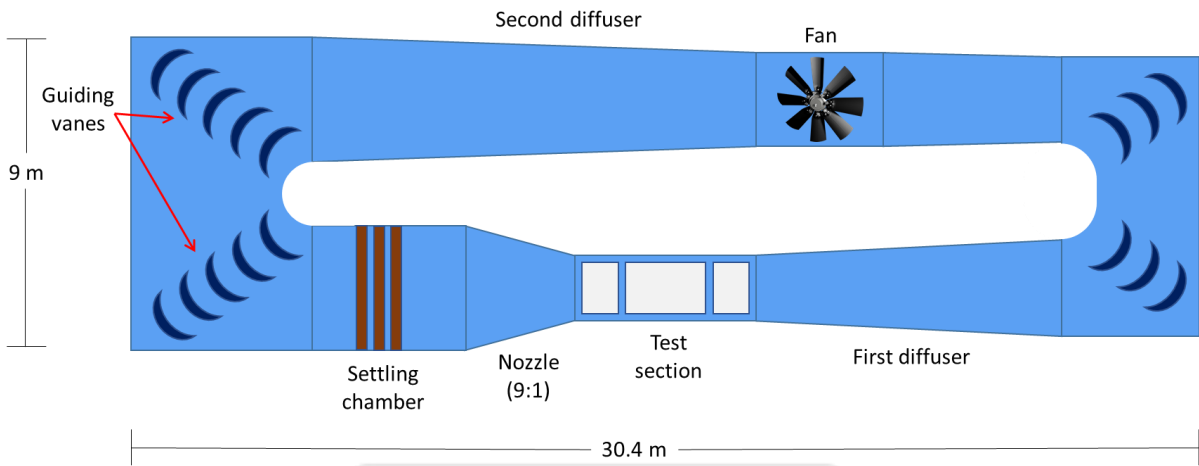


Figure 3.1. Diagram of the low-speed wind tunnel used in this research.

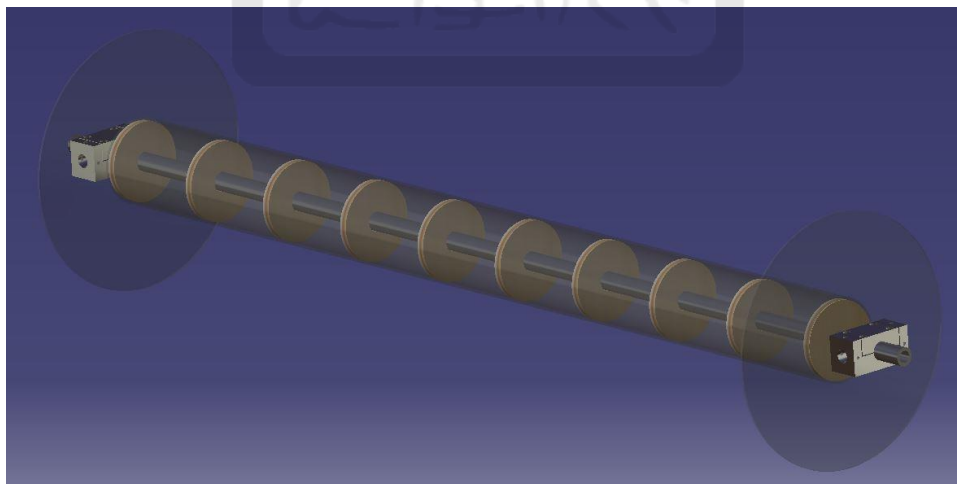


Figure 3.2. Design of circular cylinder model for vibrating tests.



Figure 3.3. Cylinder (Model 2) used for vibrating tests installed in the low-speed wind tunnel. Three laser sensors were used to measure the amplitude of vibration.



Figure 3.4. Green laser DPSS 532 nm – 5W.



Figure 3.5. High speed camera Photron Fastcam SA-X.



Figure 3.6. Custom made mirror for PIV laser.



Figure 3.7. Camera lens Nikon NIKKOR 50 mm f/1.2.



Figure 3.8. Seeding injector.

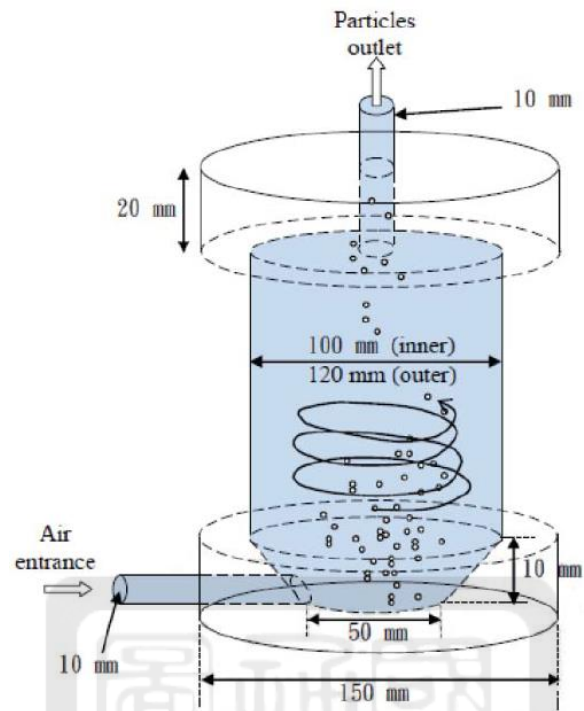


Figure 3.9. Design of the particle seeding device.



Figure 3.10. DANTEC Streamline Pro CTA 90C10 system.



Figure 3.11. NI BNC-210 terminal block.

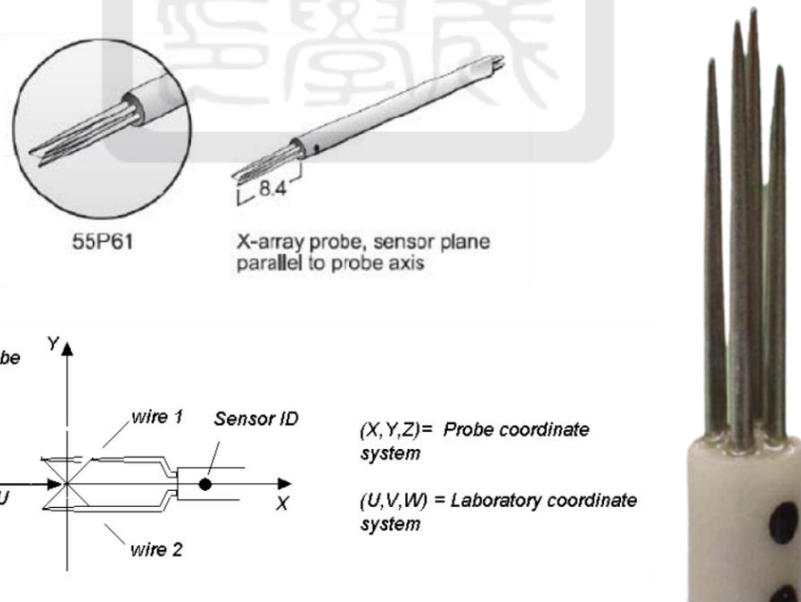


Figure 3.12. X-wire probe 55P61 and its orientation with respect to experimental coordinate system



Figure 3.13. Low pressure calibrator DPI610.

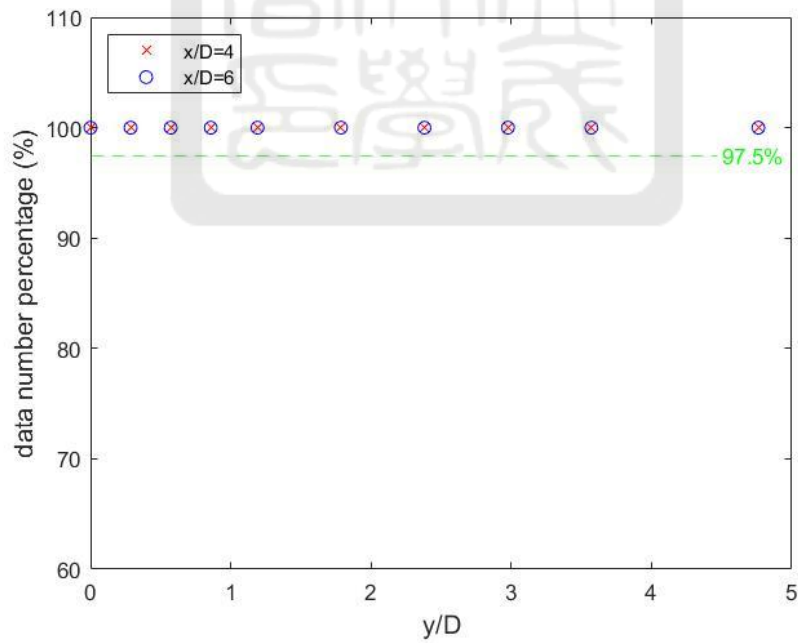


Figure 3.14. Percentage of raw data that satisfy the condition  $|\beta| \leq 45^\circ$  at streamwise stations of  $x/D = 4$  and  $6$  for the case of  $Re = 1.3 \times 10^4$ .



Figure 3.15. Validyne DP103-18 low pressure variable reluctance sensor.

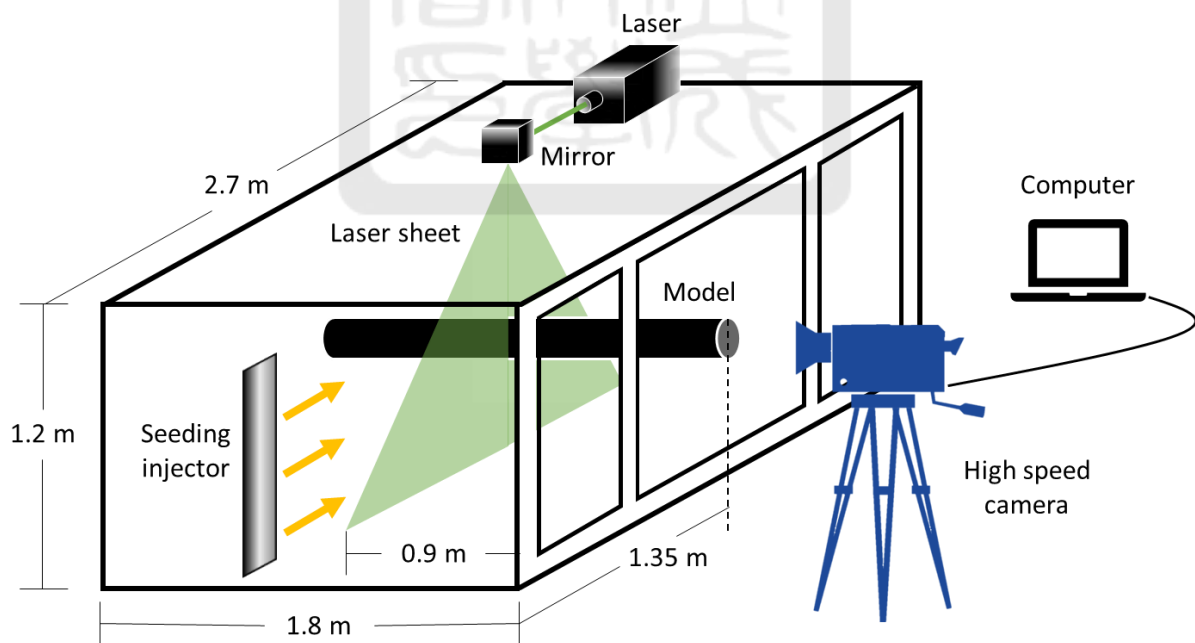


Figure 3.16. Experimental layout of the PIV static test.

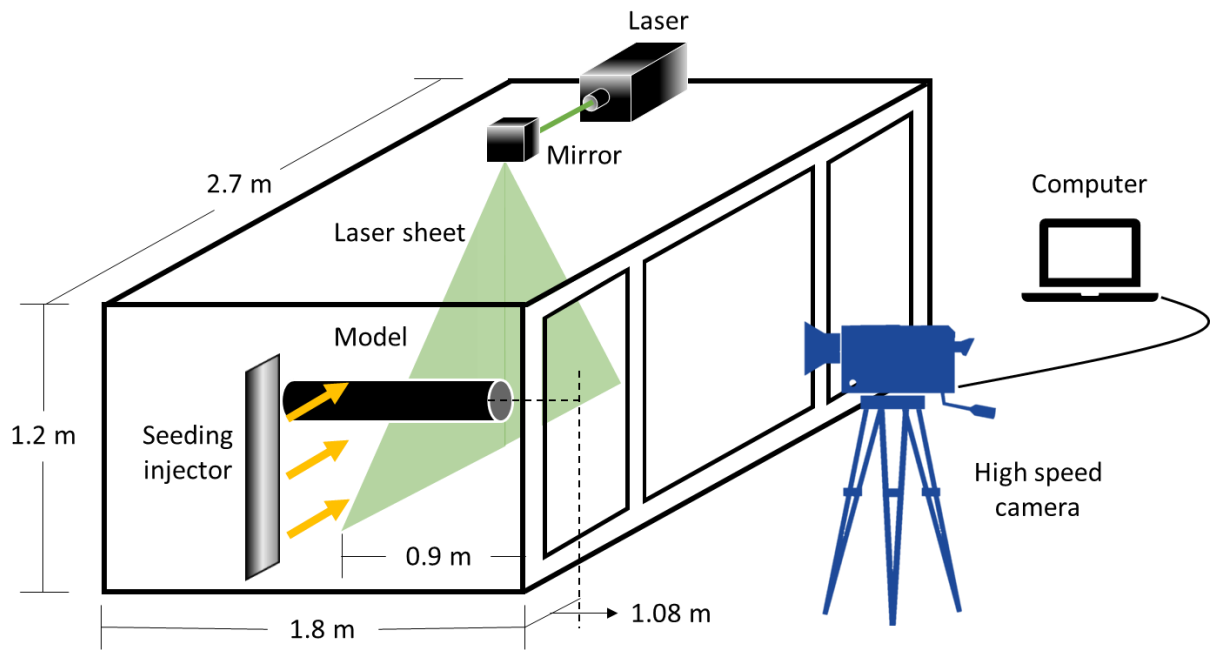


Figure 3.17. Experimental layout of the PIV vibrating test.

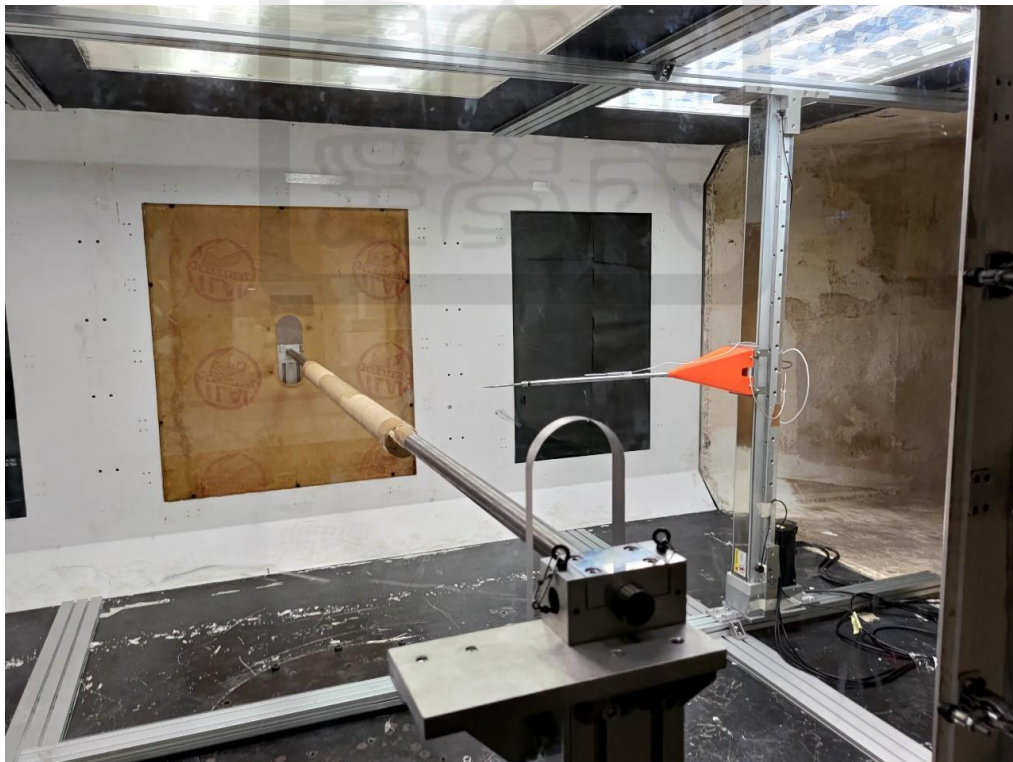


Figure 3.18. The HWA static test setup. It shows the circular cylinder model and the structure supporting the HWA probe. The vertical bar has a moving mechanism that can move the plate supporting the HWA in the  $y$  direction.

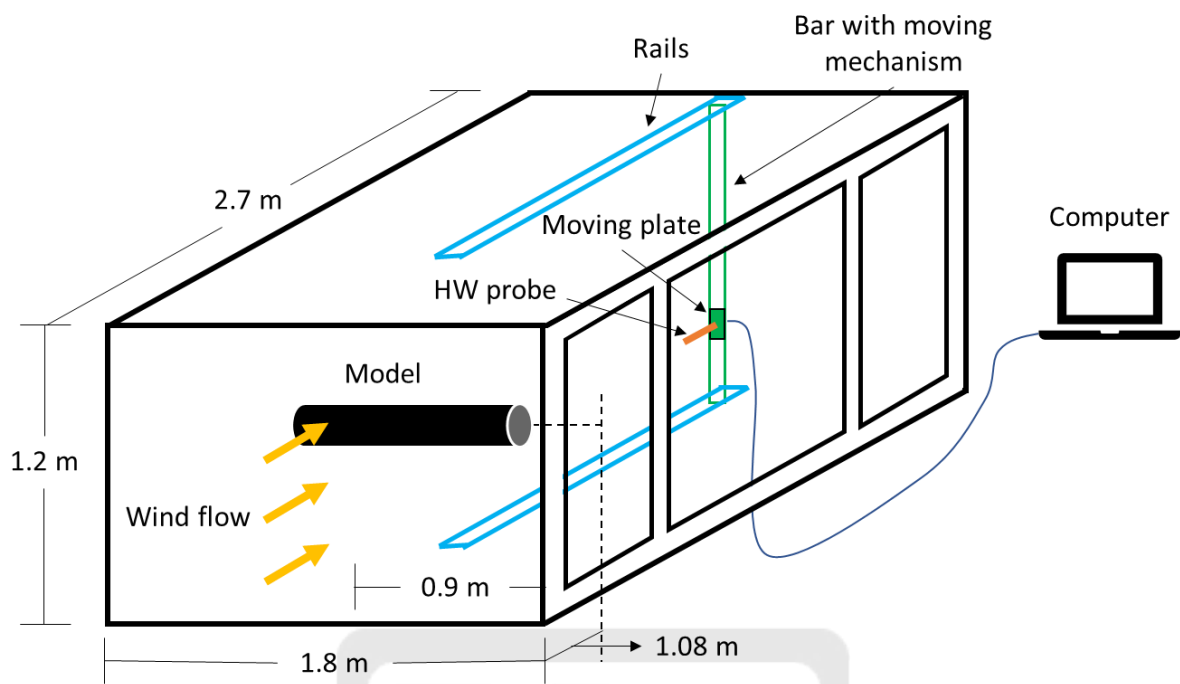


Figure 3.19. Experimental layout of HWA test (for aeroelastic test).



Figure 3.20. The laser sensors KEYENCE IL-1000.



Figure 3.21. The NI cDAQ-9178.



Figure 3.22. Aluminum box holder mounted at the ends of both models.



Figure 3.23. Structure that supports the model for the static experiments.

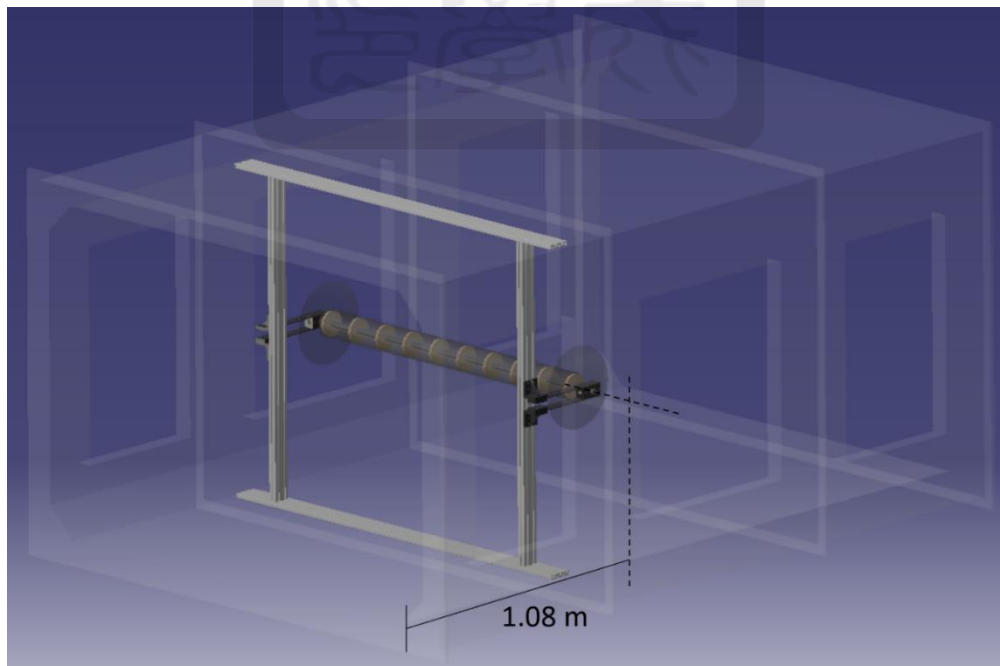


Figure 3.24. Design of aeroelastic support structure

## Chapter 4 – Experimental results and discussion

### 4.1 Fixed test

Fixed tests were done using a circular cylinder and employing PIV and HWA measuring techniques. PIV is used to measure the two-dimensional instantaneous velocity distributions and to visualize the flow field behavior, as well as the vorticity field. The flow field results obtained with the HWA provide a basis to corroborate the accuracy of the PIV system employed. The results of each measurement technique and a comparison between them are discussed in this subsection.

#### 4.1.1 Selection of seeding material

First, PIV tests were carried out using two different seeding particle materials to compare their results with those of HWA in order to select the tracer particles that best follow the motion of the flow. One was oil DEHS (Di-Ethyl-Hexyl-Sebacat) with an average particle size of  $3\ \mu\text{m}$ , for which a high-volume liquid seeding generator was utilized; while the other was aluminum oxide ( $\text{Al}_2\text{O}_3$ ) solid particles, as described in Section 3.4.1.1. Even though the Stokes number of both seeding materials ( $Stk = 0.001$  and  $0.142$  for DEHS and  $\text{Al}_2\text{O}_3$ , respectively) satisfy the criteria of  $Stk \ll 1$ , implying that particles can be treated as point sources in the turbulent flow and maintain near dynamic equilibrium with the carrier fluid, as stated by Crowe et al. (1996), they exhibit different results due to the limitation of the PIV system used in this investigation. Due to the large size of the wind tunnel test section, the high-speed camera is placed at a great distance afar from the laser sheet. Therefore, the sizes of the particles projected on the image frames is remarkably reduced, which lead to their brightness being diminished. This, in turns, causes more inaccuracy during the data analysis.

The mean streamwise velocity results of both PIV measurements (using DEHS and  $\text{Al}_2\text{O}_3$ ) are compared with the results of HWA, for  $Re \cong 13000$  and  $Re \cong 24000$ , in Figure

4.1 and Figure 4.2, respectively. It is clearly seen that the velocity profiles using DEHS as seeding material differ from those of the solid particles and the HWA. Red dots denote the positions at which errors between PIV and HWA measurements are greater than 10%, as calculated with Eq. (4.1). For a better appreciation of the discrepancy between the different cases, the maximum error in each of the three measured sections ( $x/D = 2, 4$  and  $6$ ) between the HWA and the PIV using oil and solid particles, for the two cases exhibited in Figure 4.1 and Figure 4.2 have been calculated as below and are summarized in Table 4-1.

$$Error (\%) = \frac{u_{PIV} - u_{HWA}}{u_{HWA}} \times 100\% . \quad (4.1)$$

At the station of  $x/D = 2$ , the error is largest for the two cases. Additionally, the errors using oil particles are larger than those using solid particles. Therefore, solid  $Al_2O_3$  were chosen to perform all subsequent PIV experiments.

#### 4.1.2 Verification of analysis techniques

In order to validate the reliability of the velocity field and turbulence characteristics measured by using the PIV, the mean velocity profiles and turbulence intensity profiles were compared with those measured with the HWA at three different streamwise stations:  $x/D = 2, 4$  and  $6$ , which are located within the near-wake region.

Because the flow pattern is the main interest of this study, the first order statistics are of particular importance. Thus, the present results of the mean streamwise and lateral velocity profiles at  $Re \cong 1.3 \times 10^4$  were also compared with the results of Lin (2021) to further verify the accuracy of the present measurements, as shown in Figure 4.3 and Figure 4.4. Lin used a X-type HWA to measure the flow field behind a circular cylinder at  $Re \cong 1.2 \times 10^4$ , with  $St = 0.21$ . Unconfident mean measurements obtained between either PIV and HWA, or in the present work and the Lin's measurements, are highlighted in red (with  $error > 10\%$ ). Lin's results and the HWA results of the present study are mostly consistent with each other; with

differences of mean streamwise components (for HWA measurements at  $x/D = 4$  and  $6$ ) smaller than 7.8%.

The root-mean-square (rms) fluctuating velocities of streamwise and lateral components obtained with PIV and HWA for  $Re \cong 1.3 \times 10^4$  are shown in Figure 4.5 and Figure 4.6, respectively. Likewise, comparisons of the present PIV and HWA results of mean lateral velocities and rms velocities of streamwise and lateral components for the case of  $Re = 2.4 \times 10^4$  at the three selected stations are presented in Figure 4.7 - Figure 4.9 (mean streamwise results can be seen in Figure 4.2). At  $x/D = 2$  mean velocity results differ greatly, as depicted with red dots (with *error* > 10%). However, at  $Re \cong 1.3 \times 10^4$  the maximum difference between HWA and PIV streamwise velocity profiles is 8.1%, while for  $Re \cong 2.4 \times 10^4$  the differences are smaller than 1.8%. Note that scales (x-axis range) of streamwise and lateral results are not the same; they have been adjusted for a better visualization. Similar results were obtained by Chen and Chang (2018) for cases with lower Reynolds numbers ( $Re = 3856$  and  $9959$ ), and at slightly more upstream stations ( $x/D = 1.8$  and  $1.59$ ) who compared PIV and HWA data with LES predictions.

Thus, a conclusion can be drawn that at core subregions of very upstream stations ( $x/D \leq 2$ ), where the intensity of fluctuating velocity is high and remarkable variations of instantaneous flow angles frequently occur, no reliable measurements can be made using either PIV or HWA system and are, hence, discarded in this study. Nonetheless, both techniques can perform confident measurements in the downstream stations of  $x/D > 2$ . In other words, data measured with either PIV or HWA system at stations of  $x/D > 2$  can be considered reliable. Accordingly, for this study, in which  $Al_2O_3$  particles are employed, and results are obtained at stations  $x/D = 4$  and  $6$ , the maximum streamwise velocity error between PIV and HWA techniques is about 8.1%, which happens at the case of  $Re \cong 1.3 \times 10^4$ , as shown in Table 4-1.

### 4.1.3 PIV results

#### 4.1.3.1 Standard deviation

To investigate the accuracy of the data obtained from PIV experiments, the standard deviation, as well as the standard error, were calculated. For a large number of data, the uncertainty in the mean is given by the standard deviation (std)  $\sigma$ :

$$\sigma = \sqrt{\frac{1}{N} \sum_{i=1}^N |x_i - \bar{x}|^2} \quad (4.2)$$

which is a common measure of the random error of a large number of observations. The parameter  $x_i$  and  $\bar{x}$  denote the  $i^{th}$  individual measurement and the corresponding mean values, respectively (Raffel et al., 2018). Additionally, the standard error (SE) is used to report the average value of  $N$  measurements associated with the standard deviation of the mean:

$$\sigma_{\bar{x}} = \frac{\sigma}{\sqrt{N}} \quad (4.3)$$

By looking at this equation, one can observe that the standard error is smaller than the standard deviation by a factor of  $1/\sqrt{N}$ . This reflects the fact that the uncertainty of the average value gets smaller when using a larger number of samples. The SE obtained in this study agrees with this definition; the standard error decreases as the number of samples increase (see Figure 4.10).

To guarantee that the data analysis yields invariant results, the standard deviation and the standard error of the mean velocity were calculated with increasing number of samples at different points in the flow field, illustrated in Figure 4.10, showing the variations of std and SE versus the number of sample at  $x/D = 4$ ,  $y/D = 1$  for  $Re = 1.3 \times 10^4$  and  $2.4 \times 10^4$ . Specific std and SE results of the mean streamwise velocity are summarized in Table 4-2. The order of magnitude of the standard errors is  $-4$ , which is close to the values obtained by Seyed-Aghazadeh et al. (2017). Furthermore, the maximum error in the mean velocity is about 0.55%, which is much smaller than that reported by Hsieh et al. (2017). Additionally, Figure 4.11

shows the std against the number of samples at two different points ( $x/D = 4$ ,  $y/D = 1$ ) and (4, 3), for both cases of  $Re = 1.3 \times 10^4$  and  $2.4 \times 10^4$ . It can be seen that the std becomes invariant at about  $N > 15000$  (for  $Re = 1.3 \times 10^4$ ) and 20000 (for  $Re = 2.4 \times 10^4$ ), as delineated with red dashed lines. In other words, the minimum number of samples needed to obtain invariant results are about 15000 and 20000 for  $Re = 1.3 \times 10^4$  and  $2.4 \times 10^4$ , respectively. Thus, for a higher Reynolds number, the number of samples necessary to obtain an invariant result must be increased. On that account, by using 24000 and 43000 samples (for static and vibrating tests, respectively) to analyze the flow field characteristics, the results obtained in this study are statistically stationary and within the tolerated error, indicating that PIV measurements are reliable.

#### 4.1.3.2 Characteristics of the mean and fluctuating velocity fields

This section examines the mean velocity fields and turbulence measured by PIV to obtain a better insight into the wake characteristics of vortex shedding over a stationary cylinder. Figure 4.12 compares the mean velocity vectors contours, whose magnitude is  $\sqrt{\bar{u}^2 + \bar{v}^2}$ , between the two values of  $Re$ . For better clarity, their corresponding profiles normalized with  $U_f$  are plotted for two different stations ( $x/D = 4$  and 6), indicated with blue dashed lines. This demonstrates that the values of  $\bar{u}$  near the x-axis are smaller than those away from the axis.

According to Hsieh et al. (2017), a recirculation zone appears downstream of the model, wherein vortices are formed, indicating a negative velocity magnitude. Figure 4.12 a) shows smaller values at the axis (illustrated by a blue contour) than those in Figure 4.12 b) (with a minimum value of 0.1). This is due to the fact that at higher velocities the recirculation zone becomes shorter (Hsieh et al., 2017). This can be appreciated by turning into the green area (in the very near-wake subregion) of the contours, so the mean velocity at the same station is higher. Moreover, the mean streamwise velocity profiles farther away from the model ( $x/D = 6$ )

become flatter than those near the model. This is further corroborated in Figure 4.13, which shows the mean and rms fluctuating velocity profiles at different stations for both cases of Reynolds number. Figure 4.13 shows that the  $\bar{v}$  distribution for the stationary case exhibit an S-shape downstream of the cylinder. This indicates that the flow is either directed upwards or downwards on either side of the x-axis. This vertical motion gradually diminishes as the vortex moves further downstream. So, in these results, at station 7D the vertical motion is the weakest.

## 4.2 Vibrating test

Similar to the fixed tests performed, vibrating tests were carried out using PIV and HWA techniques. The results of the vibrating tests, namely the amplitude and frequency response, and the wake flow characteristics such as velocity and vorticity fields are discussed in the following lines.

First, a series of free decay experiments were conducted in still air in order to obtain the damping ratio and the natural frequency of the structure. The cylinder was excited to oscillate freely by applying an initial displacement. The free decay curve is illustrated in Figure 4.14 a). Its frequency spectrum calculated by Fast Fourier Transform (FFT) using the free decay experimental displacement data is presented in Figure 4.14 b), showing the value of the natural frequency to be  $f_n = 9.7 \text{ Hz}$ . To calculate the damping ratio  $\zeta$ , first the amplitude decay time history was obtained, and a few peaks were identified (time, amplitude), namely peak 0, peak 1 and peak n (see Figure 4.15), where  $(t_0, A_0) = (0.08, 0.032)$  ;  $(t_1, A_1) = (0.185, 0.0316)$  ; and  $(t_n, A_n) = (0.39, 0.029)$ . The damping can then be estimated as follows:

$$\zeta = \frac{\delta}{\sqrt{4\pi^2 + \delta^2}} \quad (4.4)$$

where  $\delta$  is the logarithmic decrement defined as:

$$\delta = \frac{1}{n} \ln \left( \frac{A_0}{A_n} \right). \quad (4.5)$$

Here,  $n$  is the period number, which can be obtained knowing the period of oscillation  $T$  (the time between two peaks), as follows:

$$T_n = t_1 - t_0, \quad (4.6)$$

$$n = \frac{t_n - t_0}{T}. \quad (4.7)$$

After calculations, the damping of the aeroelastic system used in this study was found to be  $\zeta = 0.005$ .

### 4.2.1 Frequency response

From HWA and oscillation amplitude experiments, the frequency responses for the different cases were calculated. The phenomenon of lock-in (or synchronization) means that the ratio  $f^* = f_s/f_n \approx 1$ , that is, the matching of the periodic wake vortex mode with the natural frequency of the body (Williamson & Govardhan, 2004). Figure 4.16 - Figure 4.19 show the time histories and their corresponding spectra of the cylinder vibration amplitude and velocity fluctuations at station  $x/D = 4$ . Figure 4.16 corresponds to a lock-in state at a reduced velocity of  $U^* = 5.3$ . At this state, only one frequency peak can be observed, meaning that the vortex shedding frequency of the system resonates with its natural frequency. On the contrary, Figure 4.17 - Figure 4.19 each corresponds to a non-lock-in state, including pre-lock-in reduced velocities  $U^* = 3.3$  and  $4.6$  (Figure 4.17 and Figure 4.18, respectively), and after lock-in reduced velocity (when the system has passed outside the lock-in range)  $U^* = 6$  (Figure 4.19).

For the non-lock-in state, the spectrum of the cylinder vibration (amplitude fluctuation) shows components at both frequencies  $f_s$  and  $f_n$ , while the velocity fluctuation spectrum contains only the vortex shedding frequency  $f_s$ . For instance, for the case of  $U^* = 4.6$ , the spectrum of the velocity fluctuation yields  $f_s = 8 \text{ Hz}$ , while the spectrum of the vibration amplitude displays two peaks, the first being  $8 \text{ Hz}$  ( $= f_s$ ), and the second showing a value of

$f_n = 9.7 \text{ Hz}$ . In a like manner, the results for station  $x/D = 6$  exhibit a similar response. The respective results for both cases are summarized in Table 4-3. These results agree with Bearman (1984), who stated that for large mass ratios ( $m^* \gg 1$ ), the actual cylinder oscillation frequency ( $f$ ) at resonance will be close to both the vortex shedding frequency for the static cylinder and the system natural frequency, that is  $f \approx f_s \approx f_n$ . Also, they are in good agreement with the definitions of lock-in or synchronization state discussed in Section 2.4.2, and with those obtained by Goswami et al. (Goswami et al., 1993) too.

### 4.2.2 Amplitude response

The amplitude response of the freely vibrating circular cylinder was measured at different wind speeds ranging between  $U^* = 4 \sim 6$ . The time histories of the amplitude response obtained from vibrating tests are shown in Figure 4.16 - Figure 4.19 and the maximum amplitude in each response plot  $A_{max}^*$  is detected (similar to Govardhan and Williamson (2006)).

Figure 4.20 shows the maximum amplitude results of the vibrating tests as a function of the velocity ratio  $U^*$ . In this study, three different branches were detected, namely the initial, the upper, and the lower branches (displayed in red in Figure 4.20 (b)). A plot from Williamson and Govardhan (2004) was used as a benchmark for comparison (shown in Figure 4.20 (a)), in which the dark squares are the data obtained from water tunnel tests with a low mass ratio ( $m^* = 2.4$ ); the white diamonds are the data obtained by Feng (1968) from wind tunnel experiments with a higher mass ratio ( $m^* \approx 250$ ), which is about 53% of the mass ratio value in this study ( $m^* = 469$ ). The present results show the initial branch being close to  $U^* = 4$ , akin to the wind tunnel case (Feng, 1968). However, the range of  $U^*$  over which there is significant response is 1.5 times larger than that found in the present study. Also, the maximum amplitudes ( $A_{max}^*$ ) found in this study (Figure 4.20 b)) are about one order of magnitude smaller than those of Feng (1968). Note that the axis scales in Figure 4.20 have been adjusted

for a clearer visualization. This reveals that the lock-in range (or synchronization regime) widens, and the maximum amplitude increases significantly as the  $m^*$  decreases, similar to the observations of Williamson and Govardhan (2004). Therefore, present results reveal that the amplitude response of a system with high  $m^*$  in an air flow is delayed, compared to a low  $m^*$ , but still exhibit the three different amplitude branches.

From previous calculations (see Section 3.3), the predicted resonance velocity (the velocity at which the vortex shedding frequency matches the natural frequency of the structure) is about  $5.2 \text{ m/s}$  ( $U^* = 5.3$ ). At resonance, the elastically mounted cylinder is expected to present the maximum oscillations. The  $A_{max}^*$  captured during vibrating tests is about 0.04, lower than the expected from Equation (2.15). As explained by Belloli et al. (2015), the difference between the theoretically calculated amplitude and the actual experimental amplitude can be partially justified by the non-linear dependence of damping on oscillation amplitude. It was also found that the maximum oscillation amplitude occurs at the resonance velocity  $U^* = 5.3$ . This validates the previously discussed synchronization frequency concepts. That is, at resonance, when  $f \approx f_s \approx f_n$ , the amplitude of vibration reaches its maximum. This is further confirmed by the cylinder vibration time history at the resonance velocity (see Figure 4.16), which displays the largest amplitude of the four different velocities examined.

### 4.3 Strouhal number data

This section reviews the trends found between the Strouhal number and the Reynolds number in literature and discusses the main difference between the rigid and the elastic setup. The Strouhal number ( $St$ ) is defined as a function of the vortex shedding frequency, cylinder diameter and velocity of ambient flow. The Reynolds number range examined in this study extends from approximately  $2 \times 10^4$  to  $4 \times 10^4$ , within the subcritical regime. The results from this set of experiments are shown in Figure 4.21 and are compared with the experimental

data of static and elastically mounted cylinders (with one degree of freedom) collected from literature.

Fixed test results correlate better with Mulcahy (1984) results (yellow triangles) than with Lienhard's (1966) curve (blue line). In Table 4-4 it can be seen that, for  $U^* = 3.3$  ( $Re = 2 \times 10^4$ ), the  $St = 0.24$ , and gradually decreases as the wind flow velocity increases. On the other hand, Strouhal number results for the vibrating case fall mostly within the envelope of Lienhard (1966), which are in good agreement with the experimental data of cylinders with one degree of freedom obtained by Resvanis et al. (2012), too, as illustrated in Figure 4.21. In this case,  $St = 0.128$  for a velocity ratio of  $U^* = 3.3$  ( $Re = 2 \times 10^4$ ), and, unlike the static case, the Strouhal number increases as the velocity is increased. This reveals that there is an apparent trend in variation of Strouhal numbers as flow velocity changes for a cylinder subject to VIV. For instance, results of static case exhibit a Strouhal number with values of  $St > 0.2$ , while vibrating case show results with  $St < 0.2$ .

It is important to keep in mind that the conventional  $St$  versus  $Re$  relationship shown in Figure 4.21 is applicable to flows passing fixed circular cylinders, for which the lock-in phenomena and synchronizations of eddies shed from the cylinder with the structural frequencies do not exist. Nevertheless, results of Strouhal number are affected by different parameters, for instance, the surface roughness, turbulent intensity, and blockage ratio. Additionally, the same Strouhal number behavior is not prevalent in vibrating cylinders where vortices are synchronized in the wake. Accounting for this consideration, the results obtained in this study are considered satisfactory.

#### **4.4 Inertial subrange and Taylor subrange length scales**

Large eddies appear in the flow after passing the cylinder, in which energy is fed by the mean flow itself. The eddies cascade down to smaller eddies until they reach the Kolmogorov length scale, which is the smallest eddy size, and are damped out by fluid viscosity. In this

fashion, the spectrum of spatial or temporal eddy sizes reaches a fully-developed state in which the disturbance energy of any eddy size becomes relatively constant. Hence, it is important to know the length scales on the flow in order to determine whether the flow has reached the fully developed state, or it is still cascading down. In this section, the results for the length scales and the inertial subrange are presented and discussed. For both cases (static and vibrating) the energy density spectrum was obtained at point  $(x/D, y/D) = (4,1)$ , while length scales were calculated at two points:  $(x/D, y/D) = (4,1)$  and  $(6,1)$ , from HWA experiments.

The energy density was obtained from FFT analysis and is used to determine the inertial range by means of the Kolmogorov's  $-5/3$  power law (Lewandowski & Pinier, 2016), which states that at this range the energy density of the flow behaves like  $C^{te} k^{-5/3}$ . The moving average of the data was calculated to filter out the noise in the spectrum and smooth the distribution curve, as a means of simplifying the detection of the inertial range. To select the size of the moving average, the sum of absolute differences (*SAD*) was determined for different window sizes. *SAD* is the difference between the real signal and the smoothed signal, that is,

$$SAD = \sum |smoothed E(f) - real E(f)| \quad (4.8)$$

A plot of *SAD* against window size is shown in Figure 4.22. It shows that as the window size increases, the difference between the real signal and the smoothed signal begins to flat out (in other words, reaching the asymptotic value). With this in mind, the size of the moving average size, for each case, was defined as the value for which the *SAD* is greater than 90% of the asymptotic value.

Figure 4.23 illustrates the actual and the smoothed energy density spectra (plotted using a log-log scale), for each velocity ratio  $U^*$ , of the static and vibrating case, respectively. Their respective inertial subranges are highlighted with red line. Its approximate limits,  $k_1$  and  $k_2$  (see Figure 2.8 for reference), are shown in Table 4-5. The upper limits of the static case are higher than those of the vibrating case, implying that eddies dissipate at higher frequencies.

The integral length scale,  $\Lambda_x$ , and the Taylor length scale,  $\lambda_x$ , were calculated by means of the energy density spectra  $E(f)$  using Equation (2.24) and Equation (2.25), respectively. Table 4-6 shows  $\Lambda_x$  and  $\lambda_x$  of each case tested (in  $\mu m$ ), at two different stations:  $x/D = 4$  and  $x/D = 6$ . The integral length scale is the size of the largest eddy. For the static case, at both stations,  $\Lambda_x$  is roughly  $O(10^{-2} m)$ , which is almost equal to 1/10 of the diameter of the circular cylinder, similar to the results of El-Gabry et al. (2014). Nonetheless, it is evident that, from station  $x/D = 4$  to  $x/D = 6$ , the size of  $\Lambda_x$  increases slightly, meaning that the eddy size is still growing and has not reached its largest size. The vibrating case present the same trend with regards to the length scale at different station, that is,  $\Lambda_x$ s are larger at station  $x/D = 6$ . Furthermore, the size of  $\Lambda_x$  becomes larger when the cylinder vibrates. The integral and Taylor length scales for the vibrating case are usually larger than those of the static case by a factor,

$$LS = \frac{\text{Length scale of vibrating case}}{\text{Length scale of static case}}, \quad (4.9)$$

which decreases as the velocity increases. This is shown in Figure 4.24, where the  $LS$  factor of both length scales ( $\Lambda_x$  and  $\lambda_x$ ) at  $x/D = 4$  and 6 are plotted. As the velocity is increased, the Integral length scale difference between the static and vibrating cylinder becomes smaller. Thus, the integral length scale is commensurate to the vibration amplitude of the cylinder.

The Taylor length scale,  $\lambda_x$ , is approximately one order of magnitude smaller than  $\Lambda_x$ . No matter what the wind speed is,  $\lambda_x$ 's at both stations present comparable sizes. Furthermore, the Taylor length scale difference between the static and vibrating cases is almost imperceptible, with the  $LS$  factor being smaller than 1.2. Hence, the Taylor length scale is not apparently increased nor decreased with the downstream distance or flow speed, whether the cylinder is vibrating or static. These results suggest that the Taylor length scale is independent of structural vibrations.

## 4.5 Vortex visualization in the wake

In this section, the vortical structures and characteristics of vortex shedding based on the PIV data of Model 2, for both static and vibrating cases, are discussed. To elucidate this mechanism, the vorticity contours and their respective vortex strength are presented.

As learning from literature, it is clear that detecting an eddy structure (vortex) is not an easy task. There exist many different definitions of a vortex (Carlier & Stanislas 2005; Jeong & Hussain, 1995). It is thus difficult to select a reliable quantitative criterion corresponding to a certain definition. Because there exists significant vorticity in a shear layer, the vorticity alone is not enough to detect a vortex. This complicates the differentiation between a vortex and a local shear layer. This means that, as Jeong and Hussain (1995) concluded, “the instantaneous vorticity fields are inadequate to reveal coherent structures in turbulent boundary layers”. To deal with this problem, the vortices are identified by the  $Q$  criterion method discussed earlier (Section 2.2.1) in this study. It provides a measure of the swirl strength to allow us to determine whether the vortices are induced mainly by the flow rotation or by the strain rate effects. The values of  $Q > 0$  indicate that at that position the effects of the region’s rotation are stronger than the strain rate effects.

Moreover, to obtain a clearer and more detailed visualization of the flow structures in the wake, the phase averaging technique was applied. Because the vortex shedding is a quasi-periodic phenomenon, the instantaneous velocity fields can be phase-averaged with respect to each period of the vortex shedding cycle. To do so, the number of samples in one period ( $N_p$ ) is first determined by dividing the shedding period of vortices  $T$  over the sampling period as  $N_p = T/T_{samp}$ . Knowing how many data samples are needed to complete one full period, the instantaneous data with interval  $N_p$  can be gathered and averaged together. Furthermore, the total number of periods within the experimental data ( $N$ ) can be calculated as  $T_{N_p} = N/N_p$ . These two values ( $N_p$  and  $T_{N_p}$ ), as well as the first zero-up-cross value (to be defined later),

are important to determine the phases within a shedding period, thus they are shown in Table 4-7.

Thereupon, the phase within a vortex shedding period is defined as

$$Phase = t_p/T \quad (4.10)$$

where  $T = 1/f_s$  is the vortex shedding period of vortices, and  $t_p$  is the phase time varying from 0 to  $T$ . Similar to Lin et al. (2009), the zero phase,  $t_p/T = 0$ , is defined as the phase at which the phase-averaged streamwise velocity  $u_{pa}$  has the zero-up-cross value measured at the point  $(x/D, y/D) = (4,2)$ . Here, a zero-crossing is a point represented by an intercept of the phase-averaged velocity waveform with its axis (at zero value). This velocity waveform (fluctuating velocity) is determined by subtracting the mean value of the phase-averaged streamwise velocity,  $\overline{u_{pa}}$ , from the phase-averaged velocity data measured at a specific point,  $u_{pa}$ , that is

$$Phase\text{-averaged velocity waveform} = u_{pa} - \overline{u_{pa}}, \quad (4.11)$$

then, the zero-crossing of this waveform function can be found. Figure 4.25 shows an example of the wave data of the phase-averaged velocity (after subtracting its average) and its zero up-crossing index (or zero phase).

As mentioned by Carlier and Stanislas (2005), it is necessary to make sure that the detected population is large enough to obtain converged statistics. To do so, the root-mean-square velocity variance, as well as the standard deviation, of the phase-averaged data was calculated at point  $(x/D, y/D) = (4,2)$  for the lowest and highest velocity tested, that is  $U^* = 3.3$  and 6 (Figure 4.26 and Figure 4.27). For the vibrating case, the fluctuations of the rms and std of the phase-averaged data seem to be small enough to consider it stable and invariant, with 290 and 530 sample periods for  $U^* = 3.3$  and 6, respectively. On the other hand, for the static case, the rms value has not converged, meaning that the number of phase-averaged periods, 69 and 129 for  $U^* = 3.3$  and 6, respectively, are not enough to obtain a second order statistically stationary result. However, the std value has started to converge, so the first order statistic data

can be considered reliable. This implies that the phase-averaged data for the vibrating case can fully represent the vortical structures in the wake and is appropriate for second order statistic estimations, while the phase-averaged data of the static case can represent the vorticity and vortex strength but not the second order statistics.

#### 4.5.1 Vorticity and vortex strength

The normalized vorticity contours and contour lines of the actual vortex by  $Q$  criterion are shown in Figure 4.28 and Figure 4.29 for the static and vibrating case, respectively. Regions in red denote positive vorticity, while blue regions have negative vorticity. In the figures, the center of each vortex is also depicted with a star. This center point is defined as the point where the  $Q$  is maximum. The phases visualized are  $t_p/T = 0, 0.2, 0.4, 0.6,$  and  $0.8$ . Note that not all phases can be captured for the static cases, as it can be seen from the number of samples shown in Table 4-7, which shows that the total number of periods in data are insufficient to visualize all the phases for all investigated  $U^*$  values (if the phase cannot be found, results are omitted or N/A is written in the results tables). On the contrary, for the vibrating case this is not an issue, and all phases can be observed.

Results show that, at most, three vortices appear within the examined region: vortex 1, vortex 2 and vortex 3, labeled as V1, V2 and V3, from left to right, respectively (see Figure 4.30 and Figure 4.31). It is clearly seen that the vortex region, obtained by  $Q$  criterion, does not coincide with the vorticity contour. This means that vortices cannot be detected using vorticity contour merely, which agrees with the definition of vortex and vorticity discussed at the beginning of this section, and with that of Jeong and Hussain (1995) too. In addition, the contour lines by  $Q$  criterion show that the real vortex is not in circular shape, but closer to elliptic.

To have a different and more detailed visualization of this, the contours of the vortex strength by  $Q$  criterion are shown in Figure 4.32 and Figure 4.33, for the static and vibrating

case, respectively. For a clearer visualization of the vortices by  $Q$  criterion, the minimum  $Q$  criterion value of the contour was set to be 10% of its maximum value. The vortices in the wake alternate between positive and negative, a pattern corresponding to the 2S mode (as explained in Section 2.4.3). Furthermore, by looking at phase  $t_p/T = 0$ , one can notice the reduction of vorticity and vortex strength as the vortex moves downstream, meaning that the values of vortex 1 and vortex 3 are  $V1 > V3$ .

Figure 4.28, Figure 4.29, Figure 4.32 and Figure 4.33 reveal that when the velocity is higher, the average vorticity magnitude decreases and the vortices present a stronger rate of rotation  $\Omega$ , depicted by a higher  $Q$  magnitude. Moreover, an interesting discovery from these results is that for the static case with  $U^* = 5.3$  the vortex strength (being  $Q = 9.45$  the maximum value) is significantly larger. A reason of  $Q$  being smaller when the cylinder oscillates might be the relative velocity between the free stream and the vibrating cylinder (Hsieh et al., 2017). Thus, vortices and their patterns can be sensitive to the displacement profile of the model in question.

#### 4.5.2 Vortex center location

Few studies from literature have investigated the center of the vortex and its location in the wake flow after a circular cylinder. For this reason, the vortex center is investigated in this study and the results are discussed in this section.

Two different distances were inspected. The distance from the centerline (x-axis) to the vortex center, specified as y-V1, y-V2, and y-V3, as depicted in Figure 4.30, can give us an idea of the development of the vortices as they move downstream. Moreover, the distance between the center of vortex 1 (V1) and vortex 3 (V3), denominated as  $C_{13}$ , as shown in Figure 4.31, can tell us about the vortex pattern.

Table 4-8 to Table 4-11 show the distances y-V1, y-V2, and y-V3, for all cases tested at each phase examined, where values are normalized with respect to the diameter of the model

D. The negative sign represents a position below the centerline. Note that for some phases only two vortices can be seen; when this happens, V3 is not present, so measurements are not applicable, and N/A is written in the result tables. It is clearly seen that for all cases, the absolute value of  $y-V1$  is the smallest, and the absolute value of  $y-V3$  is the largest, meaning that the vortex center is slowly drifting apart from the centerline as the vortex moves further downstream.

In addition, Table 4-8 shows that distances of vortices for both static and vibrating cases are similar at phase  $t_p/T = 0$ , which might be due to the fact that at  $U^* = 3.3$ , for the vibrating case, the elastic system has not reached the lock-in range, meaning that the amplitude of oscillations are minor, causing the shedding of vortices to be very similar to the static case. However, for cases  $U^* = 4.6, 5.3,$  and  $6$ , the difference of distance between vortices of the static and vibrating case is increased. This is shown in Figure 4.34, which shows a comparison of every vortex center location at phase  $t_p/T = 0$  between the static and the vibrating case for each  $U^*$  tested. Interestingly, when the cylinder oscillates, the distance from the x-axis to the vortex center is greatest at the resonance state ( $U^* = 5.3$ ), when the amplitude of oscillation is largest as disclosed before.

Additionally, the path of what is V1 at  $t_p/T = 0$  during one whole period is illustrated in Figure 4.35, which compares  $U^* = 3.3, 4.6, 5.3,$  and  $6$  of the vibrating case. This path shows the distance from the centerline to the center of that specific vortex at each phase. Note that the same vortex becomes V3 at  $t_p/T = 8$ . It is apparent that during resonance ( $U^* = 5.3$ ) the distance is greatest, and it increases with the phase. On the other hand, for the case outside the lock-in range ( $U^* = 3.3$ ), the distance is the shortest and it remains mostly constant during one period. This reveals once again that the vortex behavior is related to the amplitude of oscillation of the cylinder.

In a like manner, the values of  $C_{13}$ , normalized with respect to the diameter of the model  $D$ , are shown in Table 4-12 to Table 4-15. Also, Figure 4.36 shows a comparison of  $C_{13}$  at  $t_p/T = 0$  between the static and the vibrating cases for each  $U^*$ . In this case, for the vibrating case,  $C_{13}$  is smallest for  $U^* = 4.6$ , which is within the lock-in range at the initial branch (see Table 4-13). However, the distance between V1 and V3 are larger for the static case, which is an interesting finding. Because if one looks at the vortex shedding frequency  $f_s$  ( $f_s$  of static case  $> f_s$  of vibrating case), one would imply that vortices will be closer to each other in the static case. However, results differ from this assumption and show that vortices are actually farther apart from each other when the cylinder is static. One possible reason of this feature is the vertical displacements (i.e. y-V1, discussed earlier) that the vortices have when the cylinder oscillates. It is also known that the displacement profile affects the relative velocity between the freestream and the vibrating cylinder (Hsieh et al., 2017), something that might affect the distance between vortices. This corroborates one more time that the amplitude of oscillation affects the shedding of vortices and their behavior in the wake. The larger the amplitude is, the farther away the vortices in the wake are from the centerline.

#### 4.6 Phase-averaged velocity decomposition

The results of vortex and vorticity discussed earlier are evidence of the large-scale coherent structures present in the wake. This study explores the turbulent characteristics of the phase-averaged coherent structures (i.e., a non-stationary flow) in this section.

A discrete time interval is used to capture the mean motion of velocity  $u(t)$  at the specific time  $t$  in a period, as described in Section 4.5. The phase-averaged data is obtained by calculating the mean of the data captured at every period  $T$ , as follows

$$u_{i\ pa} = \frac{1}{T_{Np}} \sum_{n=0}^{T_{Np}} u_i(nT). \quad (4.12)$$

It is composed of a mean and a fluctuating velocity component, that is

$$u_{i pa} = \overline{u_{i pa}} + (u_{i pa})', \quad (4.13)$$

where  $i = 1, 2$  denotes the  $u$  and  $v$  components, respectively. Its fluctuating component can be determined as in Equation 4.11. Points  $(x/D, y/D) = (4, 0.5)$  and  $(4, 1)$  (as depicted in Figure 4.37 with red dots) were selected as examples to compute the fluctuating part of the phase-averaged velocity  $u$  defined in Equation 4.13 as a function of the phase  $t_p/T$  for  $U^* = 6$ , as shown in Figure 4.38 and Figure 4.39 (normalized with  $U_f$ ), respectively. It exhibits, to some extent, a periodical response. However, the random peaks that repeat in each period on the  $(u_{pa})'$  curve shown in Figure 4.38 a) and Figure 4.39 a) indicate the existence of fluctuating components. Thus,  $(u_{i pa})'$  is further separated into a quasiperiodic part  $\tilde{u}_{i pa}$  and a “real fluctuating” part  $(u_{i pa})''$ , as the triple decomposition analysis defines, that is

$$(u_{i pa})' = \tilde{u}_{i pa}(t/T) + (u_{i pa})''(t/T). \quad (4.14)$$

Consequently, the phase-averaged velocity can be expressed as

$$u_{i pa} = \overline{u_{i pa}} + \tilde{u}_{i pa}(t/T) + (u_{i pa})''(t/T). \quad (4.15)$$

The real fluctuation of the velocity can be, thus, calculated by phase averaging the fluctuating component of the velocity ( $u_i'$ ), as follows

$$(u_{i pa})'' = u_{i pa} - \overline{u_{i pa}} - \tilde{u}_{i pa} = \frac{1}{T_{Np}} \sum_{n=1}^{T_{Np}} u_i'(nT). \quad (4.16)$$

The responses of the real root-mean-square streamwise velocity, that is  $(u_{i pa})''_{rms}$ , within one arbitrary period calculated at the two different points mentioned earlier, are shown in Figure 4.38 c), Figure 4.39 c). It can be observed that the behaviors of the responses are different at each lateral position. The wider ranges of  $(u_{i pa})'$  in Figure 4.39 reveal that a stronger velocity fluctuation is developed at  $(x/D, y/D) = (4, 1)$ . Additionally, Figure 4.40 and Figure 4.41 show the same responses, that is  $(u_{i pa})'$  and  $(u_{i pa})''_{rms}$ , but normalized with

the mean of the phase-averaged velocity,  $\overline{u_{pa}}$ , at each position. This is done to detect the actual magnitude of the response of the phase-averaged fluctuating velocities at each specific position.

The time histories of  $u_{i pa}$  and the root-mean-square of  $(u_{i pa})''$  during one period  $t_p/T$  for all  $U^*$  cases tested are shown in Figure 4.42. The two different points displayed in Figure 4.37 were computed, that is,  $(x/D, y/D) = (4, 0.5)$  and  $(4, 1)$ . It reveals a fact that the real root-mean-square streamwise velocity is still a function of time ( $t_p/T$ ) in each period, as it is not a constant value. Note that the y-axis ranges in Figure 4.42 have been adjusted for a clearer visualization. The phase-averaged data shows a periodic behavior, while the rms data shows more random results. This agrees with the definitions of the phase-averaged velocity decomposition presented earlier. For instance, the phase-averaged velocity  $u_{i pa}$  is composed of a mean, a quasiperiodic and a real fluctuating component (Equation 4.15), thus its time history displays a periodic-like behavior. On the other hand, the root-mean-square results of the phase-averaged fluctuating component  $(u_{i pa})''$  are, in fact, the “real fluctuating” velocity, which is the small-scale turbulence characteristic.

Table 4-1 Maximum error percentage of mean streamwise velocity profile between HWA and PIV using oil and solid particles at different stations for  $Re = 1.3 \times 10^4$  and  $Re = 2.4 \times 10^4$ .

Re	Position X	Error %	
		HWA vs PIV (oil)	HWA vs PIV (solid)
13000	2D	31.3%	28.3%
	4D	12.6%	8.1%
	6D	13.2%	6.6%
24000	2D	13.9%	2.7%
	4D	2.7%	1.3%
	6D	3.1%	1.8%

Table 4-2 Summary of the normalized standard deviations ( $\sigma$ ) and standard errors (SE) of the mean streamwise velocity at different positions.

Re	Position X	$\sigma$ (Normalized)	SE (Normalized)	SE (m/s)
13000	3D	0.1267	0.00073	0.0035
	4D	0.1276	0.00074	0.0035
	5D	0.1234	0.00071	0.0034
	6D	0.1210	0.00070	0.0033
	7D	0.1193	0.00069	0.0033
24000	3D	0.1033	0.00059	0.0053
	4D	0.1061	0.00061	0.0055
	5D	0.1058	0.00061	0.0055
	6D	0.1014	0.00058	0.0052
	7D	0.0973	0.00056	0.0050

Table 4-3 Frequency results obtained from HWA experiments for four different  $U^*$  cases at both stations  $x/D = 4$  and  $6$ .

x/D	$U^*$	Velocity fluctuation frequency (Hz)	Vibration frequency (Hz)	
4D	3.3	4.1	4.2	9.7
	4.6	8	8	9.7
	5.3	9.7	9.7	
	6	11	9.7	11
6D	3.3	4.2	4.1	9.7
	4.6	8.1	8.2	9.7
	5.3	9.7	9.7	
	3.3	11	9.7	11

Table 4-4 Vortex shedding frequency and Strouhal number results obtained from HWA tests for each case tested.

Case	U*	Re ( $\times 10^4$ )	fs	St
Static	3.3	2.0	7.8	0.24
	4.6	2.8	10.4	0.23
	5.3	3.3	11.8	0.23
	6	3.8	13	0.22
Vibrating	3.3	2.0	4	0.12
	4.6	2.8	8	0.18
	5.3	3.3	9.7	0.19
	3.3	3.8	11.2	0.19

Table 4-5 Upper and lower limits (k1, k2) of the inertial subrange shown in the energy density spectrum (Figure 4.23) of each case tested.

U*	Static		Vibrating	
	k1 (Hz)	k2 (Hz)	k1 (Hz)	k2 (Hz)
3.3	40	400	55	140
4.6	78	430	23	222
5.3	97	790	175	595
6	164	630	85	595

Table 4-6 Integral and Taylor length scales of each case tested, measured at two different stations,  $x/D = 4$  and  $6$ , for both static and vibrating cylinders. Note: values are expressed in micrometers ( $\mu m$ ).

Case	U*	4D		6D	
		$\Lambda_x \times 10^4$ ( $\mu m$ )	$\lambda_x \times 10^3$ ( $\mu m$ )	$\Lambda_x \times 10^4$ ( $\mu m$ )	$\lambda_x \times 10^3$ ( $\mu m$ )
Static	3.3	1.06	6.7	1.02	7.7
	4.6	1.07	8.2	1.31	9.2
	5.3	1.15	7.9	1.79	9.2
	6	1.36	8.7	1.57	8.6
Vibrating	3.3	2.36	8	2.61	6.4
	4.6	1.76	9.7	2.35	9.7
	5.3	1.62	8.7	2.17	9.6
	6	1.71	8.7	2.34	9.1

Table 4-7 Number of samples in one period ( $N_p$ ), total number of periods in data ( $T_{N_p}$ ), and the first zero-up-cross sample of each case tested.

Case	$U^*$	$N_p$	$T_{N_p}$	First zero-up-cross
Static	3.3	290	69	27
	4.6	213	94	43
	5.3	179	112	53
	6	155	129	24
Vibrating	3.3	151	290	40
	4.6	111	332	111
	5.3	103	426	232
	6	82	530	39

Table 4-8 Distances from the center of vortex 1, vortex 2 and vortex 3, to the x-axis (normalized with D), defined as y-V1, y-V2, and y-V3, respectively. Results of static and vibrating cases at  $U^*=3.3$  for different phases ( $t_p/T$ ).

$U^*=3.3$						
Phase	Vibrating			Static		
	y-V1	y-V2	y-V3	y-V1	y-V2	y-V3
<b>0</b>	0.25	-0.38	0.48	-0.28	0.32	-0.54
<b>0.2</b>	0.33	-0.38	0.56	N/A	N/A	N/A
<b>0.4</b>	-0.31	0.33	-0.38	N/A	N/A	N/A
<b>0.6</b>	-0.38	0.33	-0.46	N/A	N/A	N/A
<b>0.8</b>	0.33	-0.31	0.33	N/A	N/A	N/A

Table 4-9 Distances from the center of vortex 1, vortex 2 and vortex 3, to the x-axis (normalized with D), defined as y-V1, y-V2, and y-V3, respectively. Results of static and vibrating cases at  $U^*=4.6$  for different phases ( $t_p/T$ ).

$U^*=4.6$						
Phase	Vibrating			Static		
	y-V1	y-V2	y-V3	y-V1	y-V2	y-V3
<b>0</b>	-0.31	0.40	-0.54	-0.27	0.14	-0.45
<b>0.2</b>	-0.42	0.40	-1.01	-0.21	0.26	N/A
<b>0.4</b>	-0.54	0.52	-1.01	N/A	N/A	N/A
<b>0.6</b>	0.29	-0.42	0.40	N/A	N/A	N/A
<b>0.8</b>	0.40	-0.54	0.76	N/A	N/A	N/A

Table 4-10 Distances from the center of vortex 1, vortex 2 and vortex 3, to the x-axis (normalized with D), defined as y-V1, y-V2, and y-V3, respectively. Results of static and vibrating cases at  $U^*=5.3$  for different phases ( $t_p/T$ ).

<b><math>U^*=5.3</math></b>						
<b>Phase</b>	<b>Vibrating</b>			<b>Static</b>		
	<b>y-V1</b>	<b>y-V2</b>	<b>y-V3</b>	<b>y-V1</b>	<b>y-V2</b>	<b>y-V3</b>
<b>0</b>	0.52	-0.66	N/A	0.18	-0.45	0.50
<b>0.2</b>	-0.42	0.52	-1.01	-0.21	0.18	-0.53
<b>0.4</b>	-0.42	0.52	N/A	N/A	N/A	N/A
<b>0.6</b>	0.40	-0.42	0.64	N/A	N/A	N/A
<b>0.8</b>	0.40	-0.42	0.88	N/A	N/A	N/A

Table 4-11 Distances from the center of vortex 1, vortex 2 and vortex 3, to the x-axis (normalized with D), defined as y-V1, y-V2, and y-V3, respectively. Results of static and vibrating cases at  $U^*=6$  for different phases ( $t_p/T$ ).

<b><math>U^*=6</math></b>						
<b>Phase</b>	<b>Vibrating</b>			<b>Static</b>		
	<b>y-V1</b>	<b>y-V2</b>	<b>y-V3</b>	<b>y-V1</b>	<b>y-V2</b>	<b>y-V3</b>
<b>0</b>	0.33	-0.46	N/A	0.18	-0.29	0.58
<b>0.2</b>	-0.31	0.48	-0.62	-0.29	0.26	-0.37
<b>0.4</b>	-0.31	0.48	-0.62	-0.37	0.34	-0.54
<b>0.6</b>	0.48	-0.31	0.64	-0.37	0.42	-0.53
<b>0.8</b>	0.33	-0.46	0.64	N/A	N/A	N/A

Table 4-12 Distances between vortex 1 (V1) and vortex 3 (V3), defined as  $C_{13}$  (normalized with D), of static and vibrating case at  $U^* = 3.3$  for different phases ( $t_p/T$ ).

<b><math>U^*=3.3</math></b>		
<b>Phase</b>	<b><math>C_{13}</math></b>	
	<b>Vibrating</b>	<b>Static</b>
<b>0</b>	3.55	3.73
<b>0.2</b>	3.55	N/A
<b>0.4</b>	3.07	N/A
<b>0.6</b>	3.39	N/A
<b>0.8</b>	3.07	N/A

Table 4-13 Distances between vortex 1 (V1) and vortex 3 (V3), defined as  $C_{13}$  (normalized with D), of static and vibrating case at  $U^* = 4.6$  for different phases ( $t_p/T$ ).

<b>U*=4.6</b>		
<b>Phase</b>	<b>C<sub>13</sub></b>	
	<b>Vibrating</b>	<b>Static</b>
<b>0</b>	2.73	4.14
<b>0.2</b>	3.25	N/A
<b>0.4</b>	2.53	N/A
<b>0.6</b>	3.25	N/A
<b>0.8</b>	2.98	N/A

Table 4-14 Distances between vortex 1 (V1) and vortex 3 (V3), defined as  $C_{13}$  (normalized with D), of static and vibrating case at  $U^* = 5.3$  for different phases ( $t_p/T$ ).

<b>U*=5.3</b>		
<b>Phase</b>	<b>C<sub>13</sub></b>	
	<b>Vibrating</b>	<b>Static</b>
<b>0</b>	N/A	3.67
<b>0.2</b>	3.48	3.61
<b>0.4</b>	N/A	N/A
<b>0.6</b>	3.91	N/A
<b>0.8</b>	3.70	N/A

Table 4-15 Distances between vortex 1 (V1) and vortex 3 (V3), defined as  $C_{13}$  (normalized with D), of static and vibrating case at  $U^* = 6$  for different phases ( $t_p/T$ ).

<b>U*=6</b>		
<b>Phase</b>	<b>C<sub>13</sub></b>	
	<b>Vibrating</b>	<b>Static</b>
<b>0</b>	N/A	3.78
<b>0.2</b>	3.48	3.44
<b>0.4</b>	3.17	3.84
<b>0.6</b>	3.16	3.44
<b>0.8</b>	3.48	N/A

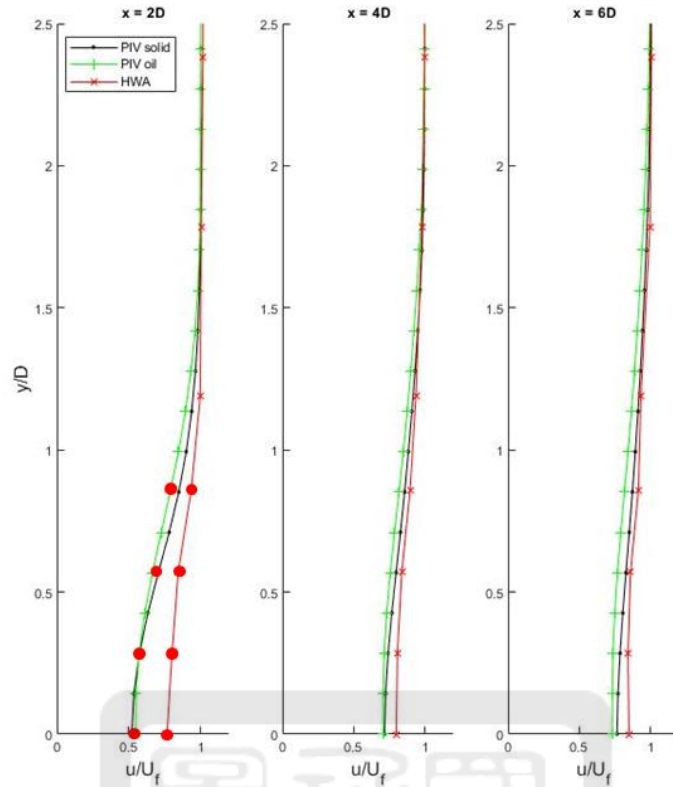


Figure 4.1. Comparison of mean streamwise velocity profiles obtained with PIV solid, PIV oil, and HWA at  $Re = 1.3 \times 10^4$  and at the stations of  $x/D = 2, 4, 6$ .

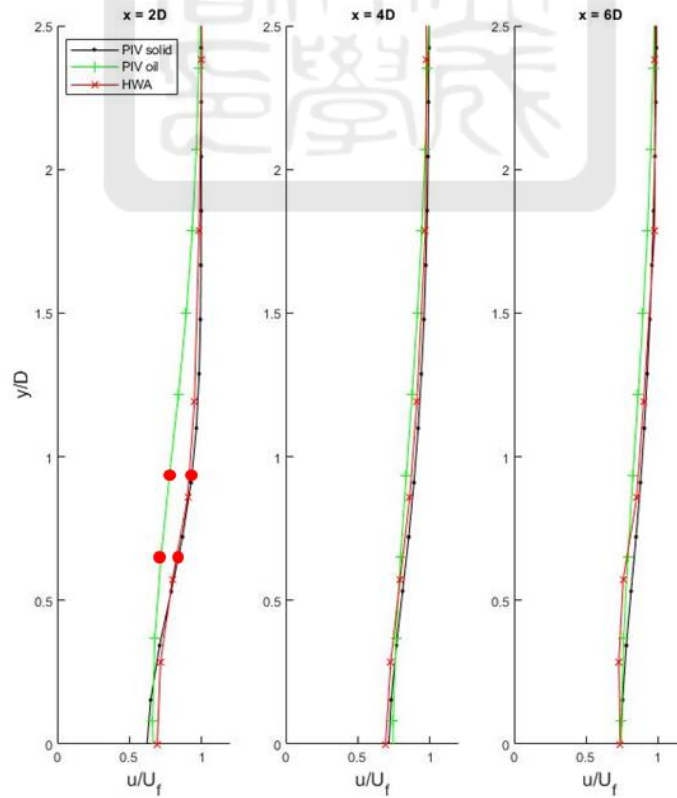


Figure 4.2. Comparison of mean streamwise velocity profiles obtained with PIV solid, PIV oil, and HWA at  $Re = 2.4 \times 10^4$  and at the stations of  $x/D = 2, 4, 6$ .

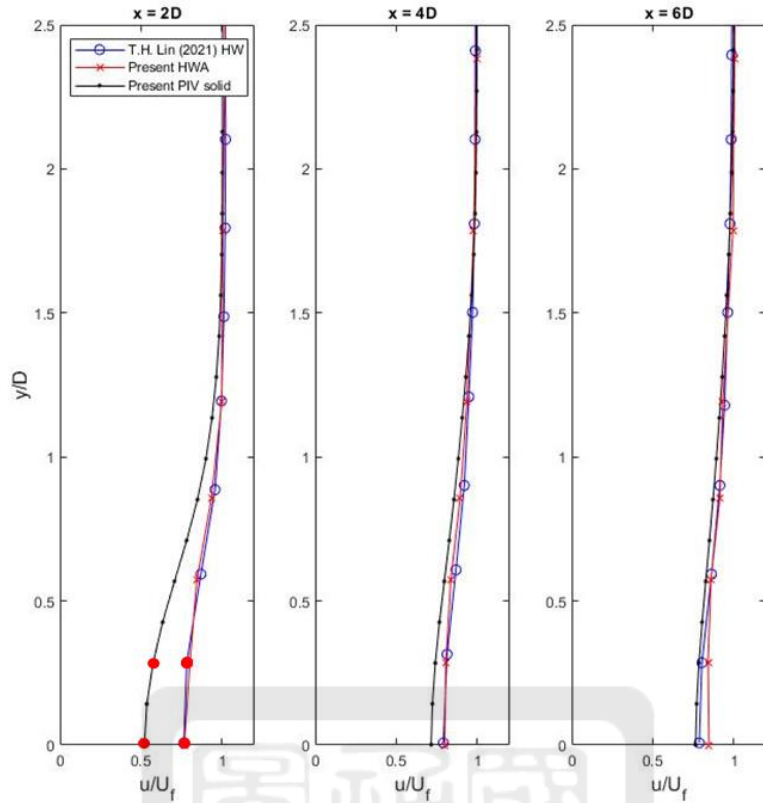


Figure 4.3. Comparison of mean streamwise velocity profiles between present PIV solid, and HWA results and Lin (2021) HWA results at  $Re = 1.3 \times 10^4$  and at the stations of  $x/D = 2, 4$  and  $6$ .

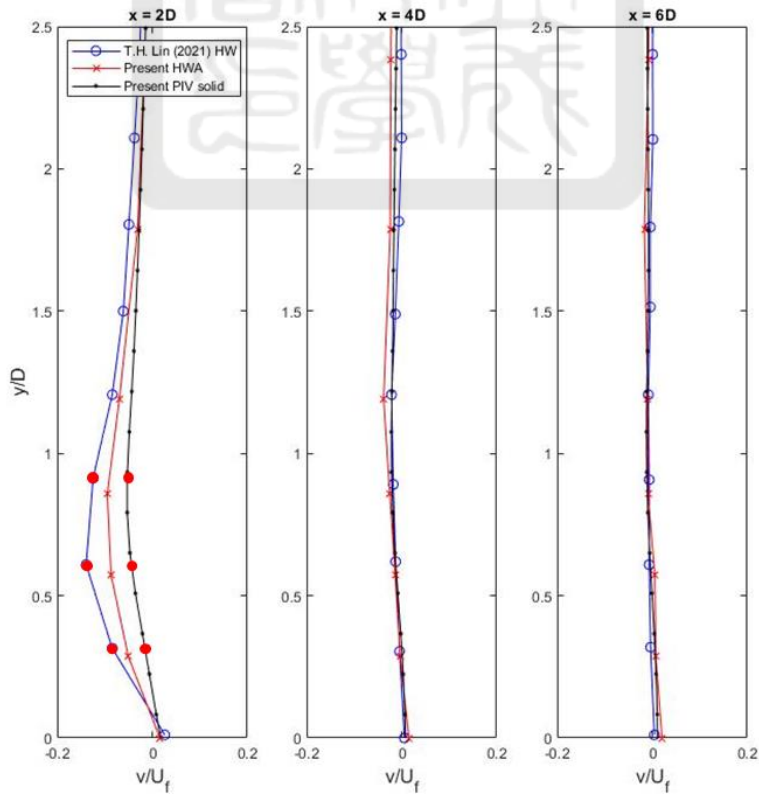


Figure 4.4. Comparison of mean lateral velocity profiles between present PIV solid, and HWA results and Lin (2021) HWA results at  $Re = 1.3 \times 10^4$  and at the stations of  $x/D = 2, 4$  and  $6$ .

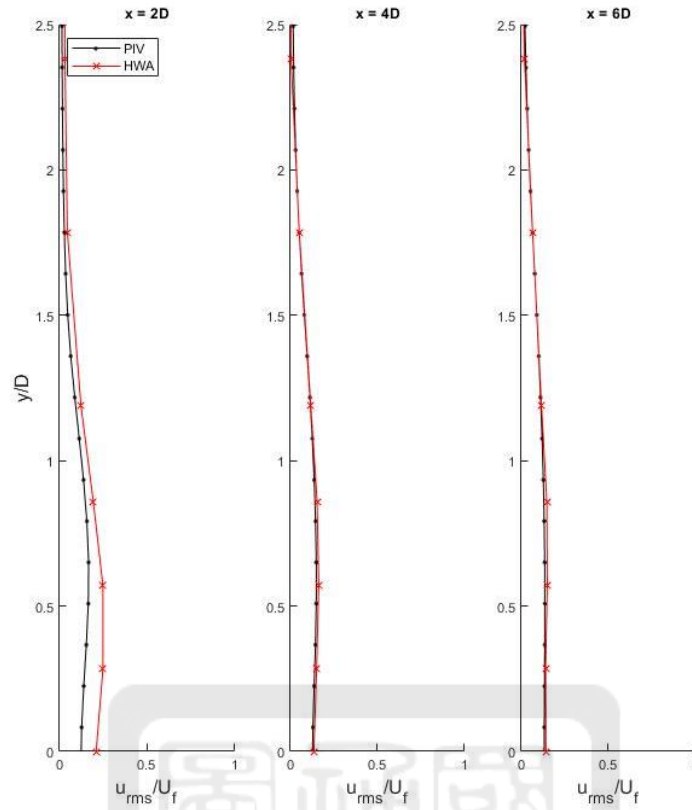


Figure 4.5. Comparison of root-mean-square streamwise velocity profiles obtained with PIV and HWA at  $Re = 1.3 \times 10^4$  and at the stations of  $x/D = 2, 4$  and  $6$ .

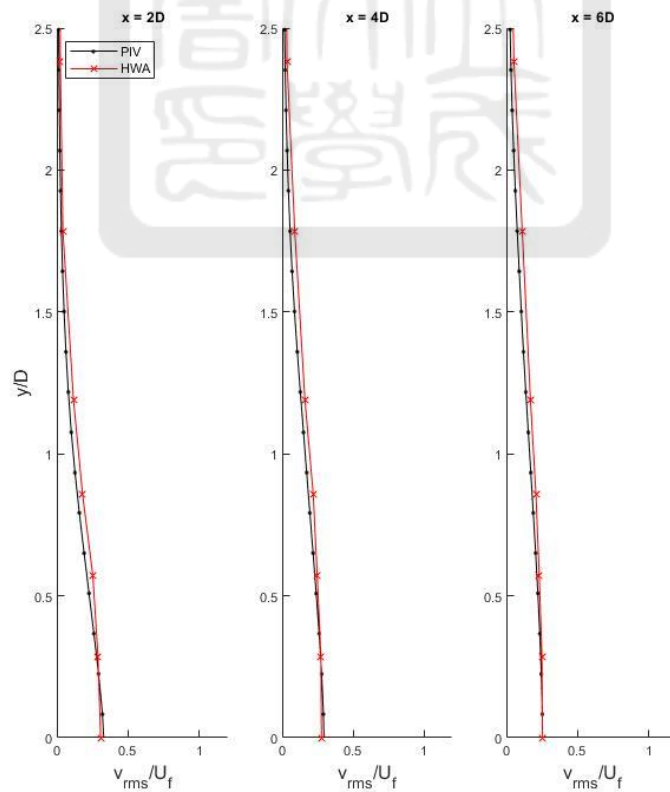


Figure 4.6. Comparison of root-mean-square lateral velocity profiles obtained with PIV and HWA at  $Re = 1.3 \times 10^4$  and at the stations of  $x/D = 2, 4$  and  $6$ .

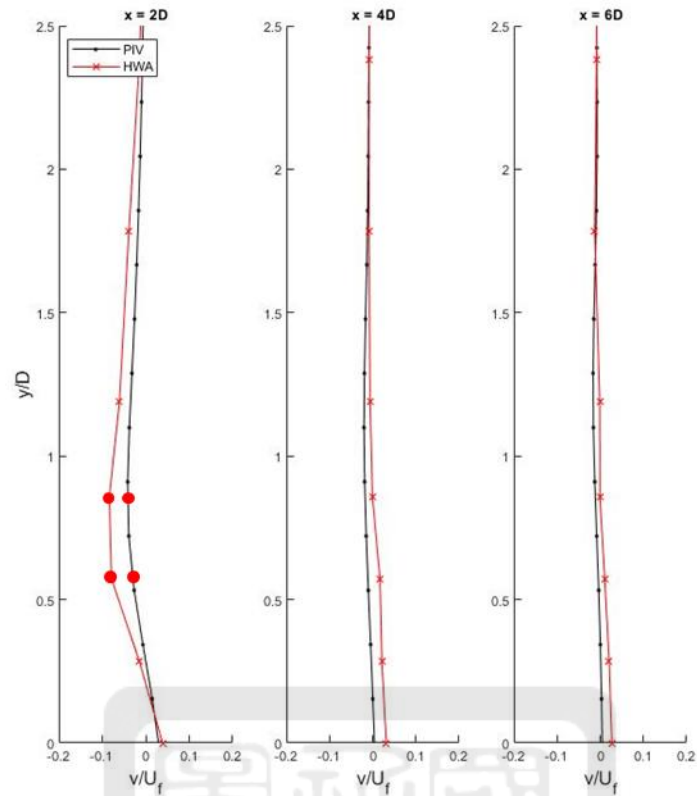


Figure 4.7. Comparison of mean lateral velocity profiles obtained with PIV and HWA at  $Re = 2.4 \times 10^4$  and at the stations of  $x/D = 2, 4$  and  $6$ .

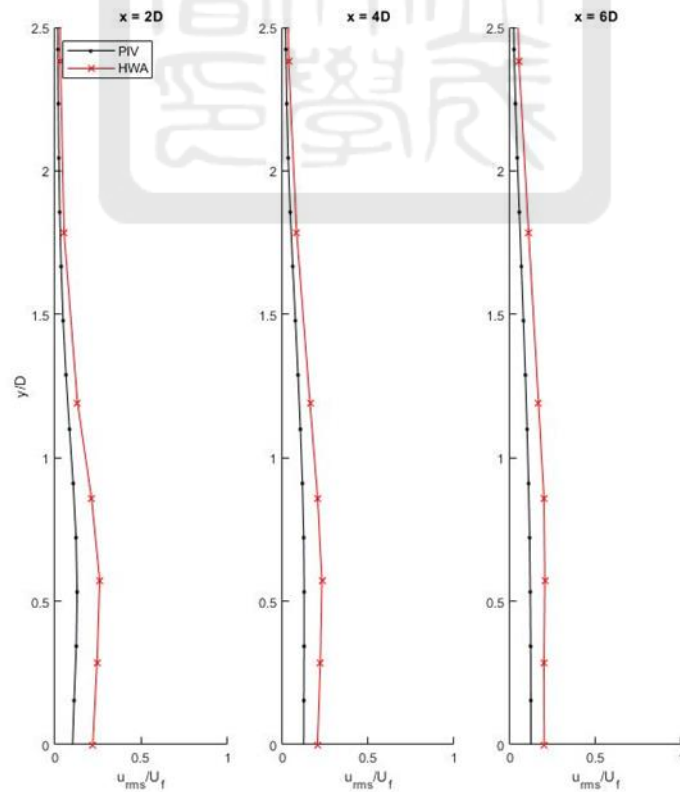


Figure 4.8. Comparison of root-mean-square streamwise velocity profiles obtained with PIV and HWA at  $Re = 2.4 \times 10^4$  and at the stations of  $x/D = 2, 4$  and  $6$ .

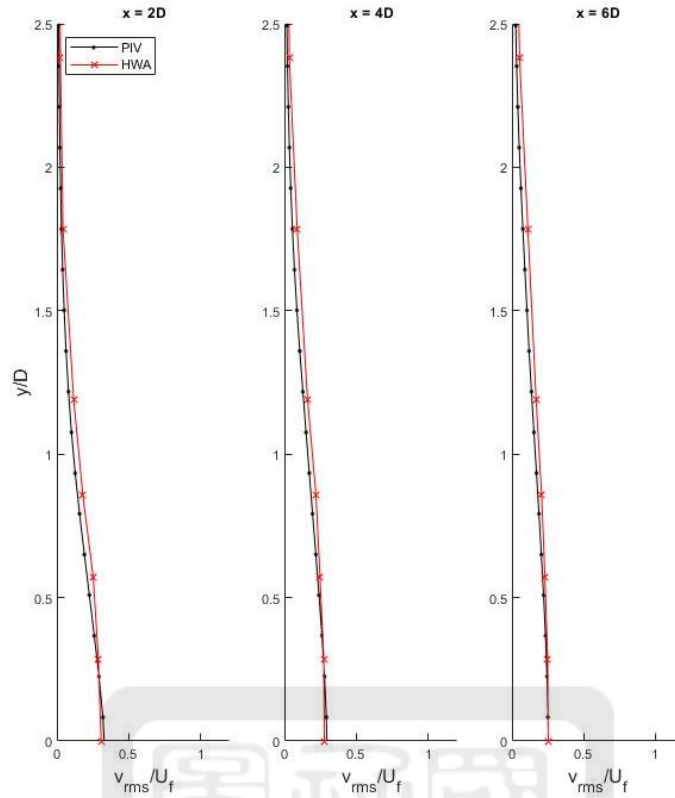


Figure 4.9. Comparison of root-mean-square lateral velocity profiles obtained with PIV and HWA at  $Re = 2.4 \times 10^4$  and at the stations of  $x/D = 2, 4$  and  $6$ .

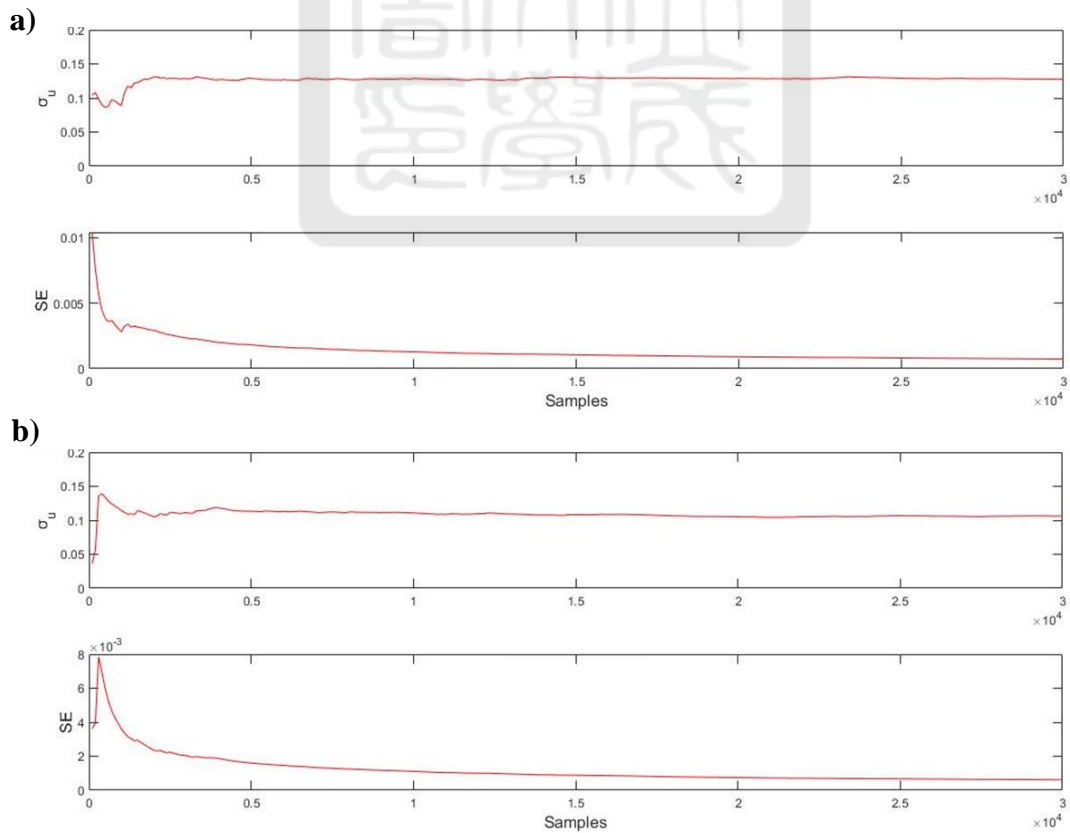


Figure 4.10. Variations of standard deviations and standard errors of mean streamwise velocity taken at the point ( $x/D=4, y/D=1$ ) for a)  $Re = 1.3 \times 10^4$  and b)  $Re = 2.4 \times 10^4$ . \*Values are normalized with free stream velocity.

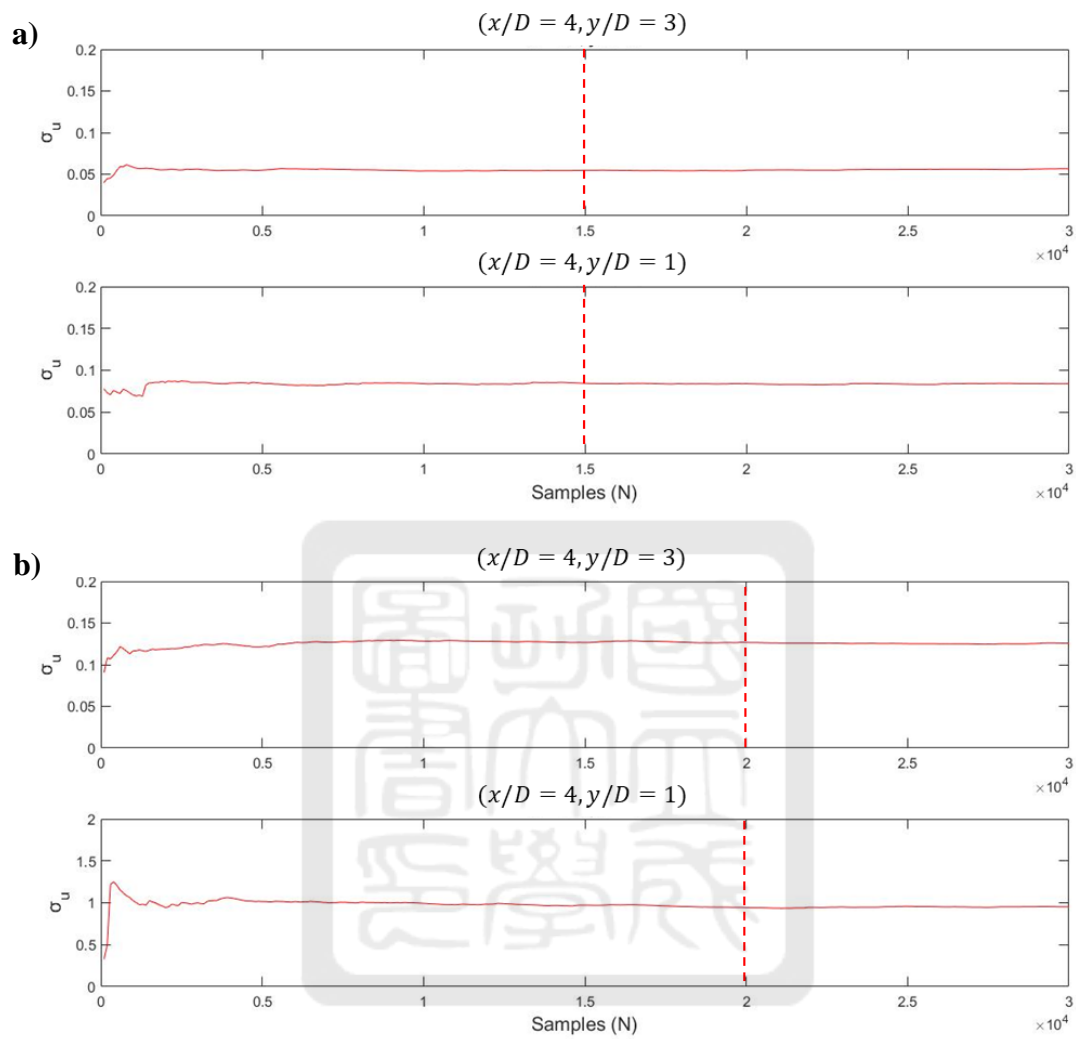


Figure 4.11. Variations of standard deviations of mean streamwise velocity taken at the points  $(x/D=4, y/D=1)$  and  $(4, 3)$  for a)  $Re = 1.3 \times 10^4$  and b)  $Re = 2.4 \times 10^4$ .

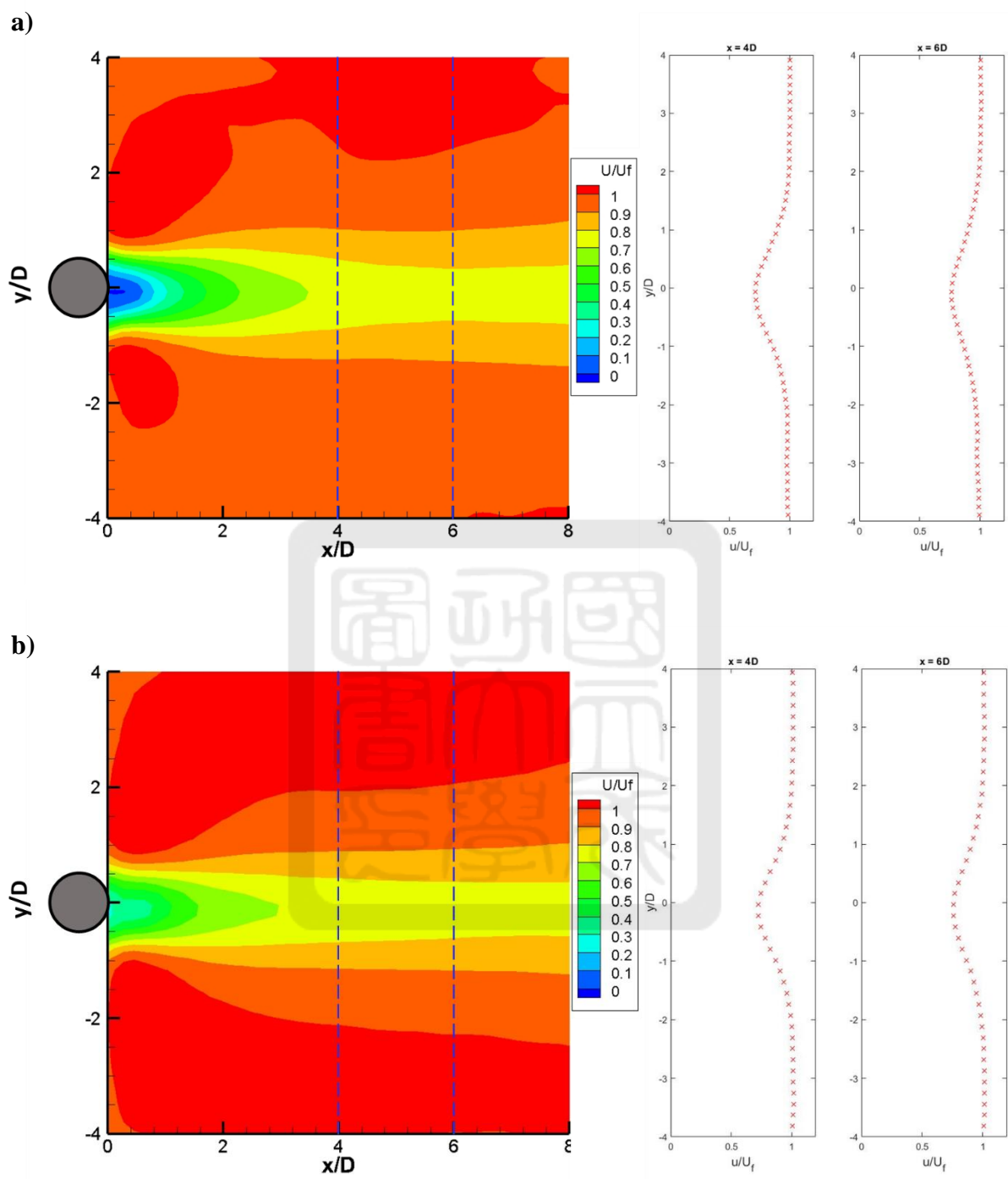


Figure 4.12. Mean streamwise velocity contour and velocity profiles for stations  $x/D=4$  and  $6$ , at a)  $Re = 1.3 \times 10^4$  and b)  $Re = 2.4 \times 10^4$ . \*Static case using Model 1.

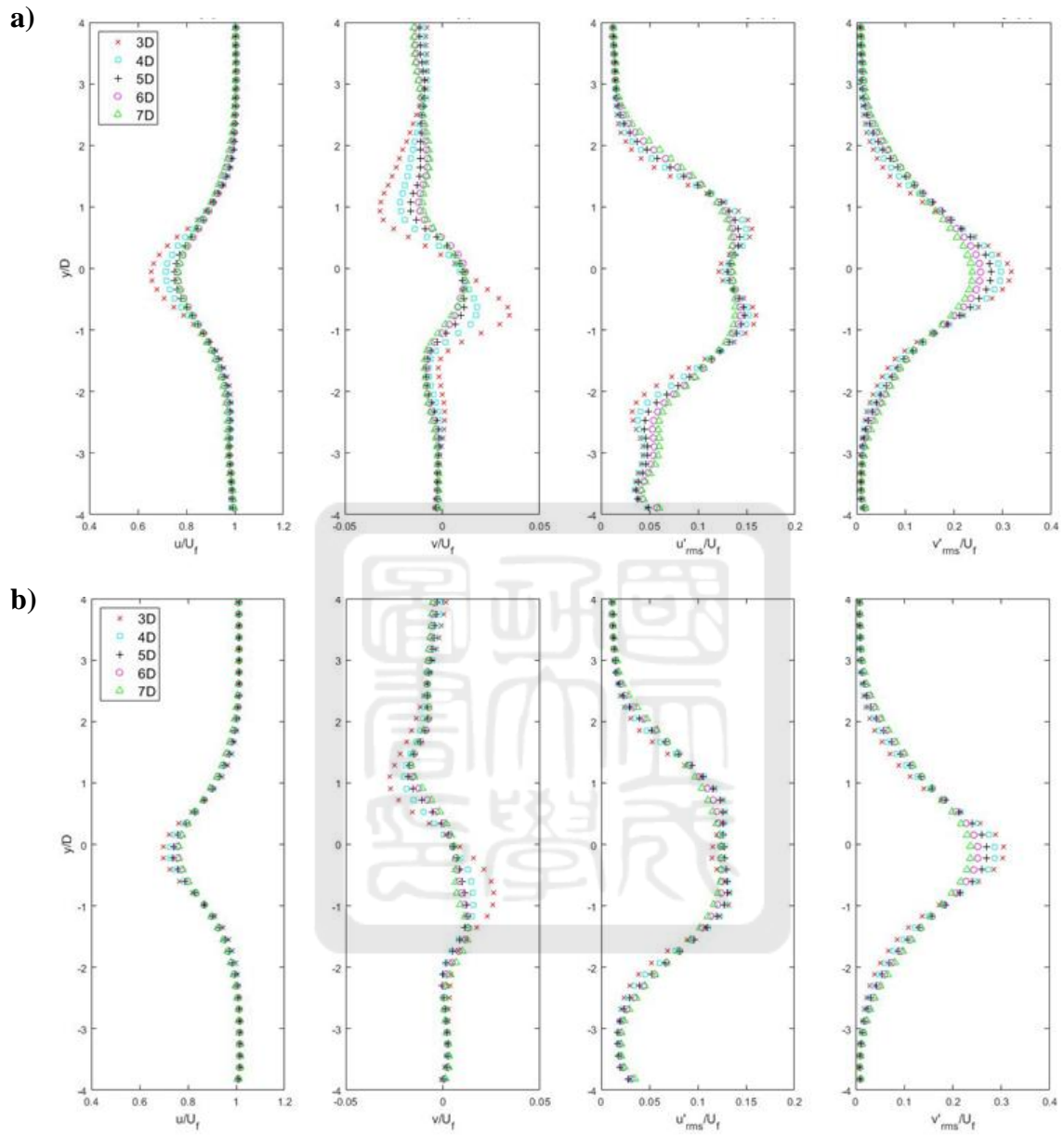


Figure 4.13. Normalized streamwise and lateral mean and root-mean-square velocity profiles at different stations ( $x/D = 3, 4, 5, 6$  and  $7$ ) for a)  $Re = 1.3 \times 10^4$  and b)  $Re = 2.4 \times 10^4$ . \*Static case using Model 1.

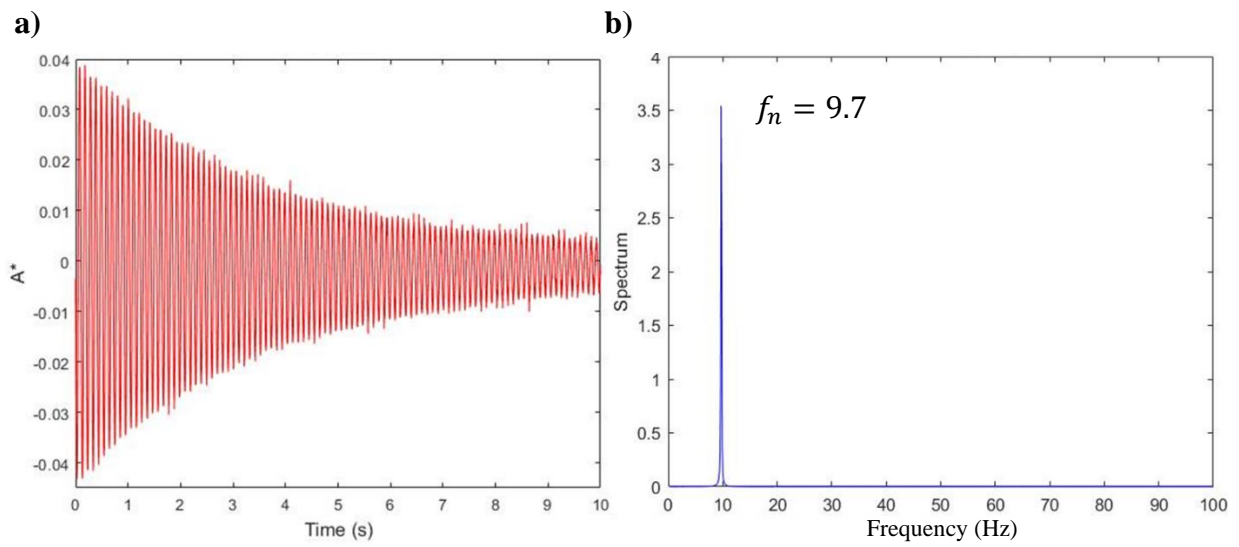


Figure 4.14. a) Decay curve of displacement after an initial excitation, and b) the structural natural frequency  $f_n$  determined by FFT.

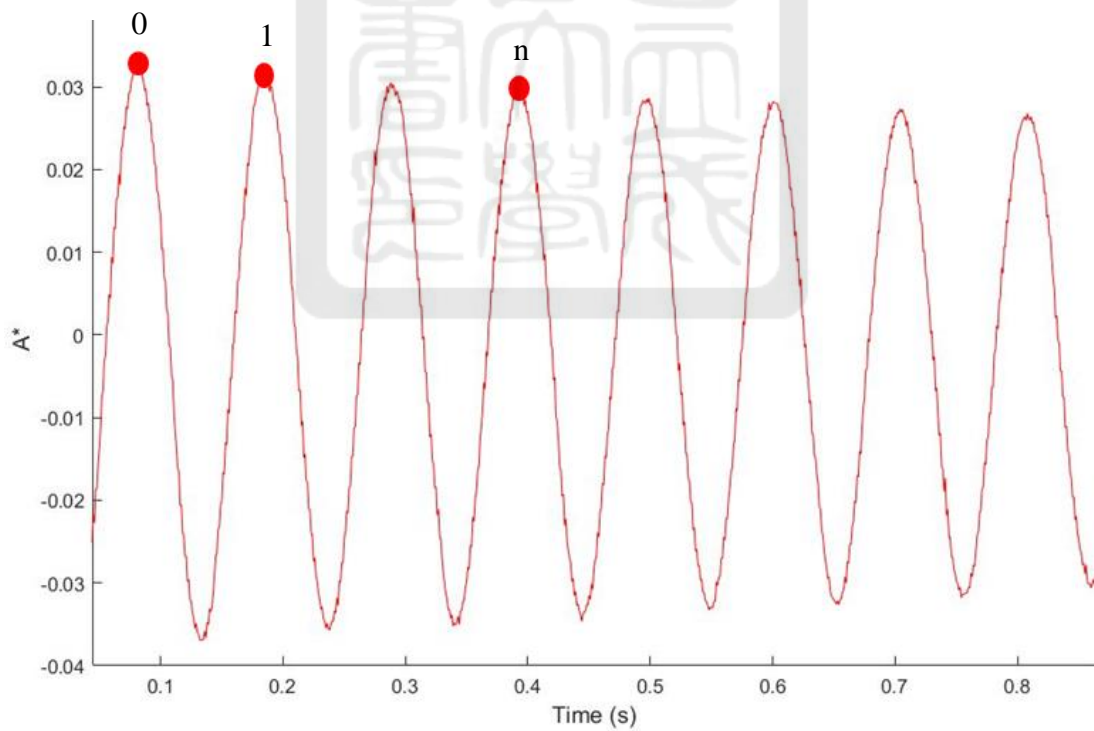


Figure 4.15. Close up of the free decay amplitude curve with three peaks identified as peak 0, peak 1, and peak n, highlighted with a red point.

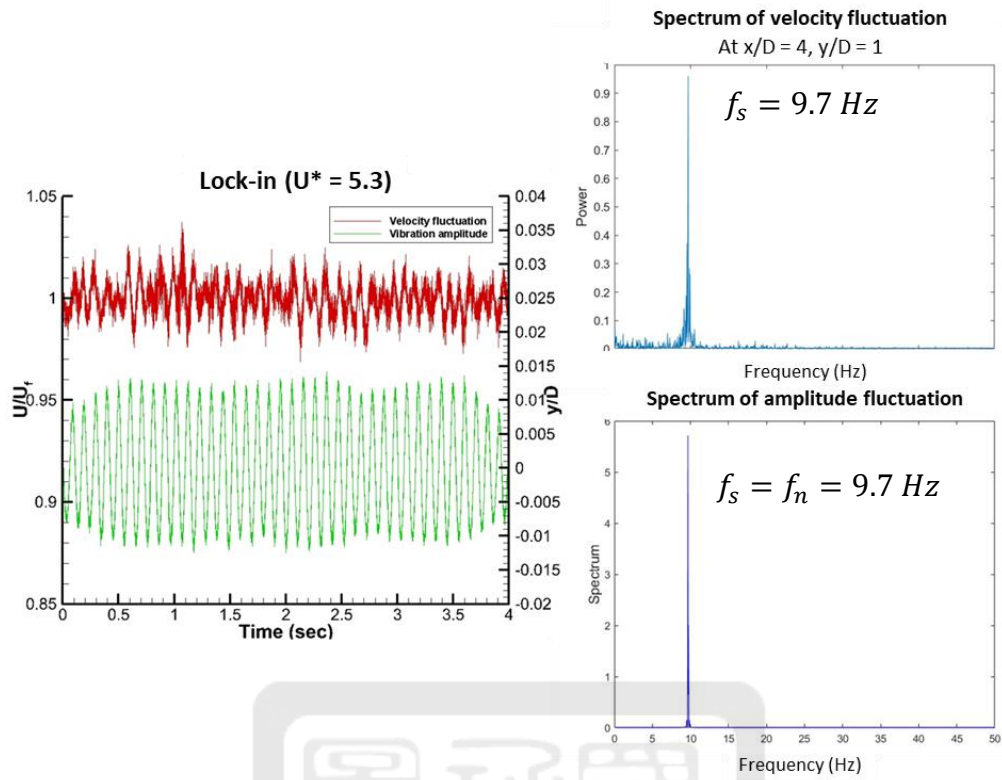


Figure 4.16. Time histories and spectra of cylinder vibrations and velocity fluctuations for the case of  $U^* = 5.3$ . a) Time histories of velocity fluctuation (red) and vibration amplitude (green), b) velocity fluctuation spectrum, and c) amplitude fluctuation spectrum.

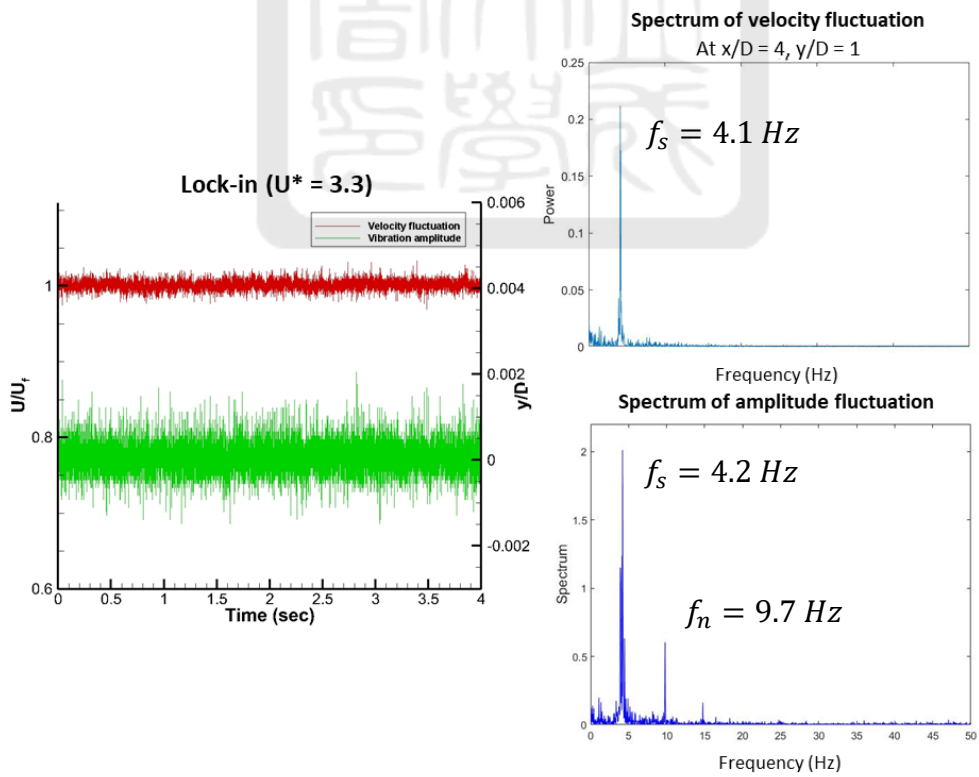


Figure 4.17. Time histories and spectra of cylinder vibrations and velocity fluctuations for the case of  $U^* = 3.3$ . a) Time histories of velocity fluctuation (red) and vibration amplitude (green), b) velocity fluctuation spectrum, and c) amplitude fluctuation spectrum.

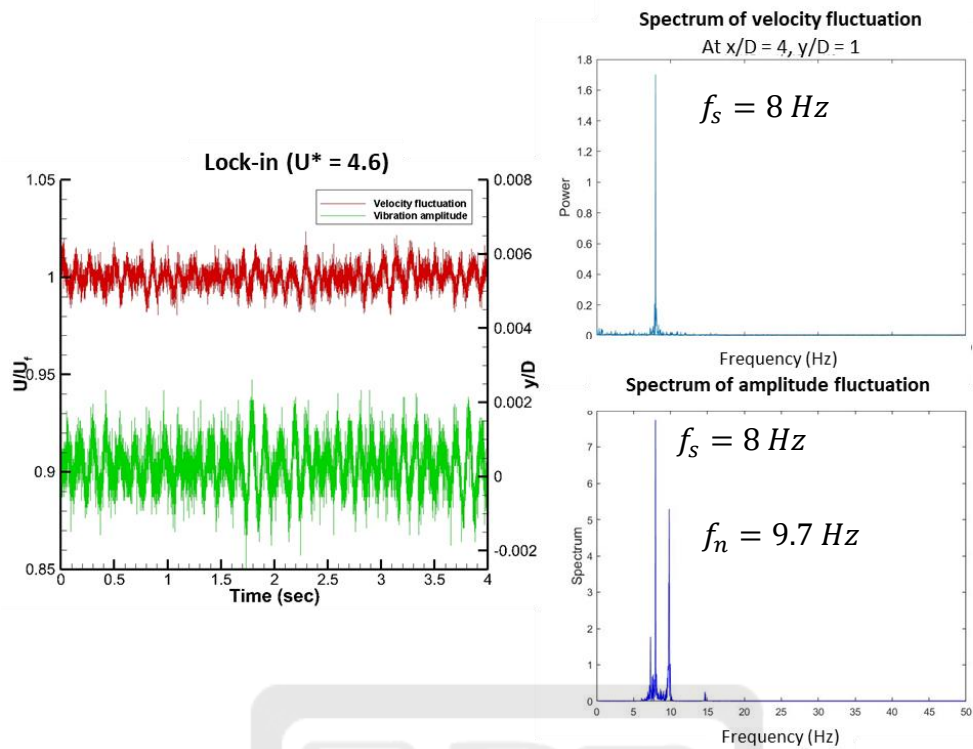


Figure 4.18. Time histories and spectra of cylinder vibrations and velocity fluctuations for the case of  $U^* = 4.6$ . a) Time histories of velocity fluctuation (red) and vibration amplitude (green), b) velocity fluctuation spectrum, and c) amplitude fluctuation spectrum.

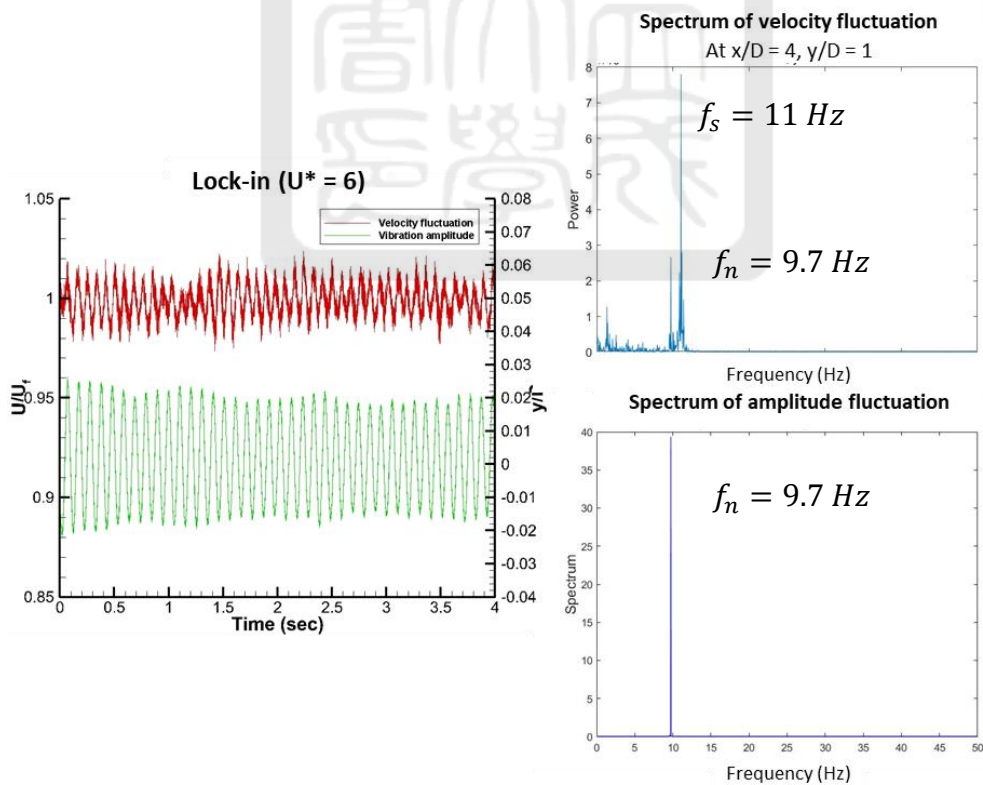


Figure 4.19. Time histories and spectra of cylinder vibrations and velocity fluctuations for the case of  $U^* = 6$ . a) Time histories of velocity fluctuation (red) and vibration amplitude (green), b) velocity fluctuation spectrum, and c) amplitude fluctuation spectrum.

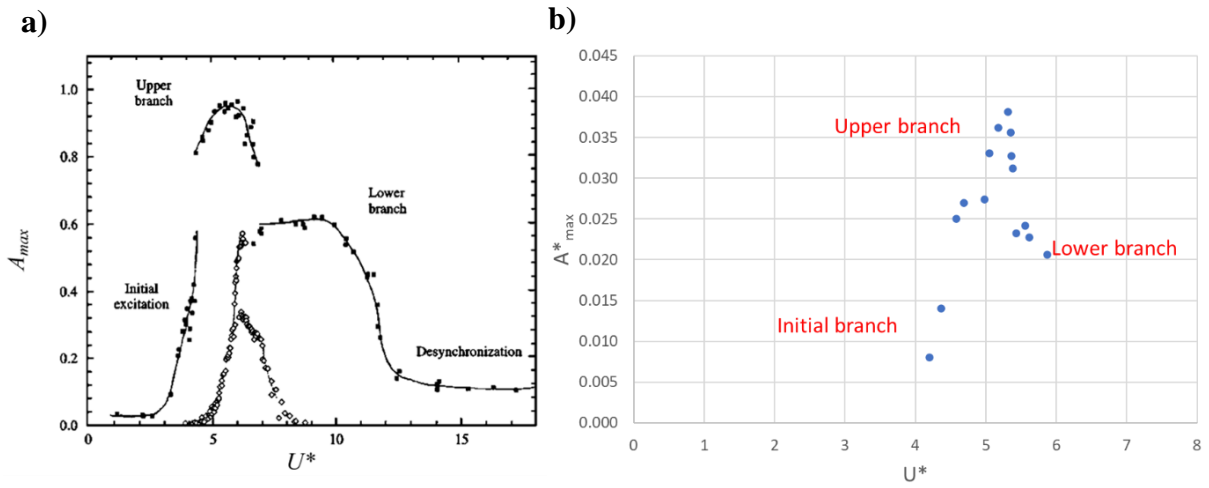


Figure 4.20. Free vibration response of the elastically mounted cylinder. The maximum displacement is plotted against the velocity ratio. a) data presented by Williamson and Govardhan (2004). b) the data acquired in the present study.

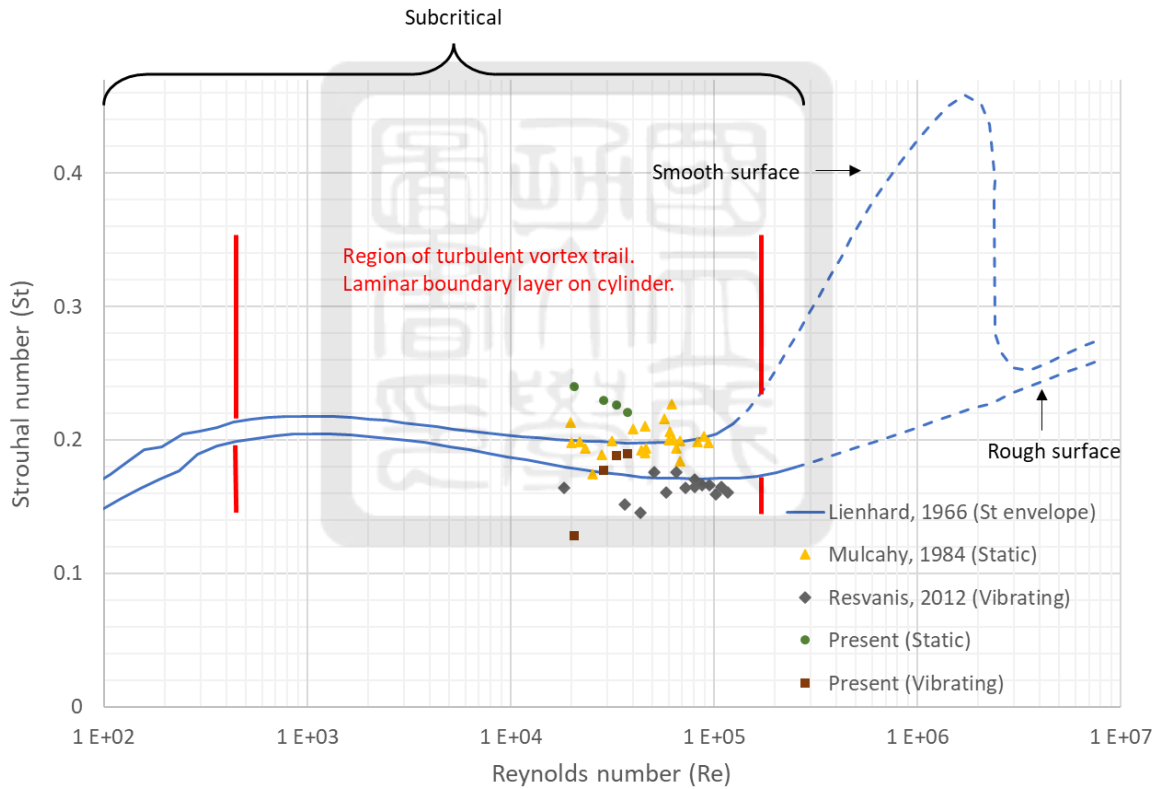


Figure 4.21. Strouhal number as a function of the Reynolds number. The blue line represent the Strouhal number envelope proposed by Lienhard (1966). Present results of static test are shown with green circles, while brown squares represent data from vibrating tests. Gray diamonds represent data of vibrating experiments from literature. Yellow triangles show data of static experiments from literature.

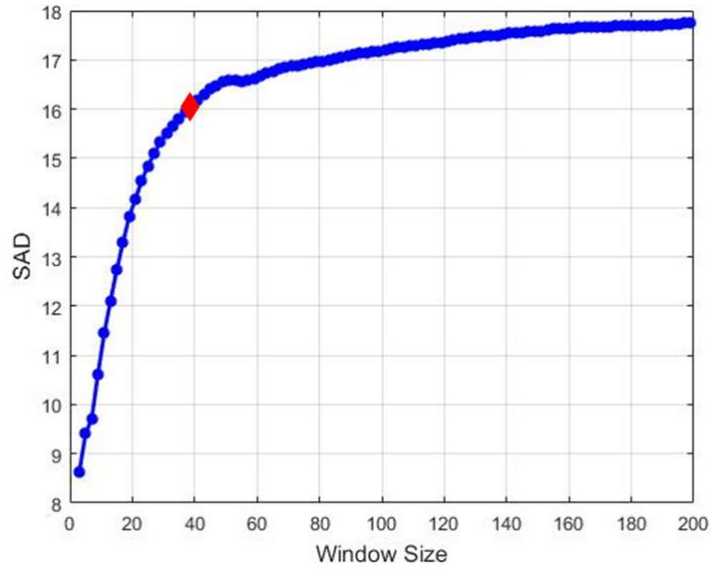
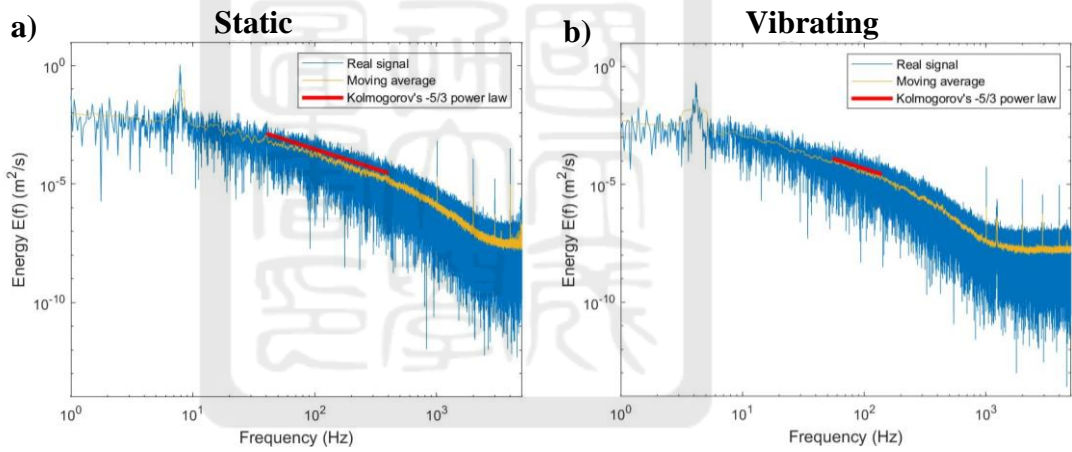
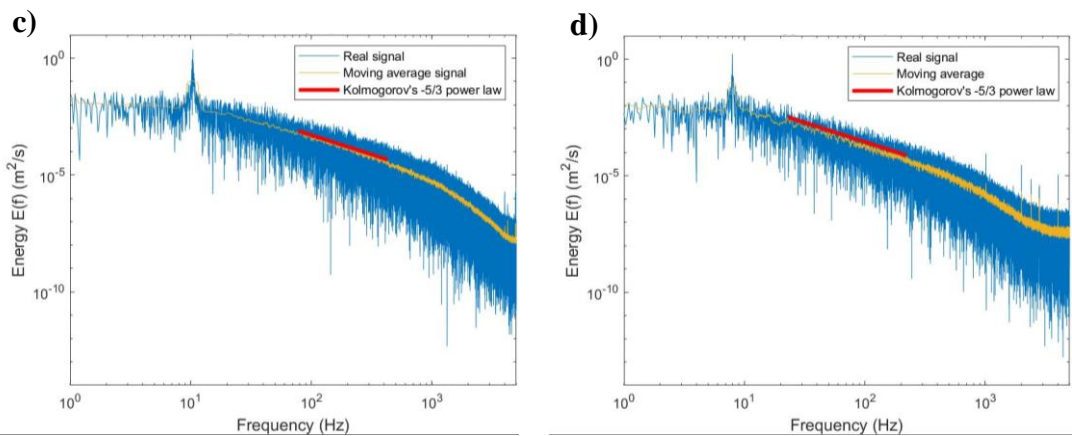


Figure 4.22. Plot of sum of absolute differences for different window sizes of static case,  $U^*=3.3$ ; collected at point  $(x/D, y/D) = (4, 1)$ . The size utilized is that at which the SAD is greater than 90% of the asymptotic value. In this case the moving average size is 39, highlighted in red.

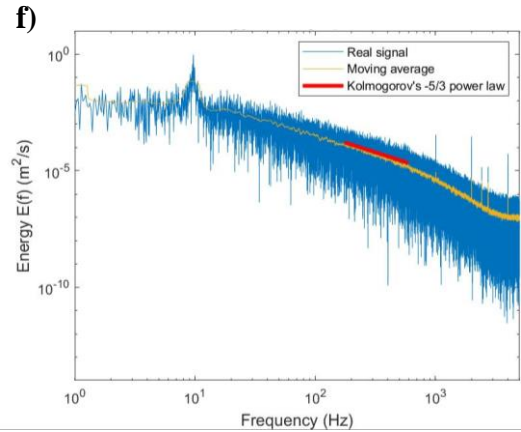
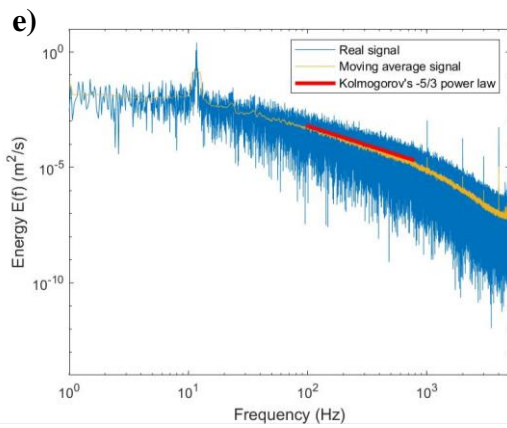
$U^* = 3.3$



$U^* = 4.6$



$U^* = 5.3$



$U^* = 6$

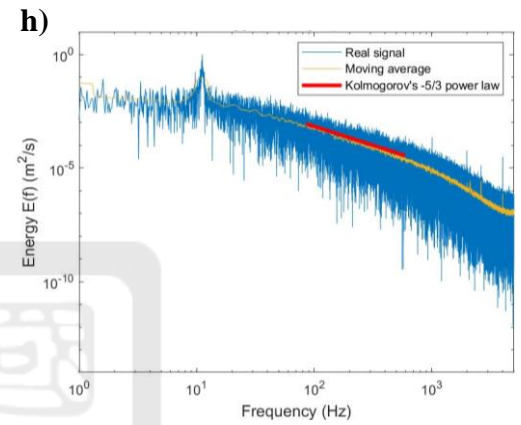
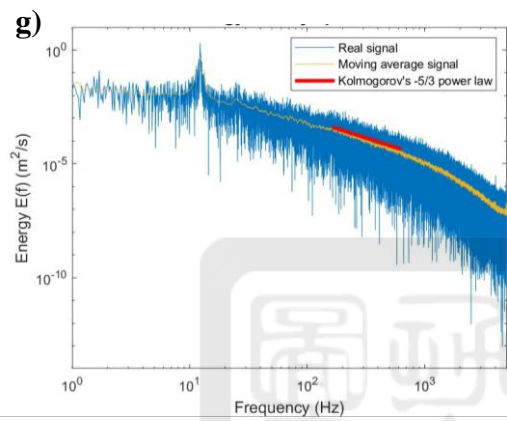


Figure 4.23. Turbulence energy spectra density of each case tested. The actual energy density is represented in blue. The smoothed signal (by moving average) is depicted in yellow. The red line, which has a slope of  $-5/3$ , indicates the approximate inertial range. Figures a), c), e) and g) are results of the static case. Figures b), d), f), and h) are results of the vibrating case. Results of velocity ratios  $U^* = 3.3, 4.6, 5.3,$  and  $6$ , are shown in Figures a) and b), c) and d), e) and f), g) and h), respectively. \*All results were obtained at point  $(x/D, y/D) = (4, 1)$ .

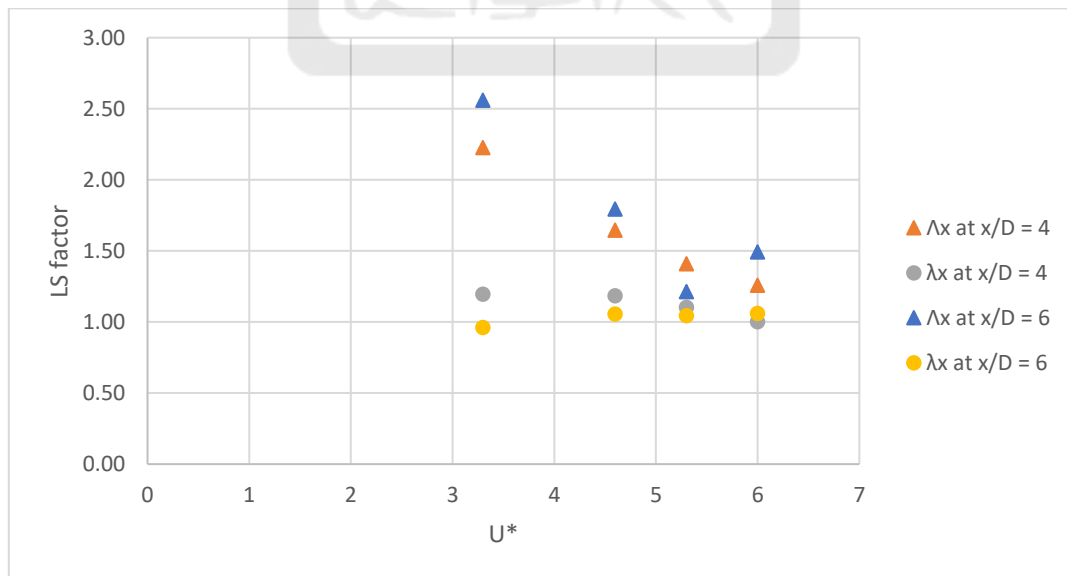


Figure 4.24. Length scale factors of  $\Lambda_x$  and  $\lambda_x$  at stations  $x/D = 4$  and  $6$ . (Refer to Equation (4.9)).

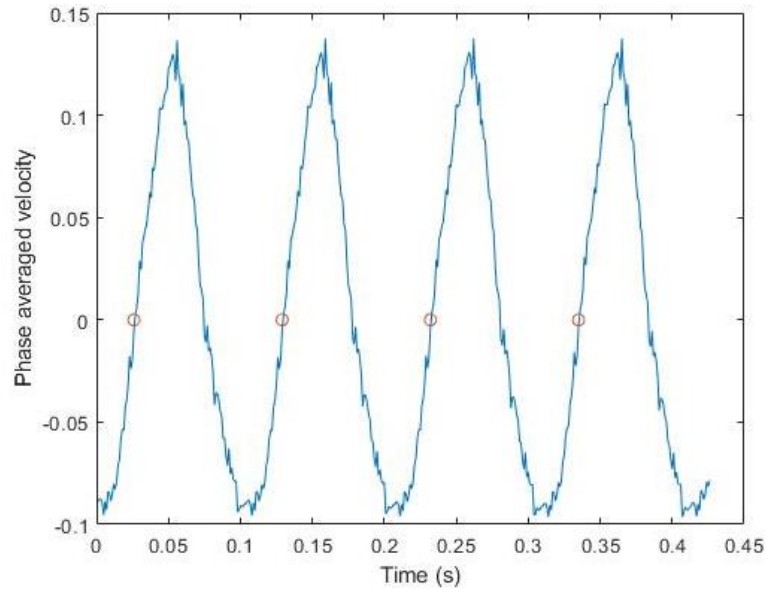
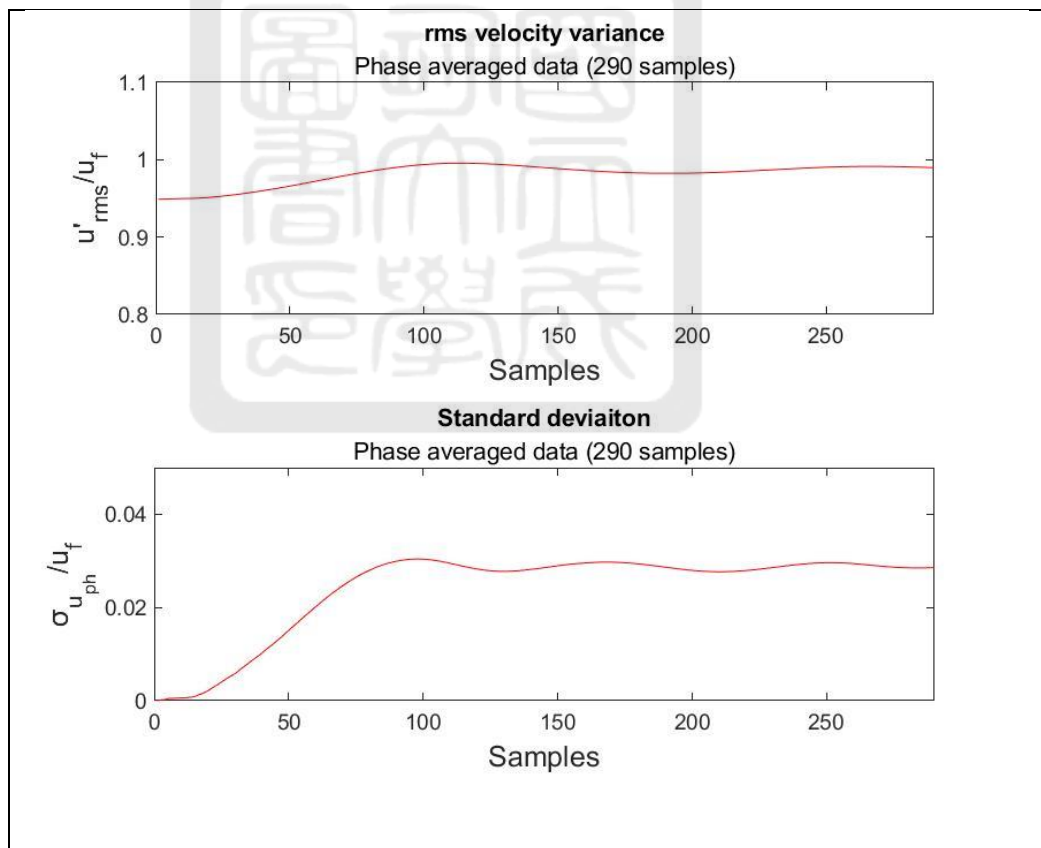


Figure 4.25. The phase average wave data (minus its average) and its zero-up-crossing index of vibrating case  $U^*=5.3$ . Each circle can represent the zero phase ( $t_p / T = 0$ ).

a)

$U^* = 3.3$



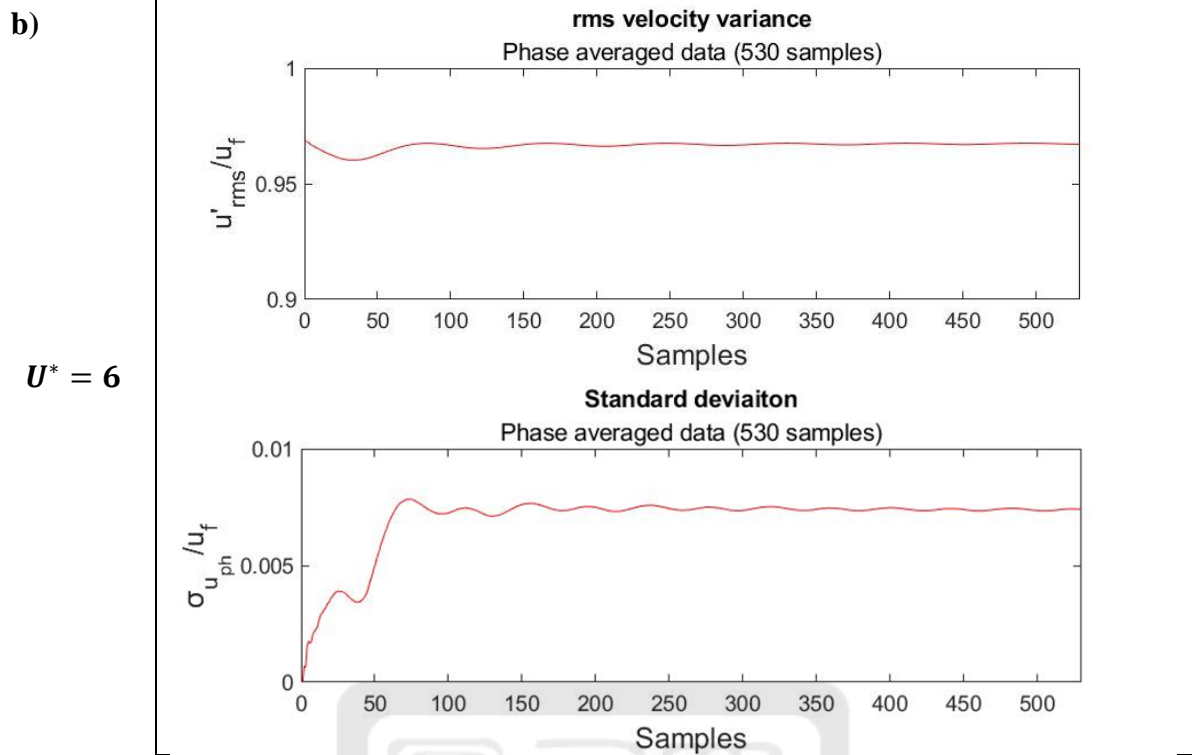
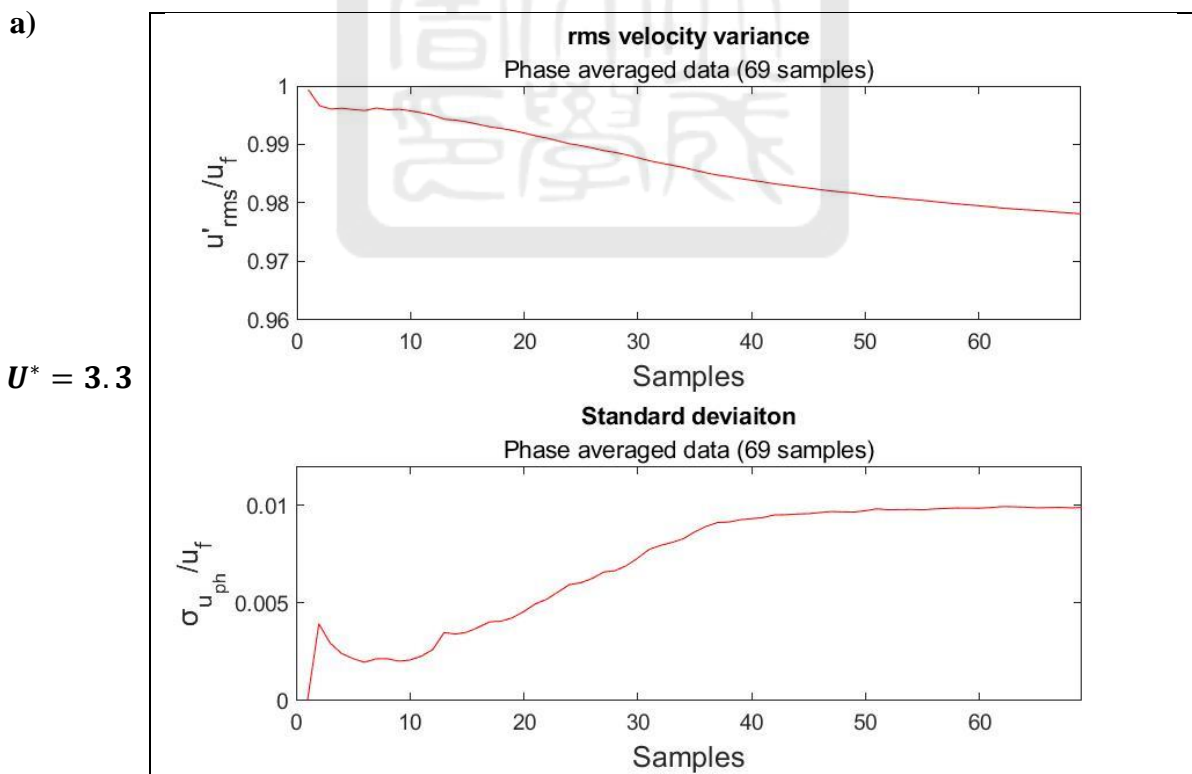


Figure 4.26. Root-mean-square variance and standard deviation of phase-averaged data for vibrating tests measured at point  $(x/D, y/D) = (4, 2)$ . a) are results of  $U^* = 3.3$ , and b) are results of  $U^* = 6$ .



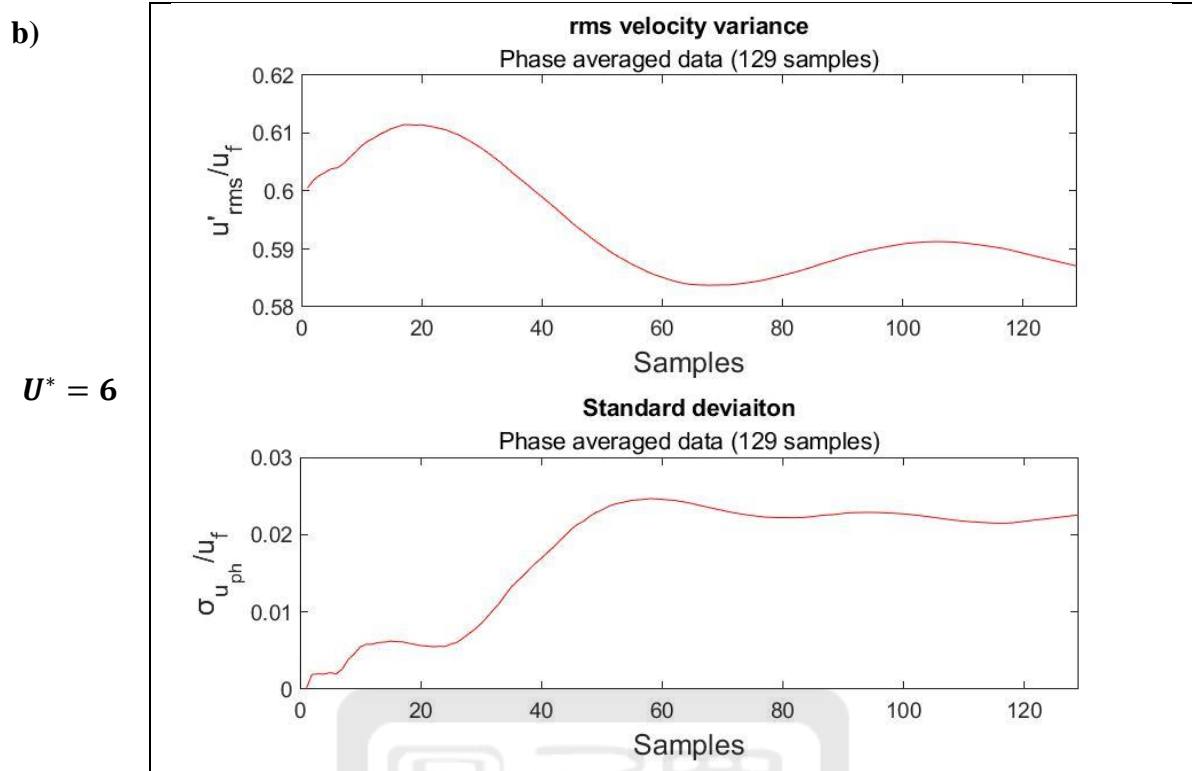
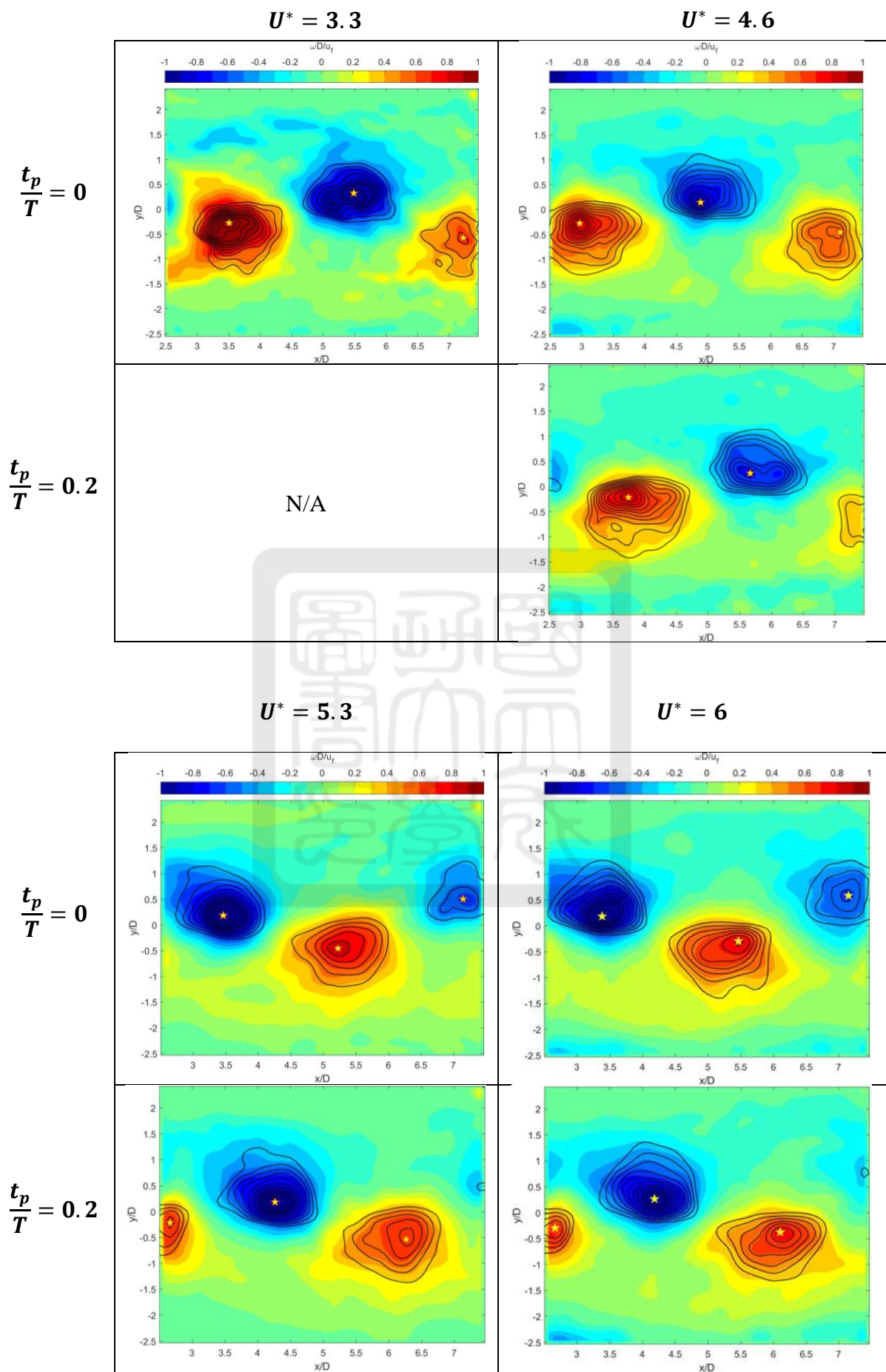


Figure 4.27. Root-mean-square variance and standard deviation of phase-averaged data for static tests measured at point  $(x/D, y/D) = (4,2)$ . a) are results of  $U^* = 3.3$ , and b) are results of  $U^* = 6$ .



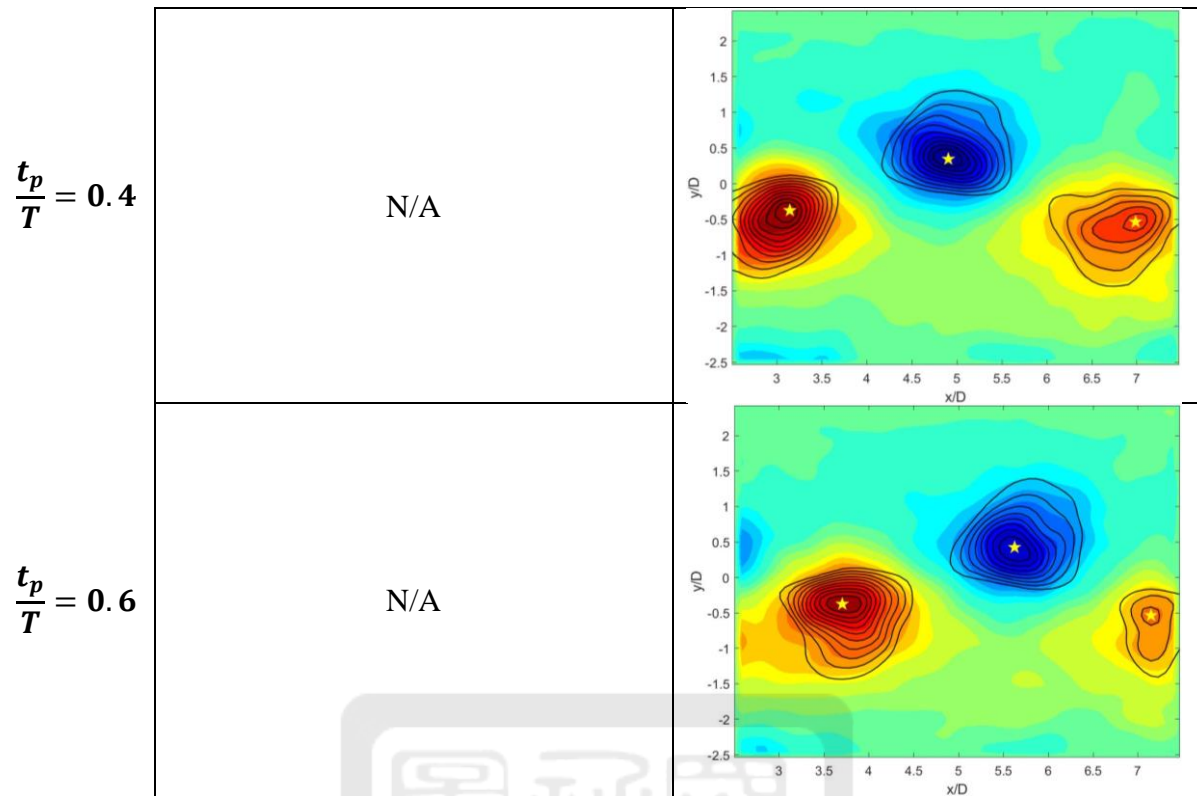
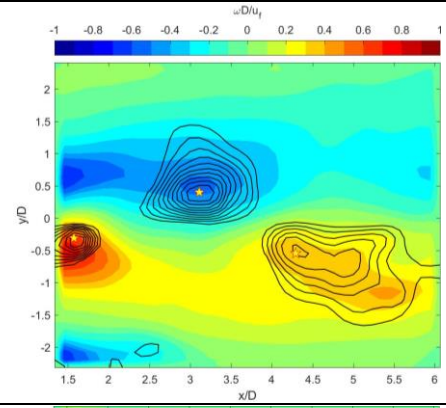
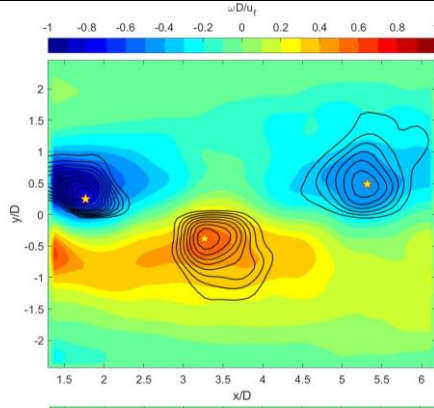


Figure 4.28. Phase-averaged normalized vorticity contour and vortex contour lines by Q criterion for static tests at different phases  $t_p/T$ . Yellow star denotes the vortex center (the maximum Q value).

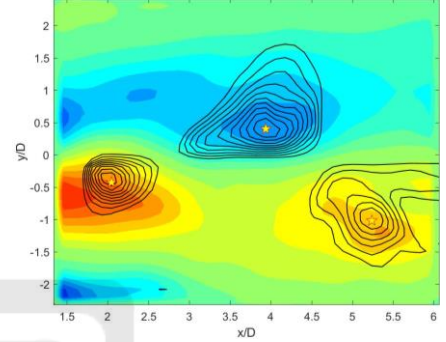
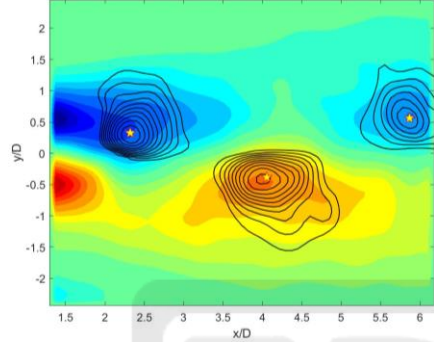
$U^* = 3.3$

$U^* = 4.6$

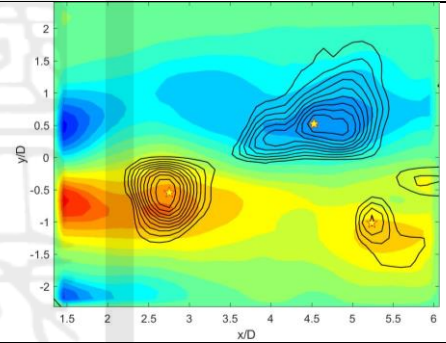
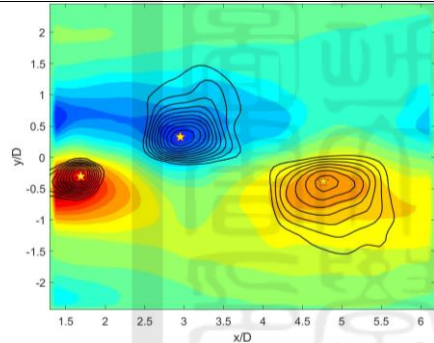
$\frac{t_p}{T} = 0$



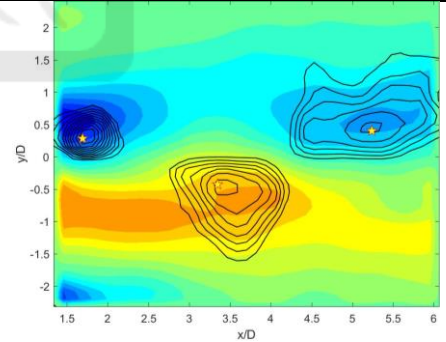
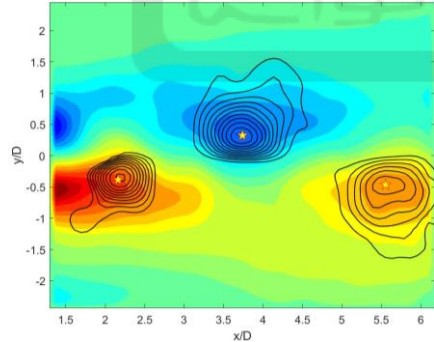
$\frac{t_p}{T} = 0.2$



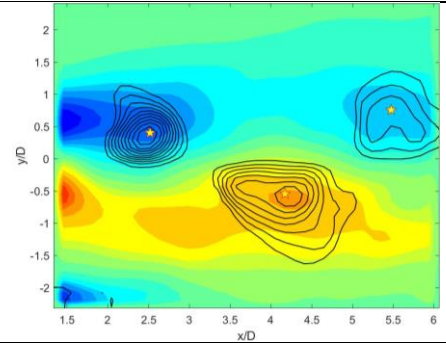
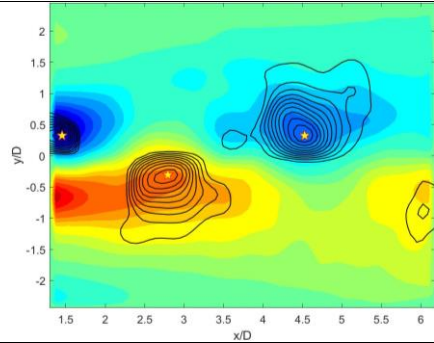
$\frac{t_p}{T} = 0.4$



$\frac{t_p}{T} = 0.6$



$\frac{t_p}{T} = 0.8$



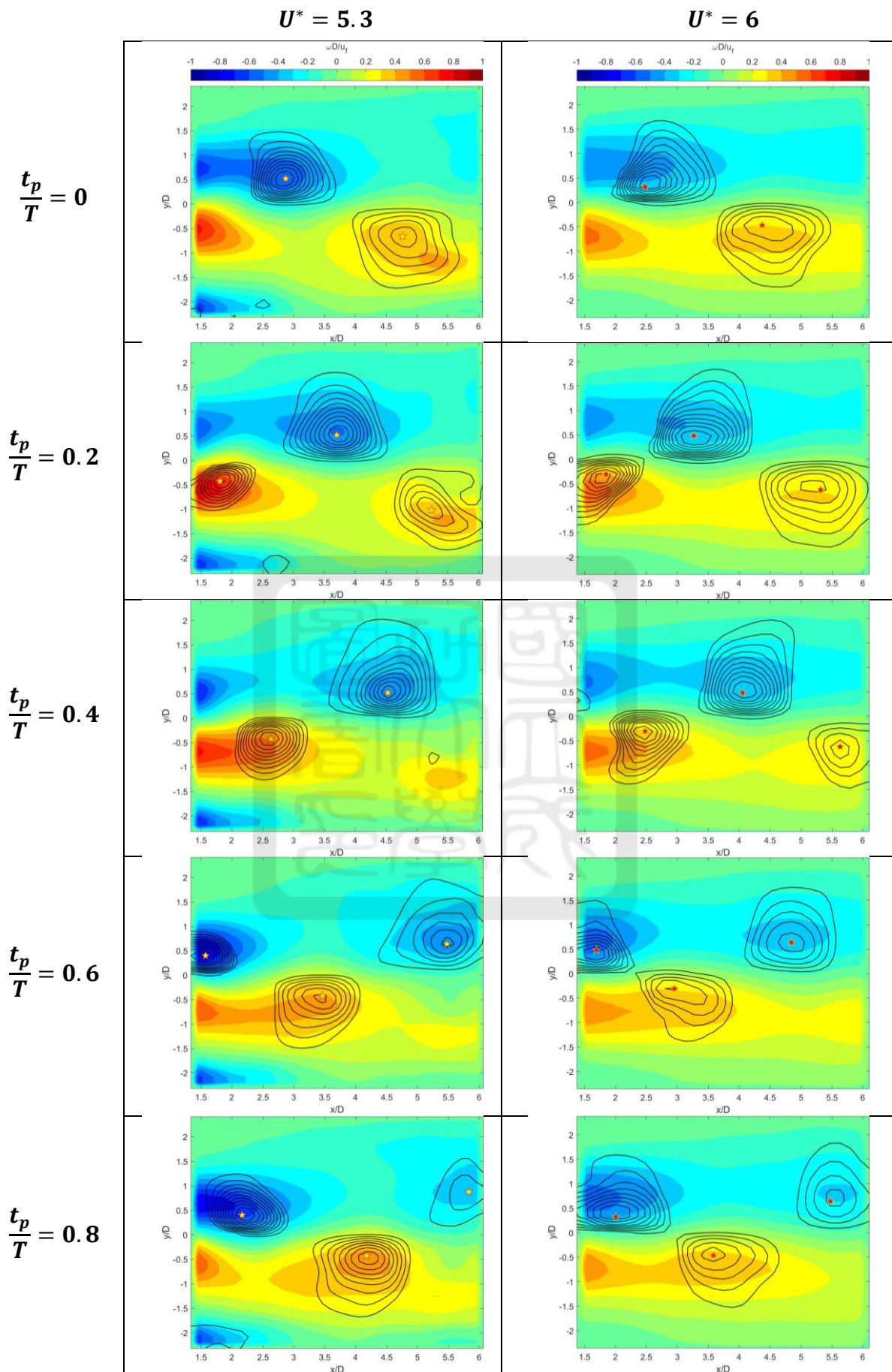


Figure 4.29. Phase-averaged normalized vorticity contour and vortex contour lines by Q criterion for vibrating tests at different phases  $t_p/T$ . Yellow (or red) star denotes the vortex center (the maximum Q value).

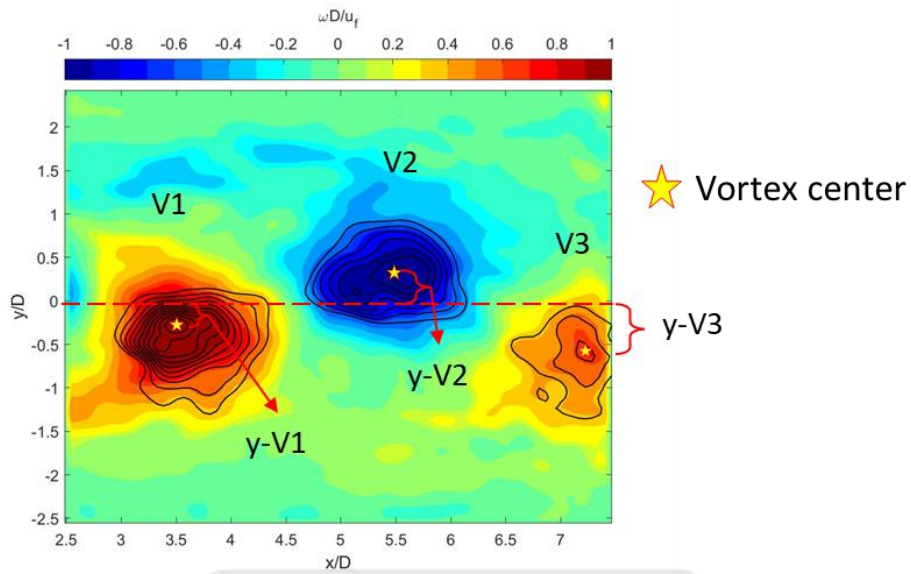


Figure 4.30. Distance from vortex center (depicted with a yellow star) to x-axis ( $y/D=0$ ). Labeled for each vortex, from left to right, as  $y-V1$ ,  $y-V2$ ,  $y-V3$ .

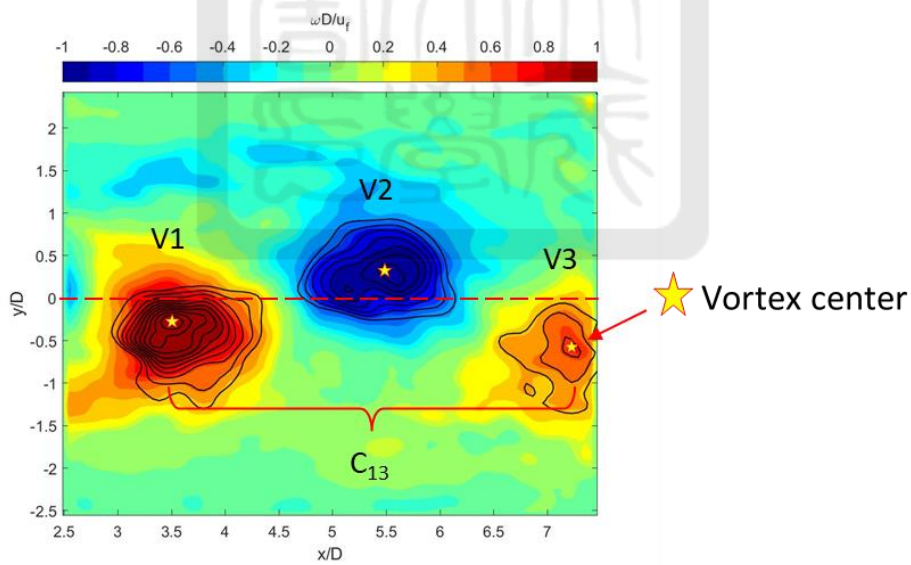
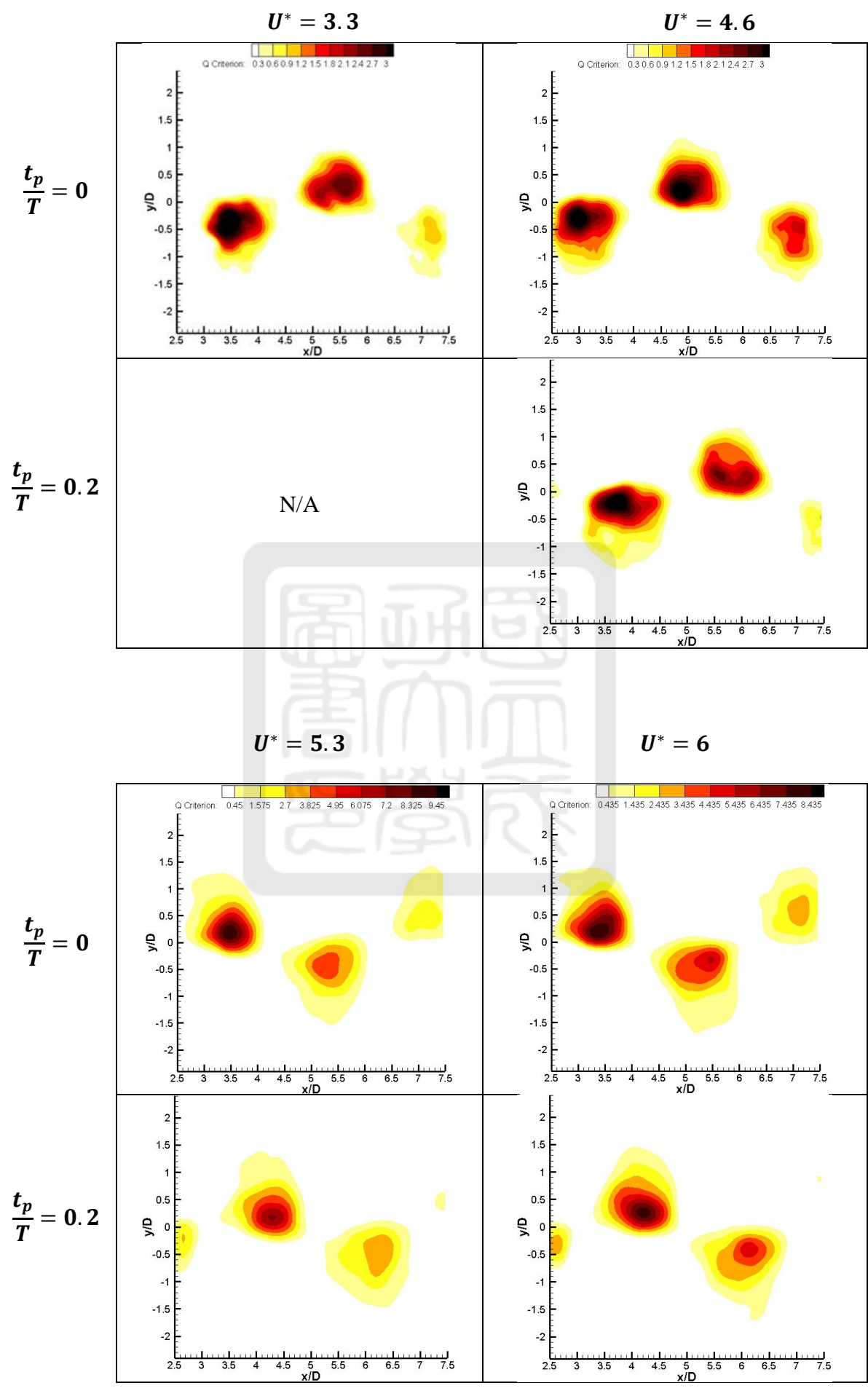


Figure 4.31. Distance between center of vortex 1 (V1) and vortex 3 (V3), defined as  $C_{13}$ .



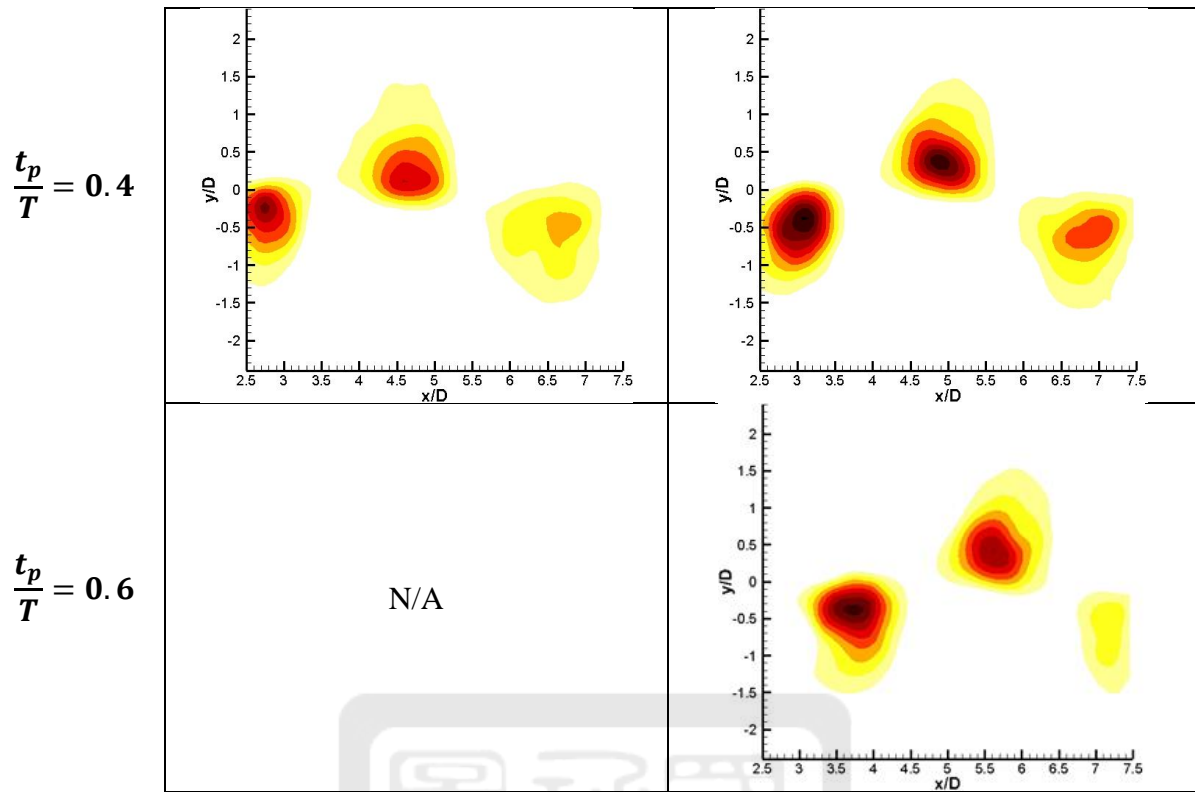
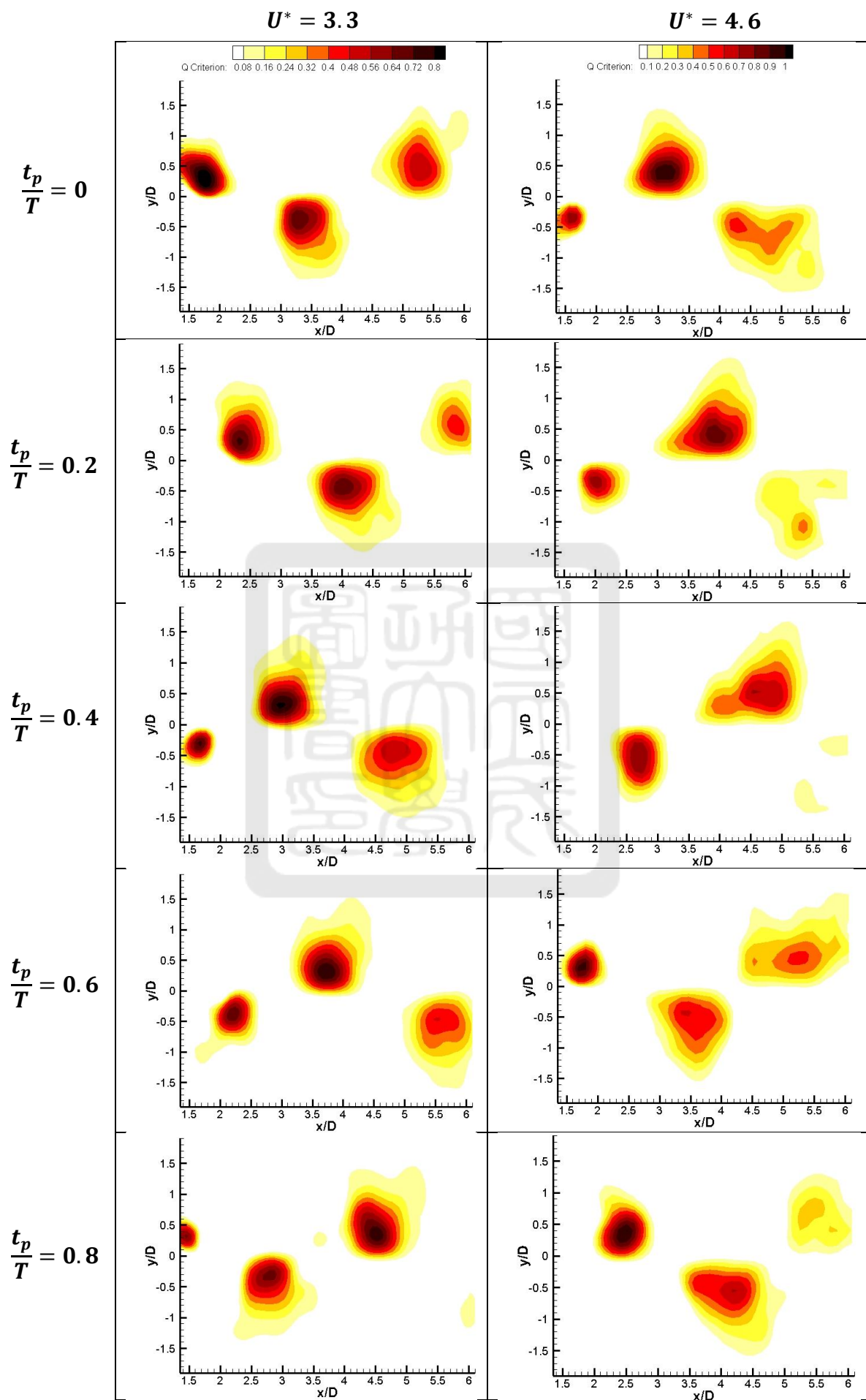


Figure 4.32. Phase-averaged vortex strength contour by Q criterion for static tests at different phases  $t_p/T$ .



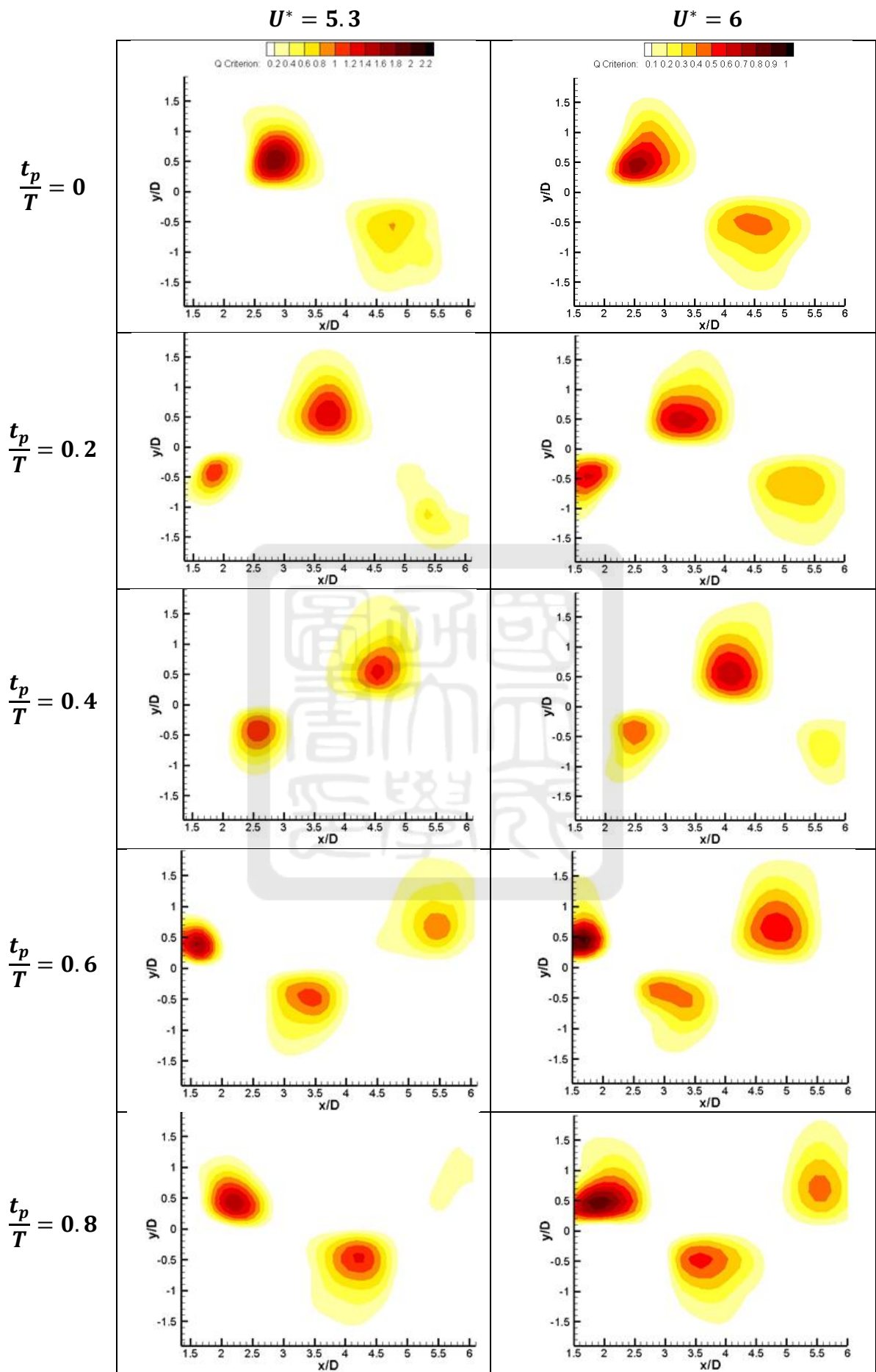


Figure 4.33. Phase-averaged vortex strength contour by Q criterion for vibrating tests at different phases  $t_p/T$ .

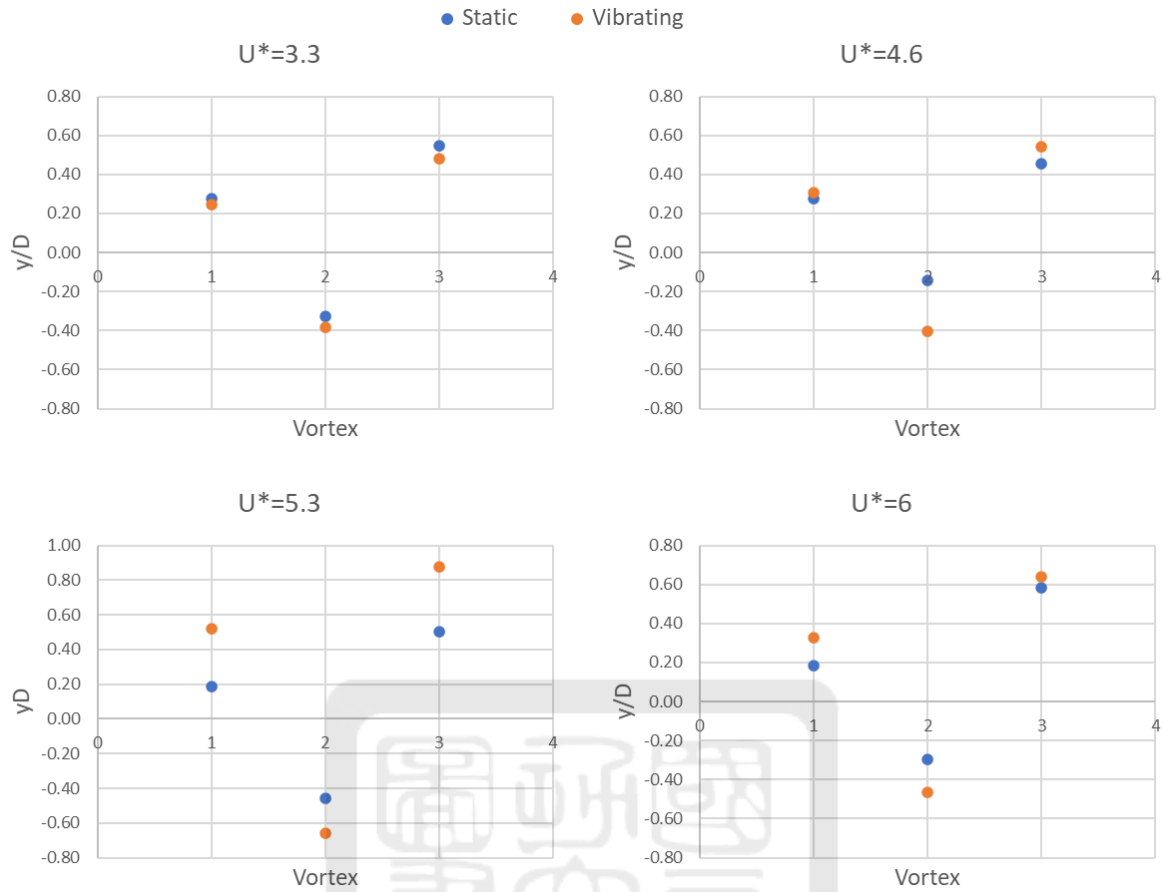


Figure 4.34. Comparison of vortex center locations ( $y$ -V1,  $y$ -V2 and  $y$ -V3) at phase  $t_p/T = 0$  between static and vibrating case for  $U^* = 3.3, 4.6, 5.3$  and  $6$ .

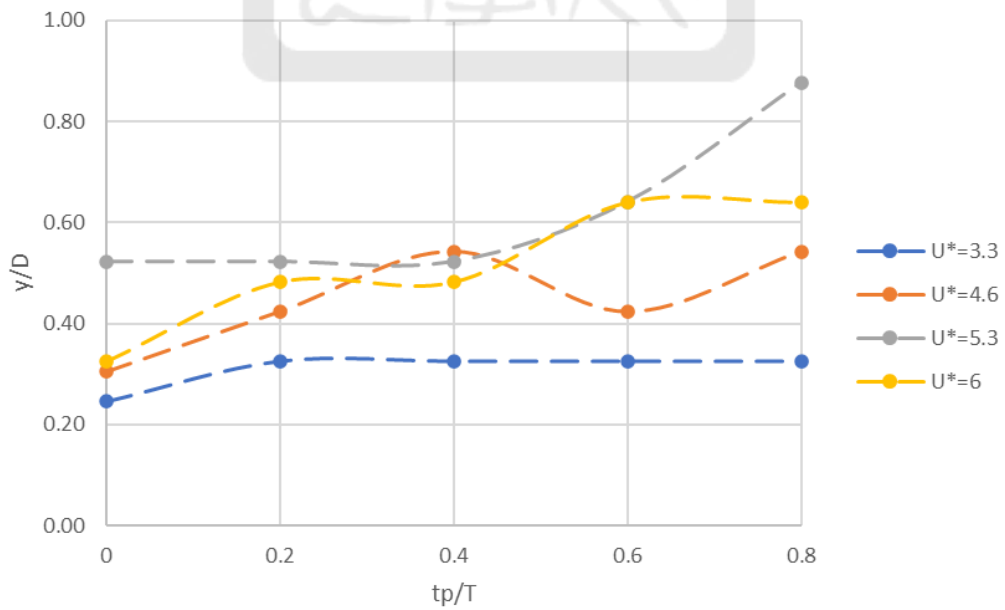


Figure 4.35. Comparison of the path of a specific vortex center (starting with  $y$ -V1 at phase  $t_p/T = 0$ ) through all phases, between  $U^* = 3.3, 4.6, 5.3$  and  $6$  for vibrating case. \*Note that the same vortex center becomes  $y$ -V3 at phase  $t_p/T = 8$ .

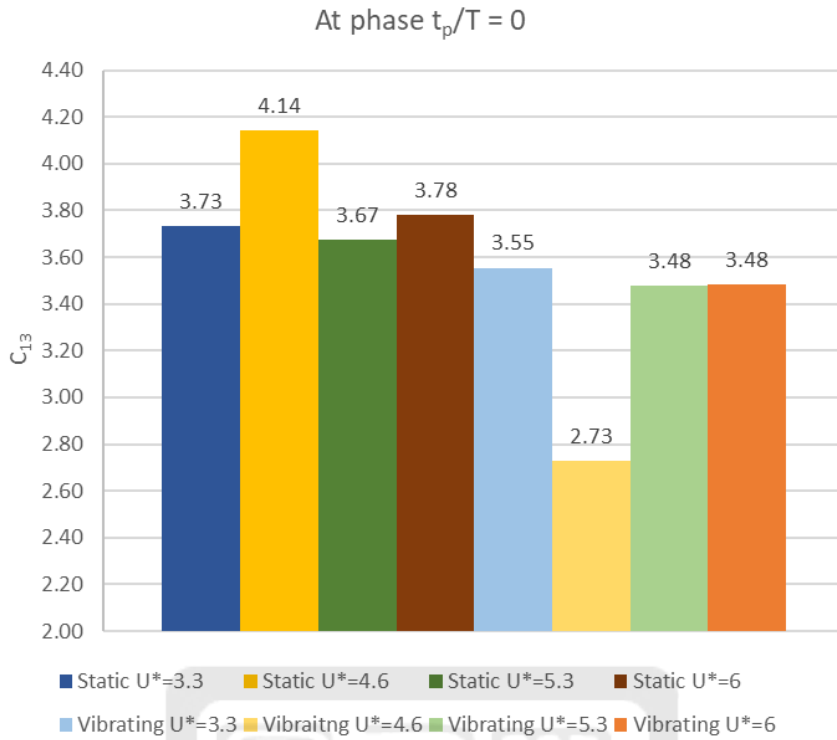


Figure 4.36. Comparison of the vortex center distances between V1 and V3 ( $C_{13}$ ) at  $t_p/T = 0$  between static and vibrating cases for  $U^* = 3.3, 4.6, 5.3$  and  $6$ .

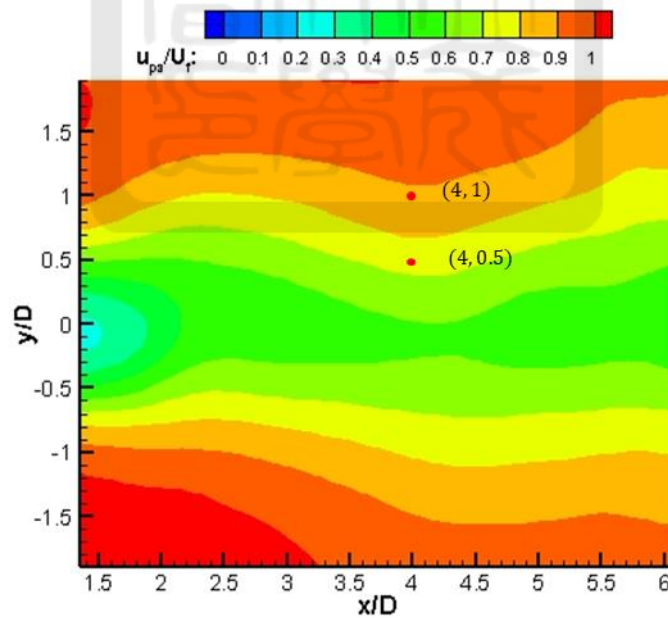


Figure 4.37. Phase-averaged velocity contour of case  $U^* = 6$  at  $t_p/T = 0$ . Red dots depict the two positions selected,  $(x/D, y/D) = (4, 0.5)$  and  $(4, 1)$ , to perform the decomposition of the phase-averaged velocities.

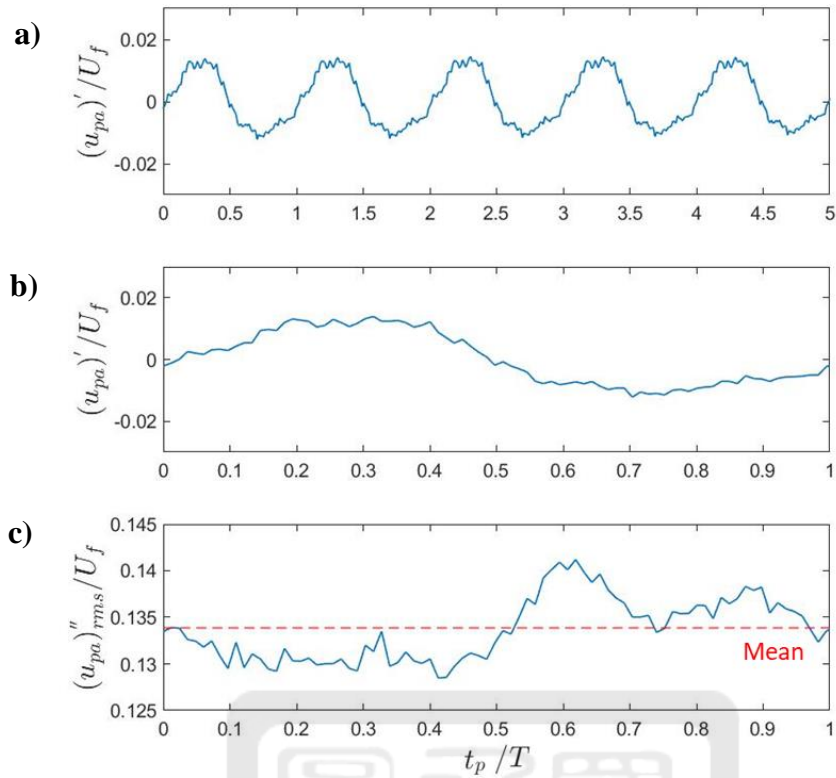


Figure 4.38. a) Phase-averaged velocity fluctuation during five periods ( $t_p/T = 5$ ). b) Phase-averaged velocity fluctuation within one arbitrary period ( $t_p/T = 1$ ). c) Root-mean-square of the “real fluctuating” velocity ( $t_p/T = 1$ ). \*Each term is computed at  $(x/D, y/D) = (4, 0.5)$  for the case of  $U^* = 6$  and normalized with  $U_f$ .

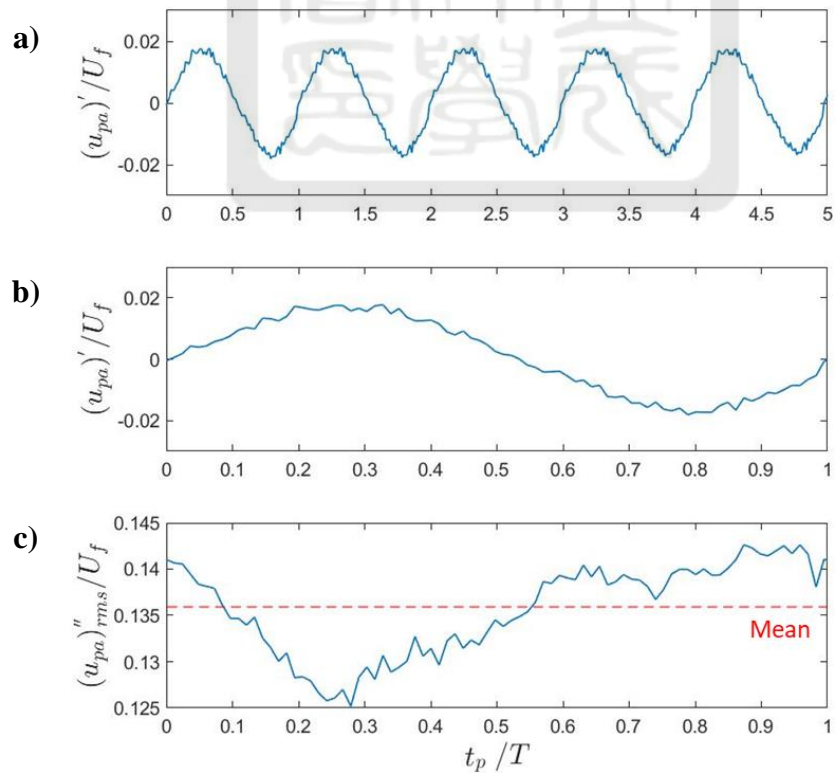


Figure 4.39. a) Phase-averaged velocity fluctuation during five periods ( $t_p/T = 5$ ). b) Phase-averaged velocity fluctuation within one arbitrary period ( $t_p/T = 1$ ). c) Root-mean-square of the “real fluctuating” velocity ( $t_p/T = 1$ ). \*Each term is computed at  $(x/D, y/D) = (4, 1)$  for the case of  $U^* = 6$  and normalized with  $U_f$ .

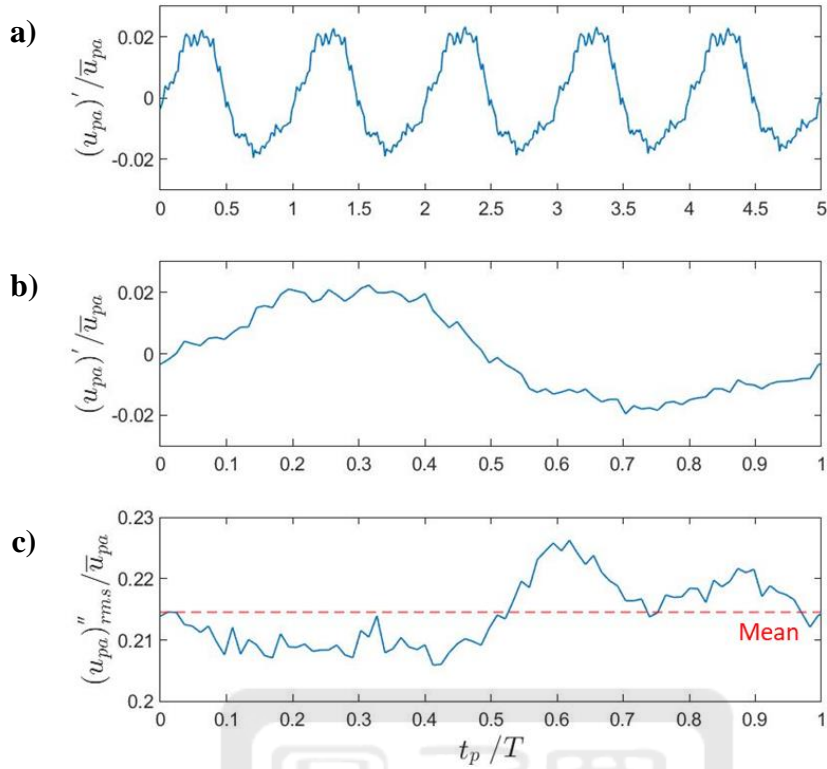


Figure 4.40. a) Phase-averaged velocity fluctuation during five periods ( $t_p/T = 5$ ). b) Phase-averaged velocity fluctuation within one arbitrary period ( $t_p/T = 1$ ). c) Root-mean-square of the "real fluctuating" velocity ( $t_p/T = 1$ ). \*Each term is computed at  $(x/D, y/D) = (4, 0.5)$  for the case of  $U^* = 6$  and normalized with  $\bar{u}_{pa}$ .

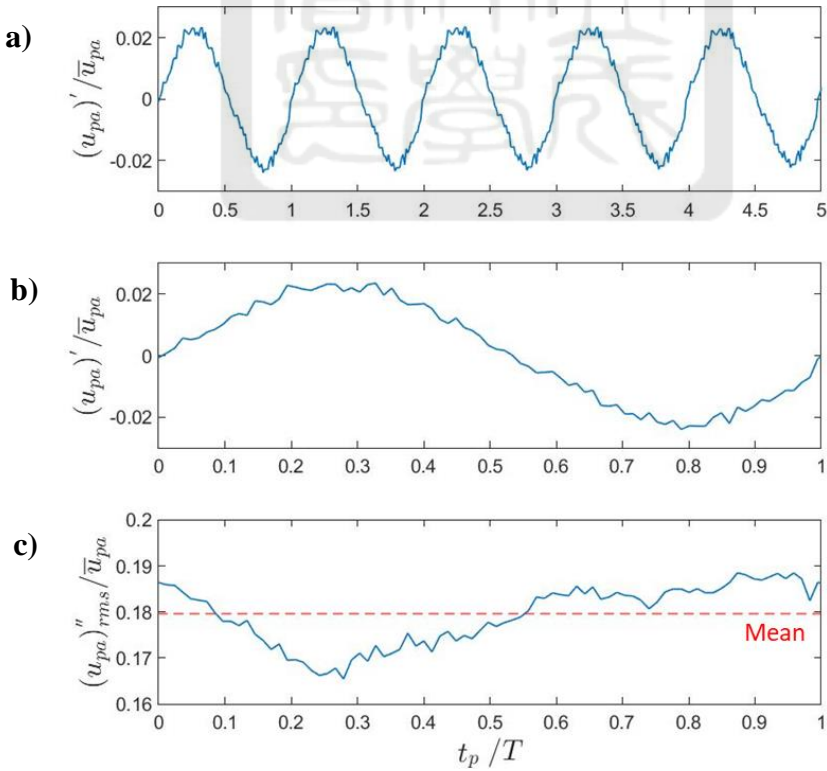
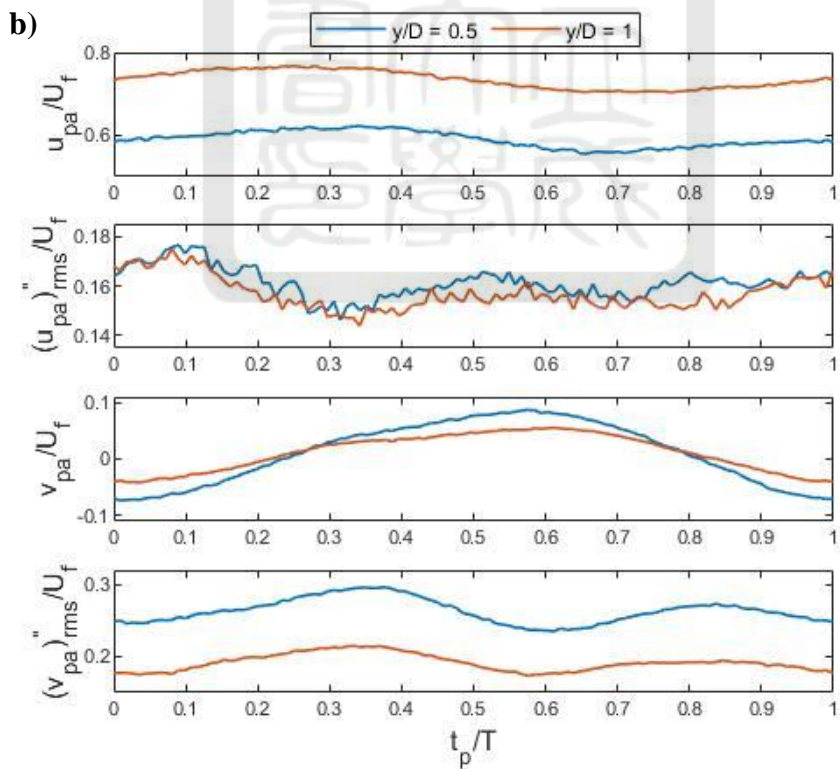
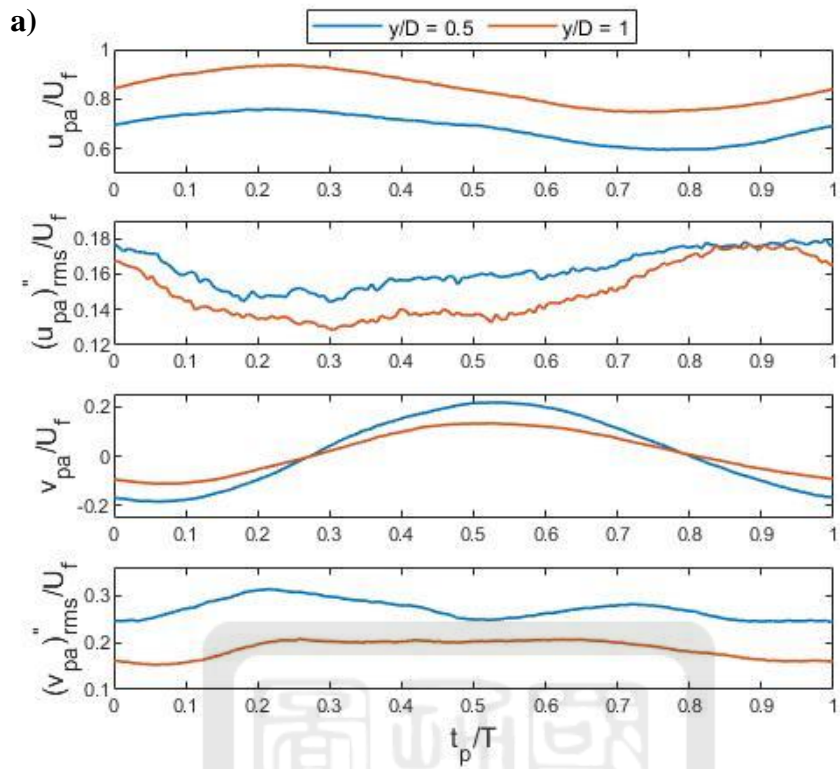


Figure 4.41. a) Phase-averaged velocity fluctuation during five periods ( $t_p/T = 5$ ). b) Phase-averaged velocity fluctuation within one arbitrary period ( $t_p/T = 1$ ). c) Root-mean-square of the "real fluctuating" velocity ( $t_p/T = 1$ ). \*Each term is computed at  $(x/D, y/D) = (4, 1)$  for the case of  $U^* = 6$  and normalized with  $\bar{u}_{pa}$ .



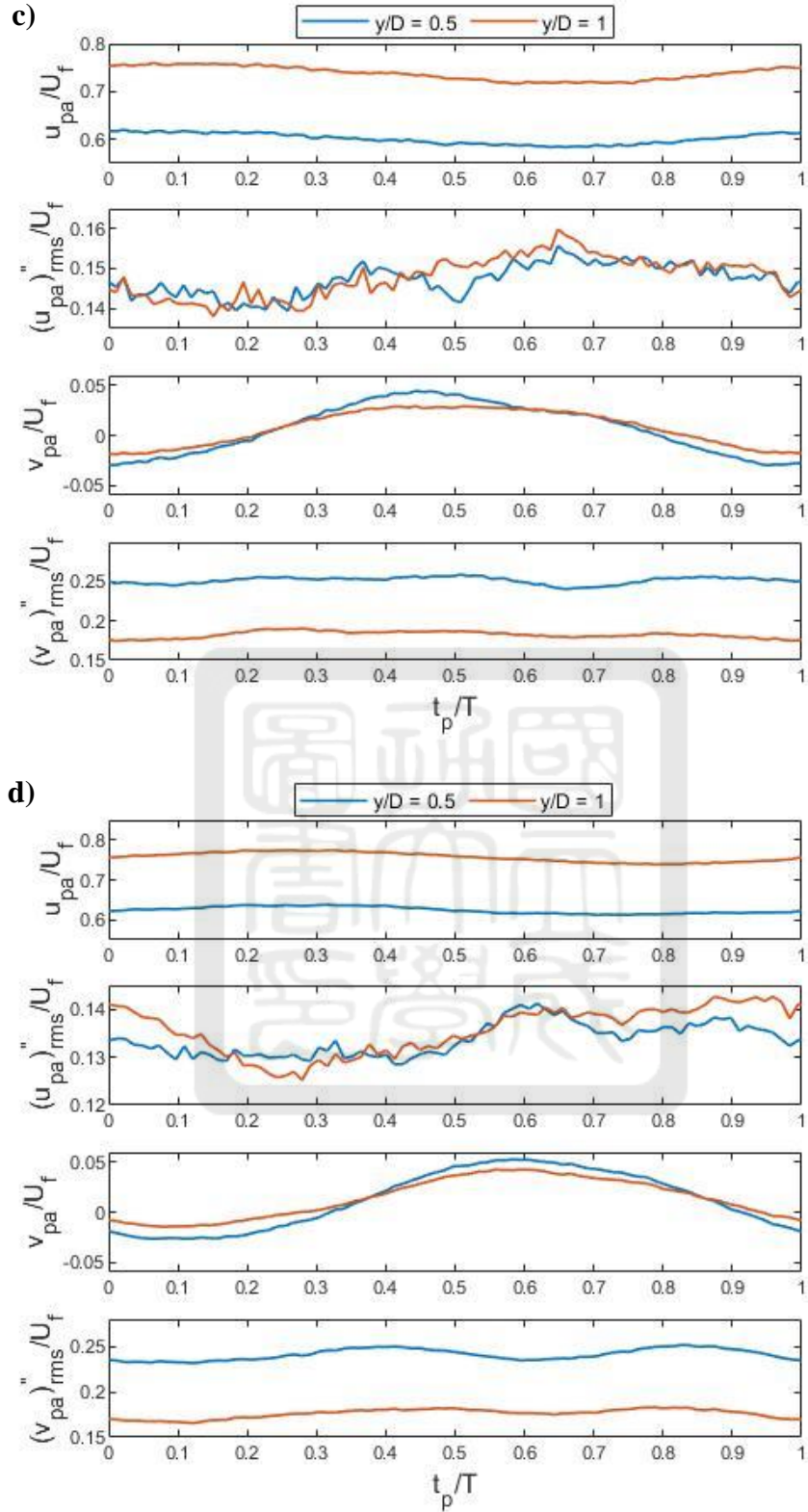


Figure 4.42. Time histories of the phase-averaged velocity, and root-mean-square of the phase-averaged fluctuating velocity measured at points  $(x/D, y/D) = (4, 0), (4, 0.5)$  and  $(4, 1)$  for a)  $U^* = 3.3$ , b)  $U^* = 4.6$ , c)  $U^* = 5.3$ , d)  $U^* = 6$ .

## Chapter 5 – Conclusions

### 5.1 Concluding remarks

The vortex structure in the wake of a freely vibrating circular cylinder, as well as its turbulence statistics, were studied and compared with that of a stationary circular cylinder using PIV and HWA systems. Its oscillation amplitude was also examined utilizing laser displacement sensors. Emphasis was made on the visualization of vortices and the understanding of their behaviors during the lock-in range (corresponding to the initial branch, upper branch, and lower branch) by identifying the vortex center and comparing each different case. To make sure the reliability of PIV measurements, the first order statistics of a static cylinder were analyzed and compared using both PIV and HWA. Results showed that statistically stationary results can be attained.

Vortices cannot be accurately detected by the vorticity contour merely, thus the  $Q$ -criterion was used to identify the vortices and their centers. To achieve a more precise visualization of the vorticity and vortex contours, the phase average technique was applied to the experimental data collected, and different phases were inspected. As the cylinder oscillates, the relative velocity between the freestream and the vibrating cylinder is altered, causing the vortex strength to be smaller than that of the static cylinder. Additionally, as may be expected, the vorticity and vortex strength are reduced as the fluid moves farther downstream.

At the resonance velocity, the vortex shedding frequency matches the natural frequency of structure, showing only one main peak in the power spectrum. At other velocities, these frequencies do not match, and the power spectrum shows two peaks. When at resonance, the displacement of the vibrating cylinder is the largest. Because of this displacement, the size of the affected wake zone at the stations examined ( $x/D = 4$  and  $6$ ) is much wider for the vibrating case compared to the static case. This was further corroborated by detecting the center of the vortices and measuring their distance from the centerline ( $x$ -axis); showing that the

vortices are farther away from the centerline when the system is at resonance. Another interesting finding is that, even though vortex shedding frequencies are larger for the static case, the distance between two consecutive vortices in the near wake region is larger. Also, at these stations the large-scale eddies are still increasing in size. On the other hand, the size of the smaller eddies, belonging to the inertial subrange, remain relatively constant and are independent of structural vibrations. This suggests that the vortices are still growing, and the flow has not reached its fully developed state.

In addition, the small-scale turbulence characteristics can be obtained from PIV measurements by means of the phase-average technique. The phase-averaged velocity can be decomposed into a mean and a fluctuating component; the fluctuating component can be further decomposed to determine the “real fluctuating” velocity. Results indicate that the velocity fluctuations are still a function of time ( $t_p/T$ ) in each period.

## 5.2 Future prospect

There exist many different approaches to visualize a flow field and to examine its characteristics. The phase average technique and vortex detection by  $Q$ -criterion, adopted in this study, is just one of them. Other analysis techniques can be applied to the data collected to investigate different characteristics of the wake flow of a circular cylinder during VIV. For instance, proper orthogonal decomposition (POD) can be applied to decompose the flow into several components (modes) and investigate their energy distribution.

In addition, a better comparison of the vortical structures between static and vibrating cases can be made by performing again static tests and increasing the number of frames of images acquired, in order to achieve the visualization of all phases within a vortex shedding period. Also, the turbulence characteristics can be measured with HWA by increasing the number of samples captured.

## REFERENCES

- Adrian, R. (1991). Particle-imaging techniques for experimental fluid-mechanics. *Annual Review of Fluid Mechanics*, 23, 261-304.  
<https://doi.org/10.1146/annurev.fluid.23.1.261>
- Bearman, P. W. (1965). Investigation of the flow behind a two-dimensional model with a blunt trailing edge and fitted with splitter plates. *Journal of Fluid Mechanics*, 21(2), 241-255. <https://doi.org/10.1017/S0022112065000162>
- Bearman, P. W. (1969). On vortex shedding from a circular cylinder in the critical Reynolds number régime. *Journal of Fluid Mechanics*, 37(3), 577-585.  
<https://doi.org/10.1017/S0022112069000735>
- Bearman, P. W. (1984). Vortex shedding from oscillating bluff bodies. *Annual Review of Fluid Mechanics*, 16(1), 195-222.  
<https://doi.org/10.1146/annurev.fl.16.010184.001211>
- Belloli, M., Giappino, S., Morganti, S., Muggiasca, S., & Zasso, A. (2015). Vortex Induced Vibrations at High Reynolds Numbers on Circular Cylinders. *Ocean Engineering*, 94, 140-154. <https://doi.org/10.1016/j.oceaneng.2014.11.017>
- Bendat, J. S., & Piersol, A. G. (2011). *Random data: Analysis and measurement procedures*. Wiley. <https://books.google.com.tw/books?id=qYSViFRNMLwC>
- Bevington, P. R., Robinson, D. K., Blair, J. M., Mallinckrodt, A. J., & McKay, S. (1993). Data reduction and error analysis for the physical sciences. *Computers in Physics*, 7(4), 415-416. <https://doi.org/10.1063/1.4823194>
- Blevins, R. (1990). *Flow-induced vibration* (2nd ed.). Van Nostrand Reinhold.
- Boillot, A., & Prasad, A. K. (1996). Optimization Procedure for Pulse Separation in Cross-Correlation PIV. *Experiments in Fluids*, 21(2), 87-93.  
<https://doi.org/10.1007/BF00193911>
- Brennen, C. E. (2006). *An internet book on fluid dynamics*  
<http://brennen.caltech.edu/fluidbook/Fluidbook.htm>
- Carlier, J., & Stanislas, M. (2005). Experimental study of eddy structures in a turbulent boundary layer using particle image velocimetry. *Journal of Fluid Mechanics*, 535, 143-188. <https://doi.org/10.1017/S0022112005004751>
- Chen, W.-C., & Chang, K.-C. (2018). PIV measurements in near-wake turbulent regions. *Modern Physics Letters B*, 32, 1840026. <https://doi.org/10.1142/S0217984918400262>
- Comte-Bellot, G. (1976). Hot-wire anemometry. *Annual Review of Fluid Mechanics*, 8(1), 209-231.
- Crowe, C. T., Troutt, T. R., and, & Chung, J. N. (1996). Numerical models for two-phase turbulent flows. *Annual Review of Fluid Mechanics*, 28(1), 11-43.  
<https://doi.org/10.1146/annurev.fl.28.010196.000303>
- Druck DPI 610/615 IS: User manual K0430. (2008). (2).
- Ekman, P. (2020). *Important factors for accurate scale-resolving simulations of automotive aerodynamics* (Publication Number 2068) [Doctoral thesis, comprehensive summary, Linköping University Electronic Press]. DiVA. Linköping.  
<https://doi.org/10.3384/diss.diva-164926>

- El-Gabry, L. A., Thurman, D. R., & Poinsette, P. E. (2014). Procedure for Determining Turbulence Length Scales Using Hotwire Anemometry.
- Feng, C. C. (1968). The measurement of vortex induced effects in flow past stationary and oscillating circular and D-section cylinders.
- Friedman, A. (1997). Aeroacoustic research in the automotive industry. In *Mathematics in Industrial Problems: Part 8* (pp. 154-168). Springer New York.  
[https://doi.org/10.1007/978-1-4612-1858-6\\_17](https://doi.org/10.1007/978-1-4612-1858-6_17)
- Gere, J. M., & Goodno, B. J. (2012). *Mechanics of Materials, SI Edition*. Cengage Learning.  
<https://books.google.com.tw/books?id=RULohOkWRxUC>
- Gerrard, J. H. (1966). The mechanics of the formation region of vortices behind bluff bodies. *Journal of Fluid Mechanics*, 25(2), 401-413.  
<https://doi.org/10.1017/S0022112066001721>
- Gonzalez, R. C. (2002). *Digital image processing* (2 ed.). Prentice-Hall Of India Pvt. Limited. <https://books.google.com.tw/books?id=iyJOPgAACAAJ>
- Goswami, I., Scanlan, R. H., & Jones, N. P. (1993). Vortex-induced vibration of circular-cylinders . 1: Experimental-data. *Journal of Engineering Mechanics-Asce*, 119(11), 2270-2287. [https://doi.org/Doi 10.1061/\(Asce\)0733-9399\(1993\)119:11\(2270\)](https://doi.org/Doi%2010.1061/(Asce)0733-9399(1993)119:11(2270))
- Govardhan, R. N., & Williamson, C. H. K. (2006). Defining the ‘modified Griffin plot’ in vortex-induced vibration: Revealing the effect of Reynolds number using controlled damping. *Journal of Fluid Mechanics*, 561, 147-180.  
<https://doi.org/10.1017/S0022112006000310>
- Griffin, O. M. (1995). A note on bluff body vortex formation. *Journal of Fluid Mechanics*, 284, 217-224. <https://doi.org/10.1017/S0022112095000322>
- Haller, G. (2001). Response to “Comment on ‘Finding finite-time invariant manifolds in two-dimensional velocity fields’ ” † Chaos 11, 427 ,, 2001 ...‡. *Chaos (Woodbury, N.Y.)*, 11, 431-437. <https://doi.org/10.1063/1.1374242>
- Hsieh, S. C., Low, Y. M., & Chiew, Y. M. (2017). Flow characteristics around a circular cylinder undergoing vortex-induced vibration in the initial branch. *Ocean Engineering*, 129, 265-278. <https://doi.org/10.1016/j.oceaneng.2016.11.019>
- Hunt, J., Wray, A., & Moin, P. (1988). Eddies, streams, and convergence zones in turbulent flows. *Studying Turbulence Using Numerical Simulation Databases, -1*, 193-208.
- Jeong, J., & Hussain, F. (1995). Hussain, F.: On the identification of a vortex. JFM 285, 69-94. *Journal of Fluid Mechanics*, 285, 69-94.  
<https://doi.org/10.1017/S0022112095000462>
- Jorgensen, F. E. (2002). *How to measure turbulence with hot-wire anemometers: a practical guide*. Dantec Dynamics.
- Khalak, A., & Williamson, C. H. K. (1997). Investigation of relative effects of mass and damping in vortex-induced vibration of a circular cylinder. *Journal of Wind Engineering and Industrial Aerodynamics*, 69-71, 341-350.  
[https://doi.org/https://doi.org/10.1016/S0167-6105\(97\)00167-0](https://doi.org/https://doi.org/10.1016/S0167-6105(97)00167-0)
- Khalak, A., & Williamson, C. H. K. (1999). Motions, forces and mode transitions in vortex-induced vibrations at low mass-damping. *Journal of Fluids and Structures*, 13(7), 813-851. <https://doi.org/https://doi.org/10.1006/jfls.1999.0236>

- Koh, T.-Y., & Legras, B. (2002). Hyperbolic lines and the stratospheric polar vortex. *Chaos (Woodbury, N.Y.)*, 12, 382-394. <https://doi.org/10.1063/1.1480442>
- LabVIEW. (2021). *Version 21.0 (LabVIEW 2021)*. National Instruments.
- Lapeyre, G., Hua, B., & Legras, B. (2001). Comment on “Finding finite-time invariant manifolds in two-dimensional velocity fields” [Chaos 10, 99 (2000)]. *Chaos (Woodbury, N.Y.)*, 11, 427-430. <https://doi.org/10.1063/1.1374241>
- Lewandowski, R., & Pinier, B. (2016). The Kolmogorov law of turbulence what can rigorously be proved? Part II. In (pp. 71-89). [https://doi.org/10.1007/978-3-319-29701-9\\_5](https://doi.org/10.1007/978-3-319-29701-9_5)
- Lienhard, J. H. (1966). *Synopsis of Lift, Drag, and Vortex Frequency Data for Rigid Circular Cylinders*. Technical Extension Service, Washington State University. <https://books.google.com.tw/books?id=qSIQGgAACAAJ>
- Lin, C., Hsieh, S.-C., Lin, W.-J., & Raikar, R. (2012). Characteristics of recirculation zone structure behind an impulsively started circular cylinder. *Journal of Engineering Mechanics*, 138, 184-198. [https://doi.org/10.1061/\(ASCE\)EM.1943-7889.0000314](https://doi.org/10.1061/(ASCE)EM.1943-7889.0000314)
- Lin, T.-H. (2021). *Parametric study on POD analysis of near-wake flow behind circular cylinder* National Cheng Kung University]. Taiwan.
- Lin, W.-J., Lin, C., Hsieh, S.-C., & Dey, S. (2009). Flow characteristics around a circular cylinder placed horizontally above a plane boundary. *Journal of Engineering Mechanics-asce - J ENG MECH-ASCE*, 135. [https://doi.org/10.1061/\(ASCE\)0733-9399\(2009\)135:7\(697\)](https://doi.org/10.1061/(ASCE)0733-9399(2009)135:7(697))
- Mannini, C., Marra, A. M., & Bartoli, G. (2014). VIV–galloping instability of rectangular cylinders: Review and new experiments. *Journal of Wind Engineering and Industrial Aerodynamics*, 132, 109-124. <https://doi.org/10.1016/j.jweia.2014.06.021>
- MATLAB. (2021). *Version 9.10 (R2021a)*. The MathWorks Inc.
- Miniature Wire. (2021). Dantec Dynamics. Retrieved June 15 from <https://www.dantecdynamics.com/components/hot-wire-and-hot-film-probes/dual-sensor-probe/miniature-wire/>
- Mulcahy, T. M. (1984). *Fluid forces on a rigid cylinder in turbulent crossflow* Conference: ASME winter annual meeting, New Orleans, LA, USA, 9 Dec 1984; Other Information: Portions are illegible in microfiche products, United States. <https://www.osti.gov/biblio/5304767>
- Parkinson, G. (1989). Phenomena and modelling of flow-induced vibrations of bluff bodies. *Progress in Aerospace Sciences*, 26(2), 169-224. [https://doi.org/https://doi.org/10.1016/0376-0421\(89\)90008-0](https://doi.org/https://doi.org/10.1016/0376-0421(89)90008-0)
- Pouransari, Z., Vervisch, L., & Johansson, A., V. (2014). Reynolds number effects on statistics and structure of an isothermal reacting turbulent wall-jet. *Flow, Turbulence and Combustion*, 92(4), 931-945. <https://doi.org/10.1007/s10494-014-9539-3>
- Raffel, M., Willert, C. E., Scarano, F., Kähler, C. J., Wereley, S. T., & Kompenhans, J. (2018). PIV uncertainty and measurement accuracy. In *Particle Image Velocimetry: A Practical Guide* (pp. 203-241). Springer International Publishing. [https://doi.org/10.1007/978-3-319-68852-7\\_6](https://doi.org/10.1007/978-3-319-68852-7_6)
- Resvanis, T., Jhingran, V. G., Vandiver, J. K., & Liapis, S. (2012). Reynolds Number Effects on the Vortex-Induced Vibration of Flexible Marine Risers.

- Roach, P. E. (1987). *The generation of nearly isotropic turbulence by means of grids*. Rolls-Royce Limited. <https://books.google.com.tw/books?id=omkHMwEACAAJ>
- Roshko, A. (1955). On the wake and drag of bluff bodies. *Journal of the Aeronautical Sciences*, 22, 124-132.
- Schaefer, J. W., & Eskinazi, S. (1959). An analysis of the vortex street generated in a viscous fluid. *Journal of Fluid Mechanics*, 6(2), 241-260. <https://doi.org/10.1017/S0022112059000593>
- Sciacchitano, A. (2019). Uncertainty quantification in particle image velocimetry. *Measurement Science and Technology*, 30(9). <https://doi.org/10.1088/1361-6501/ab1db8>
- Seyed-Aghazadeh, B., Carlson, D. W., & Modarres-Sadeghi, Y. (2017). Vortex-induced vibration and galloping of prisms with triangular cross-sections. *Journal of Fluid Mechanics*, 817, 590-618. <https://doi.org/10.1017/jfm.2017.119>
- Shih, C.-L., Chen, W.-C., Chang, K.-C., & Wang, M.-R. (2016). Velocity measurements of turbulent wake flow over a circular cylinder. *International Journal of Modern Physics: Conference Series*, 42. <https://doi.org/10.1142/S2010194516601824>
- Tennekes, H., & Lumley, J. L. (1989). *A first course in turbulence*. Butterworth. <https://books.google.com.tw/books?id=pSyuQAACAAJ>
- Townsend, A. A. (1976). *The structure of turbulent shear flow* (2 ed.). <https://ui.adsabs.harvard.edu/abs/1976cup..book.....T>
- Williamson, C. H. K., & Govardhan, R. (2004). Vortex-induced vibrations. *Annual Review of Fluid Mechanics*, 36, 413-455. <https://doi.org/10.1146/annurev.fluid.36.050802.122128>
- Williamson, C. H. K., & Roshko, A. (1988). Vortex formation in the wake of an oscillating cylinder. *Journal of Fluids and Structures*, 2(4), 355-381. [https://doi.org/https://doi.org/10.1016/S0889-9746\(88\)90058-8](https://doi.org/https://doi.org/10.1016/S0889-9746(88)90058-8)
- Zdravkovich, M. M. (1997). *Flow around circular cylinders: Volume 2: Applications*. OUP Oxford. <https://books.google.com.tw/books?id=ApAqBlpSTtIC>